Title

Engineering Platinum-based Nanocatalysts for Proton-exchange-membrane Fuel Cells in Heavy-duty Applications

ISBN

9798184162980

Author

Tsai, Yu-Han

Publication Date

2026-07-27

Peer reviewed|Thesis/dissertation

UNIVERSITY OF CALIFORNIA

Los Angeles

Engineering Platinum-based Nanocatalysts for Proton-exchange-membrane Fuel Cells in Heavy-duty Applications

A dissertation submitted in partial satisfaction of the requirements

for the degree Doctor of Philosophy in Materials Science and Engineering

by

Yu-Han Tsai

2026

ABSTRACT OF THE DISSERTATION

Engineering Platinum-based Nanocatalysts for Proton-exchange-membrane Fuel Cells in Heavy-duty Applications

by

Yu-Han Tsai

Doctor of Philosophy in Materials Science and Engineering

University of California, Los Angeles, 2026

Professor Yu Huang, Chair

Proton-exchange-membrane fuel cells (PEMFCs) directly convert chemical energy into electricity with water as the only byproduct, providing a promising pathway toward a zero-emission future. Their commercial success has been demonstrated in light-duty vehicles (LDVs) exemplified by the Toyota Mirai. Compared with battery electric vehicles (BEVs), fuel cell electric vehicles (FCEVs) offer distinct advantages for heavy-duty vehicles (HDVs), including shorter refueling time, higher payload capacity, and reduced weight penalty. However, the harsh operating conditions and prolonged service life of HDVs impose stringent requirements on PEMFC durability, while the increasing demand for Pt catalyst calls for reduced Pt utilization and scalable manufacturing. Therefore, developing highly durable, cost-effective, and industrially scalable Pt-based electrocatalysts is critical for the widespread commercialization of PEMFCs in heavy-duty transportation.

Chapter 2 presents a graphene-nanopocket protected Pt nanoparticle (Pt@Gnp) that enhances durability by suppressing Pt dissolution, particle coalescence, and ionomer poisoning during accelerated-stress-tests (ASTs). The resulting fuel cell exhibits only 1.1% rated power loss after 90,000 AST cycles, corresponding to a projected lifetime exceeding 200,000 h, more than seven times the U.S. Department of Energy (DOE) ultimate target for heavy-duty applications (30,000 h). Chapter 3 introduces a unique design of Pt nanoparticles embedded with cerium oxide clusters (CeO_x@Pt), in which strong CeO_x-Pt interactions suppress Pt dissolution, migration, and particle growth. The catalyst satisfies the DOE heavy-duty end-of-life (EOL) performance target of 1.07 A/cm^2 at 0.7 V after 90,000 AST cycles at a low total-PGM-loading of approximately 0.1 mg_{PGM}/cm^2, reducing Pt cost by 70% relative to the DOE Million-Mile Fuel Cell Truck (M2FCT) Consortium target. Chapter 4 develops a laser ablation-based synthesis strategy for Pt nanocatalysts that increases production throughput by 10-folds compared with conventional wet-chemical synthesis. The rapid heating and cooling inherent to laser ablation also create metastable nanotwinned structures that enhance catalyst durability during fuel cell operation.

Overall, the work presented in this dissertation demonstrates complementary catalyst design and synthesis strategies that simultaneously improve durability, reduce Pt utilization, and enable scalable catalyst manufacturing. These advances provide practical pathways toward the commercialization of PEMFCs for heavy-duty transportation and contribute to the broader transition toward sustainable, zero-emission transportation.

The dissertation of Yu-Han Tsai is approved.

Carlos Morales-Guio

Daniel Schwalbe-Koda

Ximin He

Yu Huang, Committee Chair

University of California, Los Angeles

2026

DEDICATION

To my parents, Ying-Hui Lin and Sung-Chi Tsai;

my sisters, Pamela Tsai, Cindy Tsai, and Jennifer Tsai;

my grandparents, my uncles, and my aunt,

whose unconditional love and support have made this journey possible.

Table of Contents

List of Figures

List of Tables

Acknowledgements

I would like to express my deepest gratitude to my advisor and committee chair, Prof. Yu Huang, for her unwavering support, guidance, and mentorship throughout my Ph.D. journey. Her scientific insight, intellectual rigor, and critical thinking have profoundly shaped my approach to research, inspiring me to tackle scientific questions with both curiosity and a comprehensive manner. I am also sincerely grateful to my committee members, Prof. Ximin He, Prof. Carlos Morales-Guio, and Prof. Daniel Schwalbe-Koda, whose valuable discussions and feedback have inspired me to continue exploring new research directions.

I am deeply thankful to all of my collaborators for their invaluable contributions to the work presented in this dissertation, including Dr. Jian-Guo Wen and Dr. Ning Su from Argonne National Laboratory, Dr. Qingying Jia from Northeastern University, Dr. Shiqi Zheng from UCLA, and Dr. Mingjie Xu, Dr. Li Xing, Dr. Haiping Sun, Dr. Xiaofeng Liu, Dr. Xingxu Yan, and Han-Hsuan Wu from the University of California, Irvine. Their expertise, collaboration, and support have greatly enriched the studies. I would also like to express my sincere appreciation to my former colleagues in the Huang group, including Dr. Jin Huang, Dr. Bosi Peng, and Dr. Zeyan Liu, who helped me to develop the experimental techniques and analytical skills that have been fundamental to my research. I am equally grateful to my current colleagues Dr. Ao Zhang, Ran Wang, Ting-Jung Hsiao, Yuxiao He, Dr. Yansong Ling, Dr. Heting Pu, Dr. Sibo Wang, and Dr. Yang Liu, for their generosity in sharing ideas, providing assistance, and making our collaborative work both productive and enjoyable.

Finally, I would like to thank my family and close friends for their love, encouragement, and support throughout this challenging yet deeply rewarding journey. Their belief in me has sustained me through both the successes and the setbacks. In particular, I would like to express my

heartfelt gratitude to my dearest friend, Crystal. She has stood by me through every high and low, offering endless love and patience. I will always be grateful for everything she has done for me.

Chapter Two is a version of *Nature Nanotechnology*, Zeyan Liu, Bosi Peng, **Yu-Han Joseph Tsai**, Ao Zhang, Mingjie Xu, Wenjie Zang, Xingxu Yan, Li Xing, Xiaoqing Pan, Xiangfeng Duan, and Yu Huang. 2025, 20, 807-814. DOI: 10.1038/s41565-025-01895-3

Chapter Three is a version of *Journal of the American Chemical Society*. Bosi Peng, Zeyan Liu, **Yu-Han Joseph Tsai**, Ting-Jung Hsiao, Qingying Jia, Jianguo Wen, Tao Zhou, Carlo U. Segre, Xiangfeng Duan, and Yu Huang. 2026, 148, 11, 11871-11878. DOI: 10.1021/jacs.5c21294.

Chapter Four is a version of *Nano Research*. Jin Huang, **Yu-Han Joseph Tsai (equal contribution)**, Shiqi Zheng, Sibo Wang, Heting Pu, Bosi Peng, Zeyan Liu, Ting-Jung Hsiao, Xiangfeng Duan, Bingbing Li, Y. Morris Wang, and Yu Huang. 2025, 18, 12, 94908136. DOI: 10.26599/NR.2025.94908136.

VITA

Education

2019 B.S. in Materials Science and Engineering, National Taiwan University, Taiwan

2021 M.S. in Materials Science and Engineering, Cornell University, U.S.A.

Honor

2022 UCLA J. Yang Scholarship

2023 UCLA Summer Mentored Research Fellowship

2025 IPMI Outstanding Student Recognition

2026 IPMI Ames Goldsmith & Colonial Metals Premier Student Award

Chapter 1. Introduction

1.1 Background and Fuel Cell Fundamentals

In light of the accelerating impacts of climate change in recent years, reducing greenhouse gas (GHG) emissions through the adoption of renewable and sustainable energy technologies has become increasingly critical for achieving global decarbonization goals. Transportation has surpassed other major economic sectors, including agriculture, industry, and residential activities, as the largest source of GHG emissions in the United States since 2016.[1] To address this challenge, the electrification of transportation has attracted significant attention, as reflected by the rapid adoption of electric vehicles (EVs) in recent years. Among the various EV technologies, battery electric vehicles (BEVs) and fuel cell electric vehicles (FCEVs) represent the two most technologically mature approaches.[2] For FCEVs, the latest commercialized Toyota Mirai, released in 2022, features a short refueling time of approximately 5 minutes and a maximum driving range exceeding 402 miles.[3] More importantly, compared with BEVs, FCEVs offer distinct advantages for medium- and heavy-duty transportation applications due to their high efficiency, high power density, fast refueling capability, and significantly lower weight penalty during long-range operation.[4,5] These advantages are particularly important for heavy-duty vehicles (HDVs), where large battery packs can substantially reduce payload capacity and increase charging downtime.

The performance advantages of FCEVs originate from the underlying fuel cell technology used for electrochemical energy conversion. Among the various fuel cell technologies, proton-exchange-membrane fuel cells (PEMFCs) have become one of the leading platforms for transportation applications because of their low operating temperature, rapid startup capability, and scalability.[6] A PEMFC directly converts chemical energy into electricity with water as the only

byproduct. The basic structure of a PEMFC consists of an anode, a cathode, and a proton-exchange-membrane (PEM) for ion transport, as illustrated in Figure 1.1. During device operation, hydrogen is supplied to the anode, where it undergoes the hydrogen oxidation reaction (HOR) to generate protons and electrons. The generated protons migrate through the PEM to the cathode, while the electrons travel through the external circuit to produce electrical power. At the cathode, oxygen undergoes the oxygen reduction reaction (ORR) and combines with protons and electrons to form water. Despite the simplicity of the overall electrochemical reactions, the sluggish ORR kinetics at the cathode remain one of the primary limitations governing PEMFC performance, efficiency, and durability, thereby motivating extensive research into advanced electrocatalyst design strategies.[7]

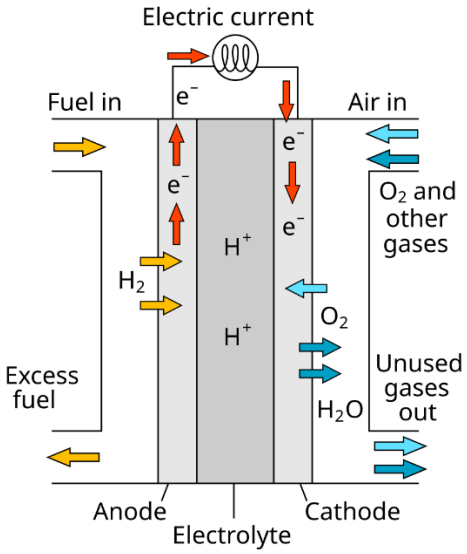

Figure 1. 1 Schematic illustration of the fundamental structure and operating principle of a proton-exchange-membrane fuel cell (PEMFC). Adapted from https://en.wikipedia.org/wiki/Proton-exchange_membrane_fuel_cell.

To overcome the sluggish ORR kinetics at the cathode, platinum-group-metals (PGMs), particularly platinum (Pt)-based catalysts, are widely employed as electrocatalysts in PEMFC. Despite their exceptional catalytic activity and stability in acidic environments, the high cost and

limited abundance of PGMs remain major barriers to the large-scale commercialization of fuel cell technologies. In particular, the cathode catalyst layer (CCL) typically requires a substantially higher Pt loading than the anode due to the intrinsically slow ORR kinetics, making the cathode the dominant contributor to catalyst cost within the fuel cell stack. It has been projected that Pt-related materials account for more than 40% of the total fuel cell stack cost, highlighting the urgent need to reduce PGM usage while maintaining high device performance and durability.[8] Consequently, extensive research efforts have been devoted to the development of highly active and durable electrocatalysts that can maximize Pt utilization, improve catalytic efficiency, and prolong operational lifetime under practical fuel cell operating conditions.

1.2 State-of-the-art Catalyst Design Strategies for PEMFCs

The need to simultaneously minimize the Pt loading while maintaining high fuel cell performance has established several key evaluation metrics for PEMFC electrocatalysts. In practical fuel cell operation, catalyst performance is not solely determined by the initial catalytic activity, but also by the accessibility of active sites, mass transport behavior, and long-term operational durability under harsh electrochemical conditions. Therefore, parameters including mass activity (MA), electrochemically active surface area (ECSA), power density, and durability retention have become critical benchmarks for evaluating and guiding the design of advanced electrocatalysts.

MA is one of the most important metrics for evaluating PEMFC electrocatalysts and is defined as the product of ECSA and specific activity (SA).[9] ECSA is closely related to the surface morphology, particle size, and surface-to-volume ratio of the catalyst nanoparticles, and reflects the amount of accessible catalytic surface area available for electrochemical reactions.[10] In general, catalysts with smaller and well-dispersed nanoparticles exhibit higher ECSA, enabling more

efficient Pt utilization. Moreover, a high ECSA is desirable for reducing local oxygen transport resistance, as the transport resistance is inversely proportional to the accessible Pt surface area.[11] In contrast, SA represents the intrinsic catalytic activity per unit active surface area and is strongly governed by the electronic structure and surface atomic configuration of the catalyst. High SA can be achieved by tuning the electronic structure of Pt through strategies such as alloying, strain engineering, and surface modification, thereby optimizing the adsorption strength of ORR intermediates on the catalyst surface.[12–14] According to the Sabatier principle, the optimal catalytic behavior occurs when the adsorption strength of reaction intermediates is neither too weak nor too strong, which is commonly represented by the peak of the volcano plot relationship for ORR activity.[15]

In addition to catalytic activity, durability is another critical metric governing the practical implementation of PEMFC electrocatalysts, especially for transportation applications that require prolonged operation under dynamic operating conditions. During fuel cell operation, the catalyst layer experiences repeated potential cycling, high humidity, and acidic electrochemical environments, all of which can induce Pt dissolution, particle migration and coalescence, Ostwald ripening, carbon support corrosion, and transition metal leaching in Pt-alloy catalysts.[16] These degradation pathways can reduce the ECSA through particle growth and loss of active surface area, while also altering the electronic structure and surface composition of the catalyst, ultimately leading to decreased catalytic activity and fuel cell performance.[17] Moreover, catalyst degradation can further increase local oxygen transport resistance and ionomer poisoning effects, resulting in more severe performance losses in the high-current-density (HCD) region.[18] To mitigate these degradation pathways, extensive efforts have been made to develop advanced catalyst design strategies, including intermetallic ordering, alloy engineering, surface protection layers, pore

confinement structures, and strong metal-support interactions.[19–21] These approaches aim to stabilize catalyst morphology and composition while preserving the accessibility and intrinsic activity of Pt active sites under long-term operating conditions. Therefore, the development of highly durable electrocatalysts that can simultaneously maintain catalytic activity, structural integrity, and mass transport properties throughout prolonged operation remains one of the central challenges in PEMFC research.

1.3 Challenges of PEMFCs in HDV Applications

Despite the significant progress in catalyst design and fuel cell technology, substantial challenges remain for PEMFCs in heavy-duty applications. Compared with light-duty fuel cell vehicles such as Toyota Mirai, HDVs impose more stringent requirements on fuel cell durability, efficiency, and power output due to their prolonged operating hours, high fuel consumption, and demanding driving conditions.[4] In particular, HDV fuel cells are required to maintain stable operation over extended periods under repeated load cycling and HCD operation, where catalyst degradation and mass transport limitations become increasingly severe. Meanwhile, the large amount of Pt required to satisfy these performance targets significantly increases system cost, creating a critical challenge in balancing catalyst activity, durability, and PGM utilization.[22] Furthermore, although advanced nanocatalyst structures have demonstrated remarkable performance improvements at laboratory scale, many synthetic approaches remain difficult to scale up and lack the throughput necessary for systematic catalyst optimization and industrial production.

To address these challenges, this dissertation focuses on the engineering of advanced Pt-based nanocatalysts for PEMFC applications through three complementary design strategies. The first strategy employs graphene nanopocket-protected Pt catalysts (Pt@Gnp) to achieve

exceptional durability and ultralong projected fuel cell lifetime under heavy-duty-relevant operating conditions by simultaneously suppressing Pt dissolution, particle agglomeration, and ionomer poisoning effects.[23] The second strategy utilized CeO_x-stabilized Pt nanoparticles (CeO_x@Pt) to overcome the conventional trade-off between Pt loading and durability, enabling highly durable fuel cell operation at substantially reduced Pt loading with approximately 70% lower cost.[24] Finally, a laser-ablation-based synthesis strategy is developed for the scalable production of PtCo nanotwinned catalysts, providing a high-throughput and potentially industrially scalable platform for catalyst synthesis and compositional investigation.[25] Collectively, these studies establish fundamental design principles for developing highly active, durable, and scalable PEMFC electrocatalysts toward practical heavy-duty fuel cell applications.

1.4 References

1. U.S. Environmental Protection Agency. *Inventory of U.S. Greenhouse Gas Emissions and Sinks: 1990-2019 – Data Highlights*. (2021).
2. Elgowainy, A. *et al.* Current and Future United States Light-Duty Vehicle Pathways: Cradle-to-Grave Lifecycle Greenhouse Gas Emissions and Economic Assessment. *Environ. Sci. Technol.* **52**, 2392–2399 (2018).
3. Toyota Motor Sales, U.S.A. , Inc. *2022 Toyota Mirai*. https://www.toyota.com/mirai/ (2022).
4. Cullen, D. A. *et al.* New roads and challenges for fuel cells in heavy-duty transportation. *Nat. Energy* **6**, 462–474 (2021).
5. Thomas, C. E. Fuel cell and battery electric vehicles compared. *Int. J. Hydrogen Energy* **34**, 6005–6020 (2009).
6. Haile, S. M. Materials for fuel cells. *Mater. Today* **6**, 24–29 (2003).

7. Liu, Z., Zhao, Z., Peng, B., Duan, X. & Huang, Y. Beyond Extended Surfaces: Understanding the Oxygen Reduction Reaction on Nanocatalysts. *J. Am. Chem. Soc.* **142**, 17812–17827 (2020).

8. Pollet, B. G., Kocha, S. S. & Staffell, I. Current status of automotive fuel cells for sustainable transport. *Curr. Opin. Electrochem.* **16**, 90–95 (2019).

9. Neyerlin, K. C., Gu, W., Jorne, J. & Gasteiger, H. A. Determination of Catalyst Unique Parameters for the Oxygen Reduction Reaction in a PEMFC. *J. Electrochem. Soc.* **153**, A1955 (2006).

10. Rudi, S., Cui, C., Gan, L. & Strasser, P. Comparative Study of the Electrocatalytically Active Surface Areas (ECSAs) of Pt Alloy Nanoparticles Evaluated by Hupd and CO-stripping voltammetry. *Electrocatalysis* **5**, 408–418 (2014).

11. Jomori, S., Nonoyama, N. & Yoshida, T. Analysis and modeling of PEMFC degradation: Effect on oxygen transport. *J. Power Sources* **215**, 18–27 (2012).

12. Mukerjee, S., Srinivasan, S., Soriaga, M. P. & Mcbreen, J. Role of Structural and Electronic Properties of Pt and Pt Alloys on Electrocatalysis of Oxygen Reduction: An In Situ XANES and EXAFS Investigation. *J. Electrochem. Soc.* **142**, 1409–1422 (1995).

13. Zhang, J., Yang, H., Fang, J. & Zou, S. Synthesis and oxygen reduction activity of shape-controlled Pt 3Ni nanopolyhedra. *Nano Lett.* **10**, 638–644 (2010).

14. Wang, D. *et al.* Structurally ordered intermetallic platinum-cobalt core-shell nanoparticles with enhanced activity and stability as oxygen reduction electrocatalysts. *Nat. Mater.* **12**, 81–87 (2013).

15. Nørskov, J. K. *et al.* Origin of the overpotential for oxygen reduction at a fuel-cell cathode. *J. Phys. Chem. B* **108**, 17886–17892 (2004).

16. Meier, J. C. *et al.* Design criteria for stable Pt/C fuel cell catalysts. *Beilstein J. Nanotechnol.* **5**, 44–67 (2014).

17. Zhang, Y. *et al.* Study of the degradation mechanisms of carbon-supported platinum fuel cells catalyst via different accelerated stress test. *J. Power Sources* **273**, 62–69 (2015).

18. Kodama, K., Nagai, T., Kuwaki, A., Jinnouchi, R. & Morimoto, Y. Challenges in applying highly active Pt-based nanostructured catalysts for oxygen reduction reactions to fuel cell vehicles. *Nat. Nanotechnol.* **16**, 140–147 (2021).

19. Yarlagadda, V. *et al.* Boosting Fuel Cell Performance with Accessible Carbon Mesopores. *ACS Energy Lett.* **3**, 618–621 (2018).

20. Zhao, X. *et al.* High-Performance Nitrogen-Doped Intermetallic PtNi Catalyst for the Oxygen Reduction Reaction. *ACS Catal.* **10**, 10637–10645 (2020).

21. Zhao, Z. *et al.* Graphene-nanopocket-encaged PtCo nanocatalysts for highly durable fuel cell operation under demanding ultralow-Pt-loading conditions. *Nat. Nanotechnol.* **17**, 968–975 (2022).

22. Sgarbi, R. *et al.* Does the platinum-loading in proton-exchange membrane fuel cell cathodes influence the durability of the membrane-electrode assembly? *Ind. Chem. Mater.* **1**, 501–515 (2023).

23. Liu, Z. *et al.* Pt catalyst protected by graphene nanopockets enables lifetimes of over 200,000 h for heavy-duty fuel cell applications. *Nat. Nanotechnol.* **20**, 807–814 (2025).

24. Peng, B. *et al.* Sparsely Dispersed CeOx-Stabilized Pt Nanoparticles Overcome Pt Loading–Durability Trade-Off for Highly Durable Heavy-Duty Fuel Cells. *J. Am. Chem. Soc.* **148**, 11871–11878 (2026).

25. Huang, J. *et al.* Synthesis of PtCo nanotwinned catalysts via laser ablation. *Nano Res.* **18**, 94908136 (2025).

Chapter 2. Pt Catalyst Protected by Graphene Nanopockets Enables Lifetimes of Over 200,000 h for Heavy-duty Fuel Cell Applications

2.1 Introduction

The interest in proton-exchange-membrane fuel cells (PEMFCs) has thrived recently as the demand for clean and renewable energy sources expanded.[1] The PEMFCs for light-duty vehicles (LDVs) have entered the early stage commercialization deployment but face considerable infrastructure challenges in competition with battery electric vehicles (BEVs).[2] On the other hand, PEMFCs feature much better scalability with much less weight penalty than lithium-ion batteries for medium- and heavy-duty vehicles (MDV, HDV) that account for less than 5% of the vehicles on the road but produce 26% of the green-house emissions.[3-7] Such MDVs and HDVs also feature lower requirements on infrastructure investment due to the dedicated routes, and thus have been perceived as a major market penetration point for broader commercial adoption of PEMFCs.

However, the distinctive operation conditions in HDV applications have set new challenges for PEMFC technology. For example, typically HDV travels six times farther and consumes over eight times more petroleum than LDV.[5,7] Ensuring the competitiveness of PEMFCs for HDV applications need to satisfy much more stringent fuel cell durability and fuel efficiency requirements. To this end, the US Department of Energy (DOE) has set a series of fuel cell targets dedicated for HDV. Compared with those for LDV, the ultimate lifetime target for HDV has been dramatically increased from 8,000 hours to 30,000 hours, while the efficiency target increased from 70% to 72% (Figure 2. 1a, dash and solid green lines).[3,8] The current status of the fuel-cell-driven buses remains far away from these targets (Figure 2. 1a, blue line).[9-11] To meet these targets requires breakthrough advancements in fuel cell performance and durability. At cell level, the long

lifetime target requires a high power performance retention above 90% in the high-current-density (HCD) region, where the power output is determined, to ensure adequate power for startup and acceleration.[12] Meanwhile, the high efficiency target can be translated to high catalytic activity in the kinetic-controlled low-current-density (LCD) region, as the cell predominantly (ca. 90% of the time) operates in a low-power mode during idling and cruising.[13,14] Therefore, ideal fuel cell catalysts for HDV applications should simultaneously retain their performance metrics in both the LCD and HCD regions throughout the unusually long service life.

To date, immense progress has been made in improving the activity and durability of Pt catalysts in membrane-electrode-assembly (MEA) for cost-effective LDV applications.[15-26] Coating catalyst surfaces with a uniform layer composed of silica or carbon have been found effective to mitigate catalyst degradation.[12,21,27-30] However, it has been recognized that the carbon encapsulation strategies may lead to decreased initial activity due to thick and non-uniform coating, highlighting the challenges in developing a protective layer without sacrificing activity.[29] In our previous study, ultrafine PtCo catalyst protected by porous graphene nanopockets demonstrated high performance and stability for LDV applications at <0.09 mg_{Pt}/cm^2 cathode loading.[28] Nonetheless, the non-precious metal leaching and corresponding cation poisoning effect still pose great challenges in maintaining the long-term durability for HDV applications. With ~0.25 mg_{Pt}/cm^2 cathode loading of PtCo@Gnp, noticeable power performance loss of ~5% at 0.67 V was observed after 30,000 cycles of AST (Figure 2. 2). Particularly, the retention of power performance in HCD region remains unsatisfactory, and no reported state-of-the-art catalysts have reached the stability target of < 10% performance loss, while simultaneously satisfy all performance metrics, after the harsh accelerated stress test (AST) suggested by the DOE, (Figure 2. 2b, Table 2. 1).[8] Moreover, most of the catalyst studies to date adopt the short AST cycles for

LDV, which consists of 30,000 square wave cycles,[22-25,28,31,32] MEA research and performance demonstration with longer AST cycles reflecting behavior in HDV applications is scarce. To ensure the targeted lifetime of HDV over 30,000 hours, the Million Mile Fuel Cell Truck Consortium (M2FCT) has extended the AST cycles from 30,000 to 90,000,[33-36] which poses a formidable challenge in catalyst durability and demands new materials design with exceptional durability throughout the operating regions. These challenges and observation laid the foundation for further development of HDV-relevant pure Pt catalyst with superior durability.

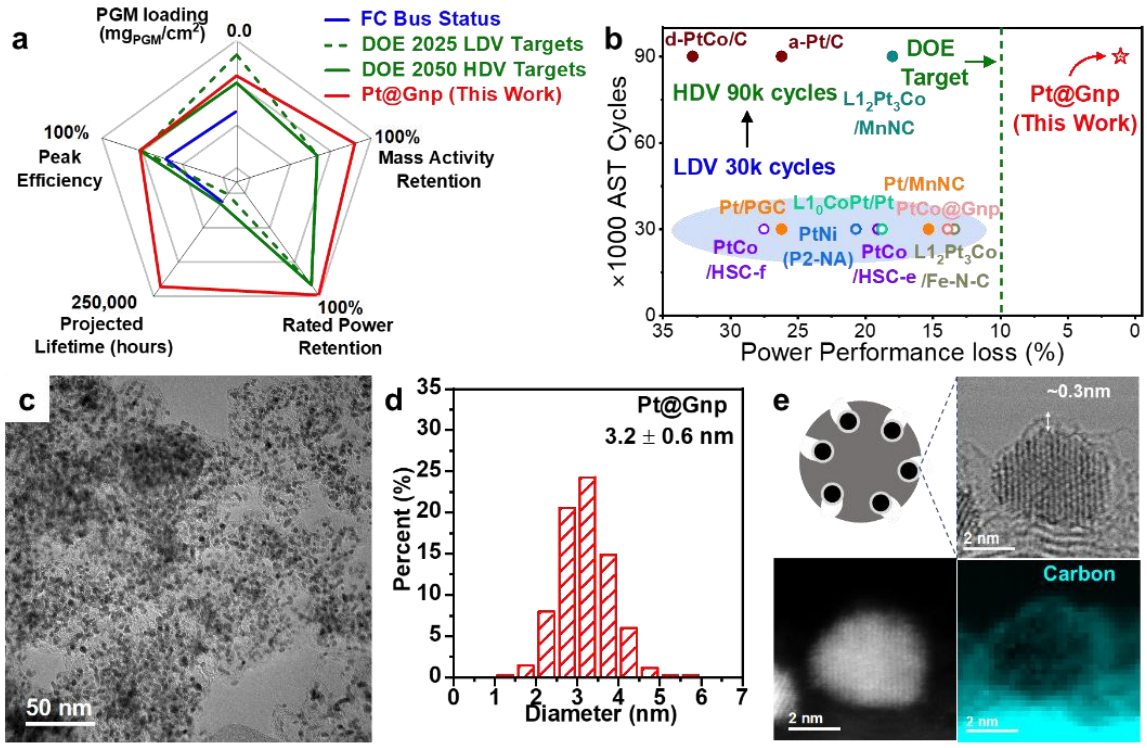

Figure 2. 1 Overall performance demonstration and structural characterizations of the developed catalyst. (a) Comparison of major fuel cell performance metrics among current fuel cell bus status (black), DOE 2050 HDV targets (solid green), DOE 2025 LDV targets (dashed green), and the developed Pt@Gnp/KB catalyst (red). (b) Comparison of AST cycles and rated power degradation between the developed Pt@Gnp/KB catalyst and the state-of-the-art catalysts (PtCo@Gnp;[28] PtCo/HSC-e, PtCo/HSC-f;[32] Pt/PGC, Pt/MnNC;[31] PtNi P2-NA;[22] $L1_0$ CoPt/Pt;[25] $L1_2$ Pt_3Co/Fe-N-C;[23] d-PtCo/C, a-Pt/C;[34] $L1_2$ Pt_3Co/MnNC;[35] hollow and solid symbols represent LDV-relevant and HDV-relevant PGM Platinum group metal (PGM) loading, respectively), showing that the Pt@Gnp/KB catalyst represents the only candidate satisfying power performance durability target at a high AST cycle number. (c) TEM image of the developed Pt@Gnp/KB catalyst. (d) Count-based particle size distribution of the Pt@Gnp/KB catalyst with averaged particle diameter. (e) HR-STEM and EELS mapping images show that the Pt@Gnp/KB catalyst is covered by a thin carbon layer with a thickness of around 0.3 nm.

Catalyst	Cathode Loading (mg_{Pt}/cm^2)	Total Loading (mg_{Pt}/cm^2)	Mass Activity (MA) (A/mg_{Pt})			30k MA Retention (%)	90k MA Retention (%)	ADT Condition	Power@0.67V (W/cm^2)			30k Rated Power Loss (%)	90k Rated Power Loss (%)
			BOL	30k	90k				BOL	30k	90k		
DOE Targets	NA	≤ 0.125 LDV ≤ 0.300 HDV	> 0.44	> 0.264	NA	> 60	NA	Square Wave	>1.0	>0.9 (for LDV)	>0.9 (for HDV)	<10 (for LDV)	<10 (for HDV)
Pt@Gnp/KB (This Work)	**0.225**	**0.25**	**0.74±0.0014**	**0.87±0.0014**	**0.65±0.007**	**-17.6**	**87.8**	**Square Wave**	**1.077±0.026**	**1.107±0.014**	**1.065±0.043**	**-2.8**	**1.1**
comm-Pt/VC (This Work)	0.25	0.275	0.35±0.019	0.16±0.019	0.08±0.005	45.7	22.9	Square Wave	1.120±0.038	0.906±0.020	0.677±0.011	17.9	39.6
comm-Pt/KB (This Work)	0.25	0.275	0.79±0.019	0.45±0.05	0.29±0.019	57.0	36.7	Square Wave	1.159±0.030	1.050±0.054	0.956±0.046	9.4	17.5
a-Pt/C[34]	0.25	0.3	0.416*	0.276*	0.177*	66.3	42.5	Square Wave	0.962*	NA	0.710*	NA	26.2
d-PtCo/C[34]	0.25	0.3	0.823*	0.335*	0.145*	40.7	17.6	Square Wave	0.902*	NA	0.606*	NA	32.8
Pt_3Co/HSC[33]	0.25	0.3	NA	NA	NA	NA	NA	Square Wave	0.914*	NA	0.742*	NA	18.8
$L1_0$-CoPt[33]	0.25	0.3	NA	NA	NA	NA	NA	Square Wave	0.880*	NA	0.741*	NA	15.8
$L1_2$ Pt_3Co/MnNC[35]	0.2	NA	0.49	NA	0.31	NA	63	Square Wave	1.221[a]	NA	1.001[a]	NA	18
$L1_0$-PtNiGa[36]	0.2	NA	0.6	NA	0.4	NA	66	Square Wave	1.36[a]	1.26*	1.10*	7.4	19.1
PtCo@Gnp[28]	0.09	0.1	1.136	0.754	NA	66.4	NA	Square Wave	1.013	0.872	NA	13.9	NA
Pt/Mn-N-C[31]	0.20	0.30	NA	NA	NA	NA	NA	Square Wave	1.246*[a]	1.055*[a]	NA	15.3	NA
Pt/PGC[31]	0.20	0.30	NA	NA	NA	NA	NA	Square Wave	0.985*[a]	0.727*[a]	NA	26.2	NA
PtCo/HSC-e[32]	0.100	0.125	0.65	0.37	NA	56.9	NA	Square Wave	1.10*	0.889*	NA	19.0	NA
PtCo/HSC-f[32]	0.100	0.125	0.71	0.33	NA	46.5	NA	Square Wave	1.22*	0.886*	NA	27.5	NA
PtNi (P2-NA)[22]	0.100	0.15	0.63	0.44	NA	70.0	NA	Triangle Wave	0.75*	0.59*	NA	20.7	NA
$L1_0$-CoPt/Pt[25]	0.105	0.205	0.56	0.45	NA	81.0	NA	Square Wave	0.52*	0.42*	NA	18.8	NA
$L1_2$ Pt_3Co/FeNC[23]	0.10	0.20	0.72	0.44	NA	62	NA	Square Wave	0.83*	0.72*	NA	13.4	NA

Table 2. 1 Comparison of key fuel cell performance metrics with the state-of-the-art catalysts. Notably, the MEA with Pt@Gnp/KB catalyst satisfied all DOE performance metrics and out performed all the state-of-the-art catalysts in durability, highlighting the promising application in heavy-duty applications. a: Tested under unrealistic high air flow rate of 2000 sccm. *: Values were extracted from the plots. The error bar represented the standard deviation derived from at least two independent tests.

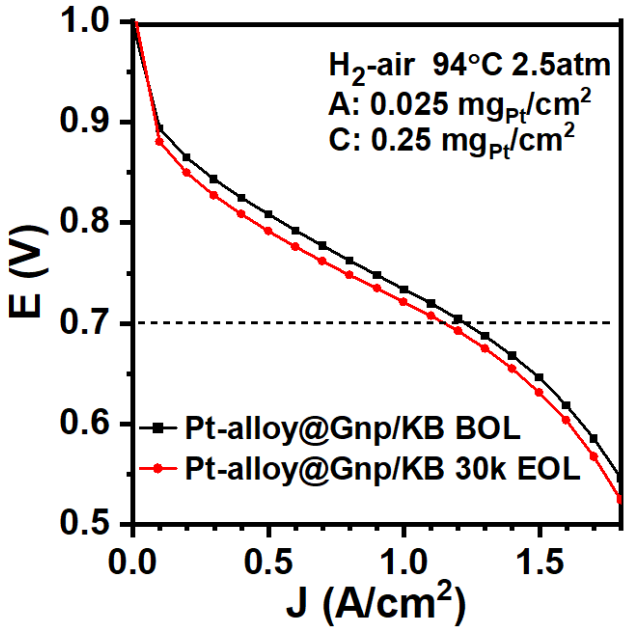

Figure 2. 2 H_2-air performance of Pt-alloy@Gnp/KB at high catalyst loading before and after 30,000 AST cycles, showing noticeable performance loss.

Here we present an ultrafine pure Pt catalyst protected by graphene nanopockets and supported on the KetjenBlack carbon (Pt@Gnp/KB) as highly durable ORR electrocatalyst in PEMFC. The fabricated MEA with our Pt@Gnp/KB nanocatalyst delivers a high initial MA of 0.74 A/mg_{Pt} and an outstanding rated power density of 1.08 W/cm^2 with 0.25 mg/cm^2 total Pt loading, and an unprecedented durability with an exceptionally small rated-power loss of 1.1% after 90,000 aggressive square wave cycles. The remarkable activity and durability throughout the operating region project an ultra-long fuel cell lifetime of over 218,000 hours with high efficiency of around 72% (Fig. 2. 1a, red line), far beyond the current fuel cell bus status[9-11] and exceeding the DOE 2050 ultimate targets for HDV.[8] The origin of the enhanced durability was comprehensively investigated and confirmed through the probing of size agglomeration, Pt dissolution, and ionomer poisoning effect. With proven mitigation of these degradation pathways, we showcase a highly attractive catalyst design for HDV applications with a stringent requirement on durability and efficiency challenges.

2.2 Methods

Materials and Chemicals

Platinum(II) acetylacetonate [$Pt(acac)_2$], cobalt(II) acetylacetonate [$Co(acac)_2$], aquivion D83-06A ionomer dispersion were purchased from Sigma Aldrich. Commercial Pt/VC catalysts (comm-Pt/VC) with weight ratio of Pt: 10% and 40% were purchased from Alfa Aesar. Commercial Pt/KB (comm-Pt/KB) catalyst was purchased from The Fuel Cell Store. Isopropanol (IPA), and acetone were purchased from Fisher Scientific. Freudenberg H14C7 gas diffusion layer (GDL), and polytetrafluoroethylene (PTFE) gasket were purchased from The Fuel Cell Store. Carbon black (Ketjenblack EC-300J) was obtained from Fitz Chem LLC. The water used was Ultrapure Millipore (18.2 MΩ·cm).

Catalyst Preparation

Synthesis of Pt@Gnp/KB with infrared radiation furnace: The synthetic protocol is modified from a previous reported work.[28] In a typical synthesis, carbon black (Ketjenblack EC-300J), platinum (II) acetylacetonate [$Pt(acac)_2$], and acetone were mixed in glass vial under ultrasonication for 10 min, and then acetone in the mixture was evaporated. The resultant metal precursor adsorbed carbon black was finely ground into fine powder, and then annealed at 200 °C under Ar atmosphere. The as-synthesized catalyst was further cleaned by acid washing in N_2-saturated 0.05 M H_2SO_4 solution at 80 °C for 12 h. After acid washing, the catalyst was washed with ultrapure water and collected via centrifugation for 4-6 times. After thoroughly drying in vacuum, the obtained catalyst is then annealed in H_2/Ar mixture in a conventional furnace at 180 °C for 1.5 h. After fully cooled down to room temperature, the sample was collected to give the Pt@Gnp/KB catalyst, which was ready for the test.

Synthesis of Pt-alloy@Gnp/KB: The synthetic protocol followed the same process of our previous reported work,[28] and with the same processing of as-synthesized catalyst as Pt@Gnp/KB.

Structure and Composition Characterization

X-ray powder diffraction (XRD) patterns were collected with a Panalytical X'Pert Pro X-ray powder diffractometer with Cu-Kα radiation. The Pt loading in the studied catalysts and the Pt loading in the fabricated MEAs were determined by inductively coupled plasma optical emission spectroscopy (ICP-OES, Shimadzu ICPE-9000). The samples were heated and fully digested with concentrated nitric acid and hydrochloric acid to avoid the impact from the carbon support before the ICP-OES measurement. X-ray photoelectron spectroscopy (XPS) tests were done with Kratos AXIS Ultra DLD spectrometer. XPS depth profiling was conducted using the instrument's Ar^+ ion source operated at 4 kV, 50 uA, and rastered over a 3×3 mm area for 4 minutes.

Scanning transmission and transmission electron microscopy (STEM/TEM) images and energy dispersive X-ray spectroscopy (EDS) were taken with an JEOL JEM 2800 transmission electron microscope with a voltage of 200 kV. The TEM/STEM sample grids were prepared by dispersing the sample in a mixture of water and ethanol, then drop casting the dispersion onto lacey carbon film coated copper grids (for high-resolution STEM and EDS analysis). The end-of-life MEA samples for TEM/STEM were prepared by exfoliating the cathode catalyst layer from the MEA using sonication in a mixture of water and ethanol, then dropcast the dispersion onto a lacey grid. The size analysis for the catalysts from the TEM/STEM images were obtained from multiple regions and averaged from over 300 particles in each sample. The MEA cross-section samples were prepared by an ultramicrotome at thickness around 100 nm. The ratio of the Pt dissolved in the Pt band is calculated by integrating the Pt L-edge from the Pt band region divided by the total Pt signal from the entire region (membrane plus cathode catalyst layer), the results were averaged

from over 5 different regions in each sample, and the Pt band region was carefully selected by inspecting the location before and after the acquisition. The high-resolution STEM-EELS experiments were conducted with the spherical aberration-corrected Nion UltraSTEM200, operated at 60 kV. The convergence semi-angle and the beam current were set as 38 mrad and ~15 pA, respectively. The EELS dispersion and dwell time were 0.28 eV/channel and 0.5 s/pixel, respectively. The pixel size of the STEM-EELS spectrum image was set as 0.20–0.34 nm, depending on the field of view. The data analysis of removing background was carried out by the power-law function in the commercial software package Digital Micrograph. The low accelerating voltage and low beam current were used to mitigate the electron beam-induced damage to the sample, especially for the thin carbon layer structure. Additional precautions including (1) pre-treatment of the TEM grids at 160 °C in a vacuum chamber for over 8 hours to remove most of the residual solvent and other absorbed molecules, which are the major sources of contamination before transferring them into Nion UltraSTEM200 electron microscope; (2) High-resolution STEM experiments were only conducted when the pressure of the TEM column is lower than 2×10^{-9} Torr to ensure an ultraclean environment. Therefore, we can exclude the carbon deposits and other artifacts that presumably occurred in TEM for explaining the formation of carbon layer covering Pt nanoparticles.

Estimation of Mass-weighted Size Distribution

By assuming a spherical model using the measured size as diameter, we can estimate the relative volume and the relative mass of each nanoparticle to obtain the mass-weighted size distribution, which gives the distribution of Pt mass among Pt nanoparticles of different sizes. The weighted average size ($\bar{d}_w$) is obtained by the following **Eq. 1**. The d_i, m_i, V_i, and ρ are the size, mass, volume, and density of that nanoparticle, correspondingly.

$$\bar{d}_w = \frac{\sum_1^n d_i m_i}{\sum_1^n m_i} = \frac{\rho \sum_1^n d_i V_i}{\rho \sum_1^n V_i} = \frac{\sum_1^n d_i V_i}{\sum_1^n V_i} \qquad \textbf{Eq. 1}$$

MEA Fabrication and Fuel Cell Testing

Catalysts were employed as the cathode catalyst in a 5 cm^2 MEA for fuel cell testing. The catalyst ink was made by mixing the catalysts with the ionomer solution (Aquivion D83-06A) and water-IPA solvent through ultrasonication. The ionomer ratio was 0.6 for catalysts with solid low-surface-area carbon (*e.g.*, Vulcan carbon), and 0.7 for porous high-surface-area carbon (*e.g.*, KetjenBlack carbon). The fresh ink was then spray-coated onto a reinforced perfluorosulfonic acid (PFSA) membrane (12 μm thickness) by using a Sono-Tek ultrasonic spray system. Anode catalyst was the commercial 10% Pt/VC with PGM loading fixed to be 0.025 mg_{Pt}/cm^2. The cathode catalyst loading was controlled to be around 0.25 mg_{Pt}/cm^2. Both anode and cathode loading were confirmed by the ICP-AES measurements. The fabricated catalyst-coated membrane (CCM) was dried in a vacuum desiccator for an hour to evaporate the solvents before assembly. Two gas diffusion layers (GDLs), two PTFE gaskets, and the prepared CCM were pressed to prepare MEA. The thickness of the PTFE gasket is 127 μm (5 mil). The thickness of GDL, which includes a microporous layer, is 175 μm (Freudenberg H14C7).

The prepared MEA was loaded in Fuel Cell Technology 5 cm^2 single-cell hardware and tested with the Scribner 850e Fuel Cell Station with a Scribner 885 Potentiostat. The MEA was conditioned and tested following a protocol similar to DOE Fuel Cell Performance and Durability Consortium (FC-PAD).[42] The MEA was initially activated by holding the potential at 0.5 V under H_2/Air flow at 80 °C, 100% relative humidity (RH), 150 kPa_{abs} (abs: absolute; all pressure noted in this work refer to the absolute pressure), until a stable current output was reached. Then, the MEA was further activated at an oversaturated condition under H_2/Air flow. Multiple cycles of mass activity and power performance tests were then performed in order to deliver the best

evaluation of the performances. The mass activity was tested under H_2/O_2 at 80 °C, 150 kPa_{abs}, 100% RH, with a gas flow rate of 835/2000 sccm for anode/cathode. The rated power of prepared MEA was tested under H_2/Air flow at 94 °C, 250 $kPa_{abs,}$ and 100% RH with a practical low flow rate of 168/531 sccm for anode/cathode, which is equivalent to the stoichiometry ratio of 1.5/2.0 at 3.2 A/cm^2. The rated power was measured under the heat-rejection constrain ($Q/\Delta T_i$ of <1.45) at rated voltage (V_{rated}), which can be defined by the following **Eq. 2**.[1] The DOE protocol assumes P_{stack} = 90 kW and $T_{ambient}$ = 40 °C which gives a rated voltage of 0.67 V at 94 °C.[1] The fuel cell polarization data was obtained through cathodic current scan with a holding time of at least 30s at each point to allow the cell voltage to be stabilized.

$$\frac{Q}{\Delta T_i} = \frac{P_{stack}(1.25 - V_{rated})}{V_{rated}(T_{stack} - T_{ambient})} \qquad \textbf{Eq. 2}$$

The ECSA was determined by integrating the CO stripping peak assuming 420 μC/cm^2_{Pt} at 80 °C and ambient pressure. The CO stripping test under 100% relative humidity and 20% relative humidity in MEA was generally followed the protocol noted in literature.[37] The CO-displacement experiment was conducted followed previous literature[38,39]: The MEA was hold at desired cell potentials ranging from 0.2-0.5 V at ambient pressure. After 5 mins stabilization at each potential, 2.0% CO (diluted by N_2) at a flow rate of 200 sccm was introduced to the cathode of the cell, and the cell current was recorded during the process. The ion coverage (θ) of the Pt surface was calculated by the ratio of the integrated displacement charge and the integrated CO stripping charge. The accelerated durability test (AST) included up to 90,000 square wave cycles with each cycle holding the MEA at the voltage of 0.6 V for 3 seconds and then 0.95 V for 3 seconds, according to the DOE and M2FCT suggested AST protocol for PGM based catalysts.[1,33] The AST is carried at 80 °C, ambient pressure, 100% RH with H_2/N_2 flow 100/100 sccm for anode and cathode, respectively. The startup/shutdown (SU/SD) AST is carried out followed DOE recommended

protocol for unmitigated startup/shutdown[1] by repeatedly shutting down the cell and switching the anode feed gas from H_2 to air at 100 sccm for 60 seconds.

Projection of Fuel Cell Efficiency

Voltage efficiency is adopted to reflect the practical peak efficiency of the fuel cell system, which is the ratio between the peak operating voltage and the lower-heating-value of hydrogen (around 1.25 V at 94 °C) (**Eq. 3**). The operating voltage where gives the peak efficiency is achieved at 7.3% of rated power, which is calculated based on a representative Class 8 HDV with a 275 kW fuel cell system and a 20 kW idle power.[3] Noted that the calculation does not include the parasitic electrical losses due to auxiliary systems and the actual fuel consumption throughout operation, which is extremely difficult to accurately measure.[40]

$$Peak\ Efficiency = \frac{V_{peak,7.3\%\ rated\ power}}{V_{LHV\ Hydrogen}} \qquad \textbf{Eq. 3}$$

Projection of Fuel Cell Lifetime

The DOE has defined the fuel cell lifetime as the time of operation to reach 10% loss in cell voltage at rated power.[1,8] We adopt the current density at 1.5 A/cm^2 where the rated power is typically delivered to be the studied point. The lifetime of the tested MEA is then calculated by dividing the 10% of initial voltage at 1.5 A/cm^2 and the averaged voltage loss rate at 1.5 A/cm^2. An time acceleration factor of 100 over drive-cycle is used according to previous literature (**Eq. 4**).[41] Noted that a full square wave cycle takes 6 sec (0.6 V for 3 seconds and 0.95 V for 3 seconds). It is worth noting that the projection is based on an averaged degradation rate of the catalyst lifetime. Catalyst durability plays a very important role in deciding the fuel cell system lifetime which is also dependent on the durability of other system components such as proton-exchange-membrane.

$$Lifetime\ (hours) = \frac{10\% \times V_{inital}\ (mV)}{V\ Loss\ Rate\ \left(\frac{mV}{cycle}\right)} \times 6\left(\frac{sec}{cycle}\right) \times 100 \div 3600\left(\frac{sec}{hour}\right) \qquad \textbf{Eq. 4}$$

2.3 Results and Discussion

Catalyst Preparation and Strcuture

The Pt@Gnp/KB catalysts were prepared by an impregnation method (see Methods for detail).[27] The TEM images reveal that the Pt nanoparticles are densely and uniformly dispersed in the carbon support (Figure 2. 1c) with an average diameter of 3.2 ± 0.6 nm (Figure 2. 1d). The XRD shows that the Pt@Gnp/KB catalyst has a face-centered cubic (fcc) structure, similar to the commercial comm-Pt/VC and comm-Pt/KB catalysts (Figure 2. 3). The comparison of between surface and bulk Pt content, obtained from surface-sensitive XPS and bulk ICP-OES, revealed that the Pt particles were more confined in the carbon support compared to the commercial catalysts (Figure 2. 4). The confinement structure in Pt@Gnp/KB was further validated by the comparison between transmission microscopic images and the surface-sensitive secondary electron images (Figure 2. 5), which clearly showed that Pt@Gnp/KB had much less particles on the surface. To reveal the graphene-protected structure, we conducted high-resolution STEM imaging and the EELS mapping, which clearly revealed that the Pt nanoparticles are covered by a very thin (ca. 0.3 nm) graphene layer (Figure 2. 1e, Figure 2. 6).

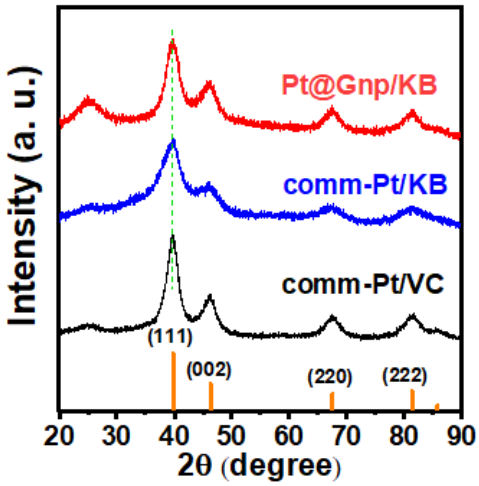

Figure 2. 3 Powder XRD patterns of the (a) Pt@Gnp/KB, (b) comm-Pt/KB, and (c) comm-Pt/VC catalysts.

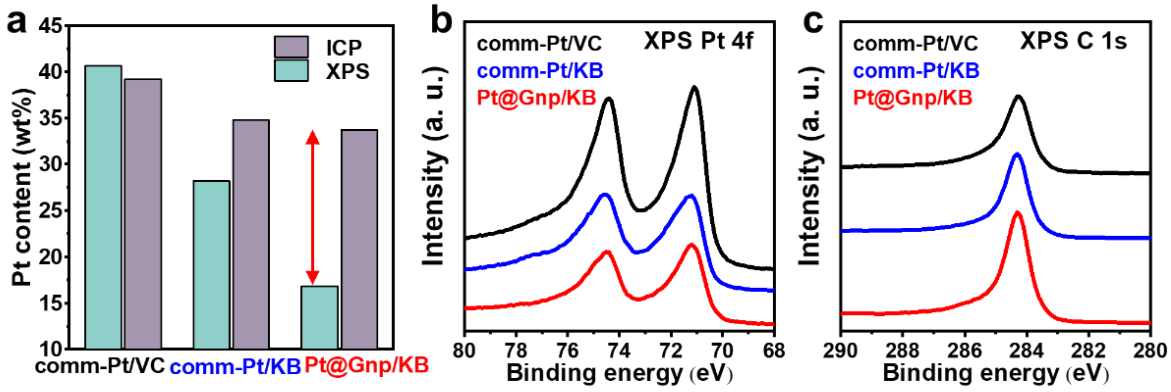

Figure 2. 4 (a) Comparison of Pt loading using bulk characterization (ICP) and surface sensitive characterization (XPS). The large gap between ICP and XPS result in Pt@Gnp/KB sample indicates that the Pt content is more confined. Raw data from XPS collected at (b) Pt 4f and (c) C 1s.

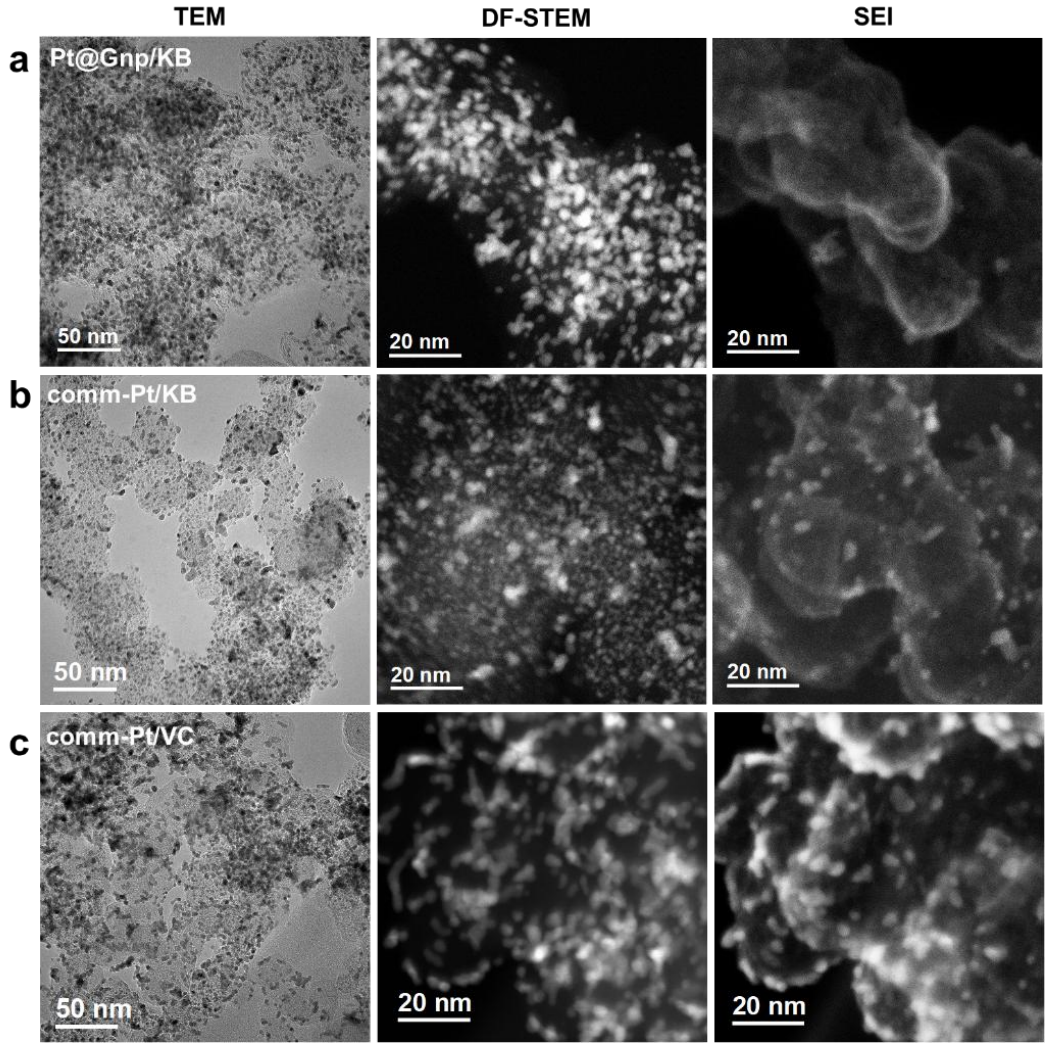

Figure 2. 5 Comparison of images between bulk transmission imaging (TEM, STEM) and surface sensitive secondary electron imaging (SEI) of (a) Pt@Gnp/KB, (b) comm-Pt/KB, and (c) comm-Pt/VC catalysts.

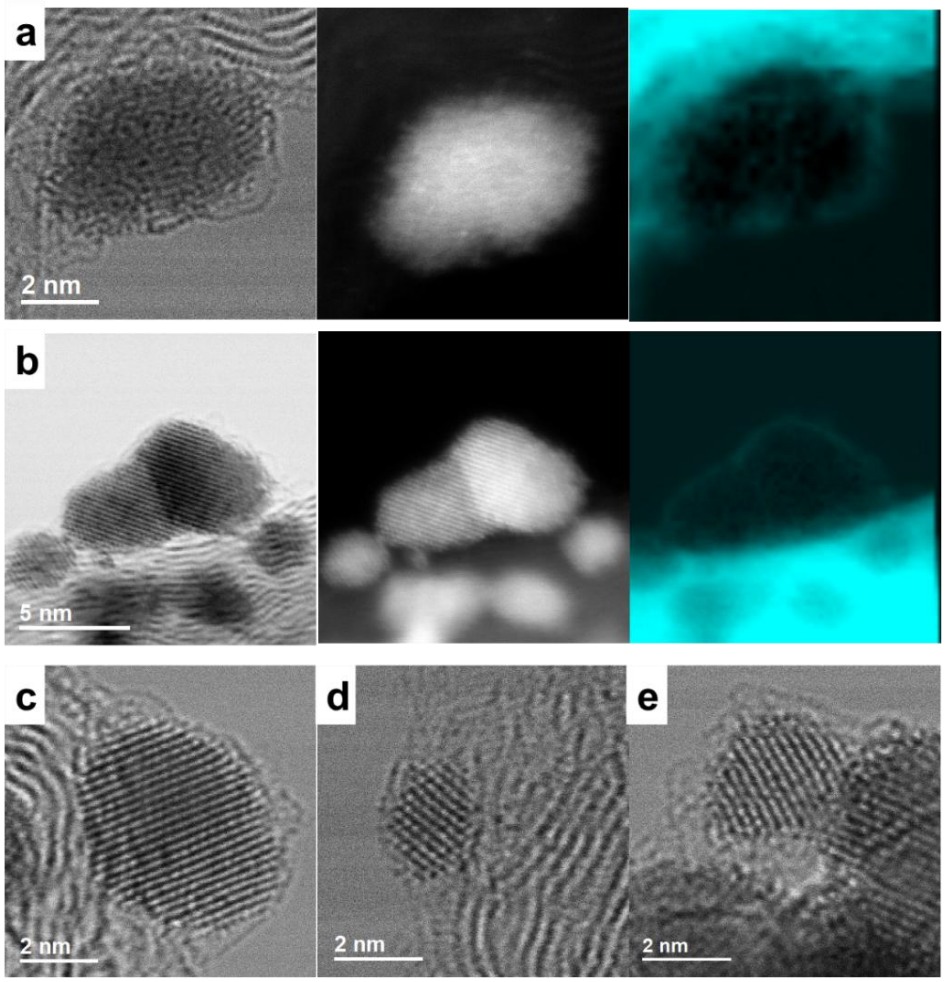

Figure 2. 6 Bright field, dark field STEM and carbon EELS mapping images at different surface locations at BOL showing that the Pt@Gnp/KB catalyst is covered by a thin graphene layer.

Fuel Cell Performance

We have evaluated the performance of the Pt@Gnp/KB catalyst against commercial catalysts (Figure 2. 7) in a 5 cm^2 single-cell fuel cell fixture. For a fair comparison, all cell components were kept the same in all tested MEAs except for the cathode catalyst. Accordingly, the MEAs were labeled by the cathode catalysts. All MEA performance metrics, including ORR MA, rated power, and durability, were tested and evaluated following the DOE recommended protocols,[1] except the AST that was extended to 90,000 cycles as recommended by the M2FCT (see Methods).[33] Note that we have also used the aggressive square-wave protocol that was previously shown to exhibit a hundred times acceleration (with respect to time) over the modified

wet drive-cycle protocol, thus representing a more aggressive test protocol for estimating the lifetime degradation of catalysts.[37]

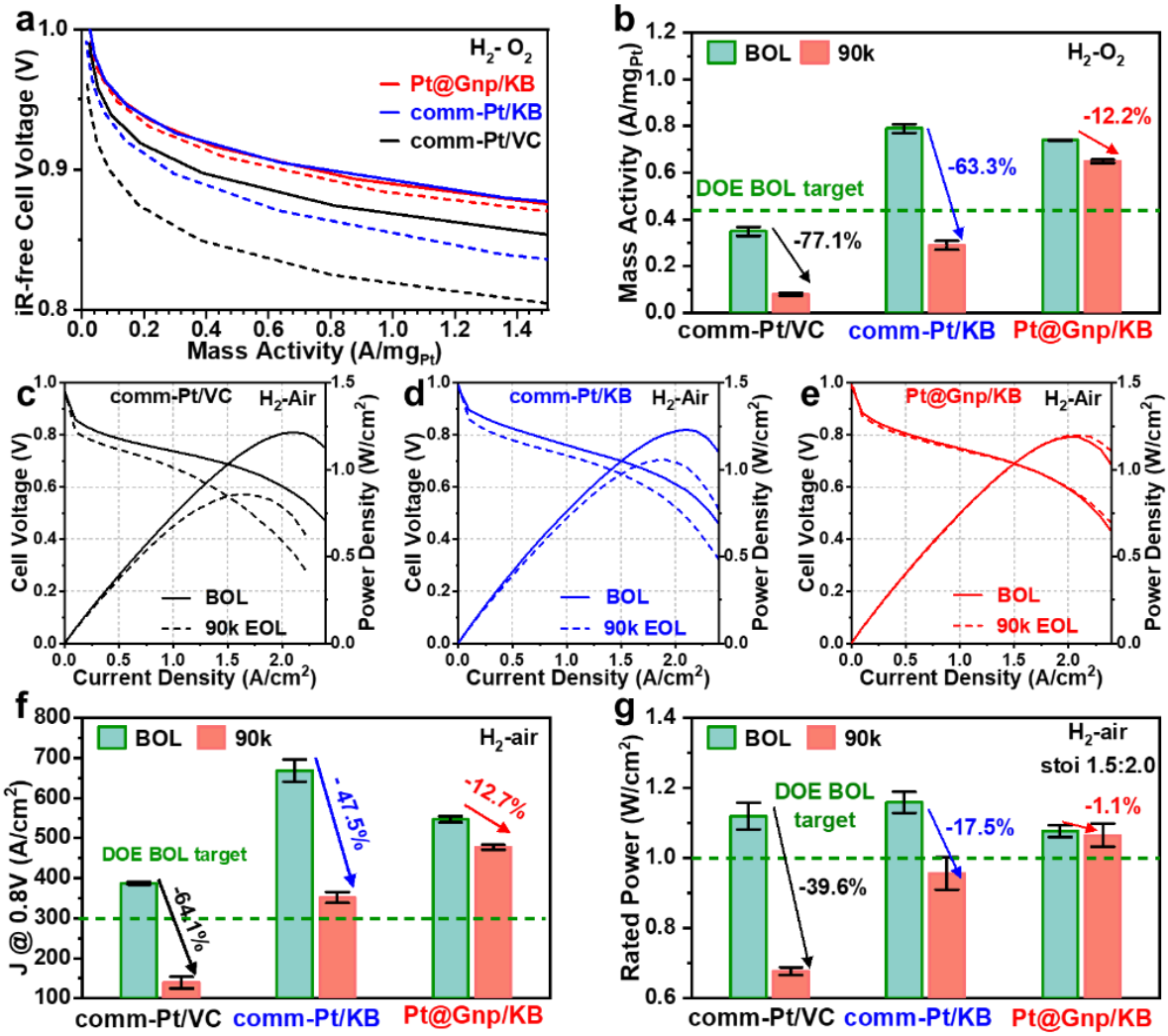

Figure 2. 7 Fuel cell performance evaluation of commercial catalysts (comm-Pt/VC and comm-Pt/KB) and the developed Pt@Gnp/KB catalyst. H_2/O_2 performance comparison of (a) the polarization plots, and (b) the MA evaluated at 0.9 $V_{iR\text{-}free}$, at BOL and EOL after 90k AST cycles. (c-g) H_2/air practical performance comparison. The polarization plots comparison of performance at BOL and EOL after 90k AST cycles (c) comm-Pt/VC, (d) comm-Pt/KB, and (e) developed Pt@Gnp/KB catalyst. (f) Performance comparison at 0.8 V at BOL and EOL after 90k AST cycles. Reflecting catalyst performance at LCD and related to cell efficiency. (g) Performance comparison at rated voltage of 0.67 V at BOL and EOL after 90k AST cycles. Reflecting catalyst performance at HCD and related to device power output. All error bars represented standard deviation with the middle as the averaged value derived from at least two independent tests.

The ORR kinetics and the MA of the catalysts were tested under H_2/O_2 at differential flow conditions to minimize the impact of mass transport losses (Figure 2. 7a, Figure 2. 8).[42] Notably,

the Pt@Gnp/KB catalyst demonstrates an impressive MA of 0.74 ± 0.001 A/mg_{Pt}, comparable with the comm-Pt/KB (0.79 ± 0.019 A/mg_{Pt}) and higher than the comm-Pt/VC catalysts (0.35 ± 0.019 A/mg_{Pt}) and the DOE targets of 0.44 A/mg_{Pt} (Figure 2. 7b). More importantly, the Pt@Gnp/KB catalyst exhibits a high MA retention of 87.8% at the EOL after the aggressive 90,000 square-wave AST cycles (Figure 2. 7b), which is significantly higher than the 36.7% and 22.9% retentions for comm-Pt/KB and comm-Pt/VC catalysts, respectively. It is also noteworthy that a high EOL MA of 0.65 ± 0.007 A/mg_{Pt} is achieved with the Pt@Gnp/KB catalyst, which is 2.2 and 8.1 times of the comm-Pt/KB (0.29 ± 0.019 A/mg_{Pt}) and comm-Pt/VC (0.08 ± 0.005 A/mg_{Pt}), respectively. The high MA and its excellent retention clearly demonstrate the advantage of Pt@Gnp/KB over commercial catalysts in achieving good performance and durability in cell efficiency which is determined in the LCD region.

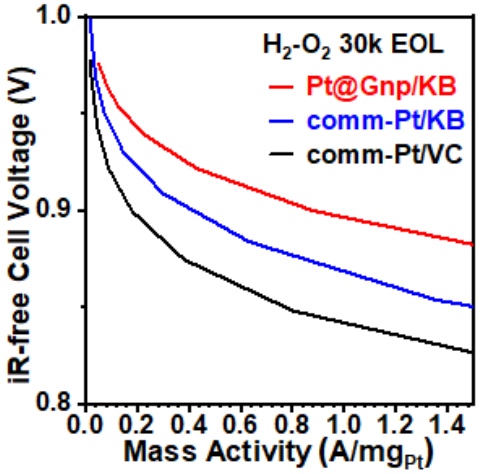

Figure 2. 8 Comparison of H_2/O_2 polarization plots of comm-Pt/KB, comm-Pt/VC, and Pt@Gnp/KB catalysts at EOL after 30k AST cycles.

Beyond the H_2/O_2 test under differential condition, the practical performances of the catalysts were evaluated under realistic operating conditions with the H_2/air flow at a low stoichiometry of 1.5:2.0 (Figure 2. 7c-e, Figure 2. 9).[8] As mentioned, performances in both LCD and HCD regions are equally important as they determine the fuel cell efficiency and the power output, respectively. To benchmark the practical performance in the LCD region, the DOE has set

a target of a current density of 0.3 A/cm^2 at 0.8 V for LDV.[1] The Pt@Gnp/KB delivers a high current density of 0.55 ± 0.008 A/cm^2 which is slightly lower than the comm-Pt/KB catalysts (0.67 ± 0.028 A/cm^2), but noticeably higher than the comm-Pt/VC catalyst (0.39 ± 0.004 A/cm^2) (Figure 2. 7f). More importantly, after 90,000 square-wave AST cycles, the Pt@Gnp/KB catalyst at EOL retains the highest current density of 0.48 ± 0.006 A/cm^2 and the highest retention of 87.3%, notably outperforming the commercial catalysts (0.35 ± 0.014 A/cm^2 and 52.5% retention for comm-Pt/KB; and 0.14 ± 0.015 A/cm^2 and 35.9% retention for comm-Pt/VC) (Figure 2. 7f).

Meanwhile, the rated power performance is evaluated at 0.67 V under the heat-rejection constrain to reflect the practical performance in the HCD region.[1] Notably, the Pt@Gnp/KB catalyst delivers a comparable rated power (1.08 ± 0.026 W/cm^2) to the comm-Pt/KB (1.16 ± 0.030 W/cm^2) and comm-Pt/VC (1.12 ± 0.038 W/cm^2) catalysts (Figure 2. 7g), suggesting that the thin protective layer and the pore confined structure does not impose high oxygen transport resistance to sacrifice the accessibility and power density performance of the Pt@Gnp/KB catalyst. Most significantly, the Pt@Gnp/KB catalyst demonstrates exceptional power retention after 90,000 square-wave AST cycles, with only a 1.1% loss of its initial rated power, far less than the 17.5% and 39.6% rated power losses for the comm-Pt/KB (0.96 ± 0.046 W/cm^2) and comm-Pt/VC (0.68 ± 0.011 W/cm^2) catalysts, respectively (Figure 2. 7g, Figure 2. 9). To probe the impact of relative humidity on the catalyst performance and durability, we evaluated the power performance at BOL and after 90k AST cycles under lower relative humidity of 65%, the results showed that the outstanding durability was still preserved with a small rated power loss of 0.2% (Figure 2. 10a). In addition, the trend of high-frequency resistance indicated that the performance decrease at lower relative humidity was mainly due to the increased ionic resistance of the membrane/ionomer as the performance differences after resistance correction were relatively small (Figure 2. 10b,c).

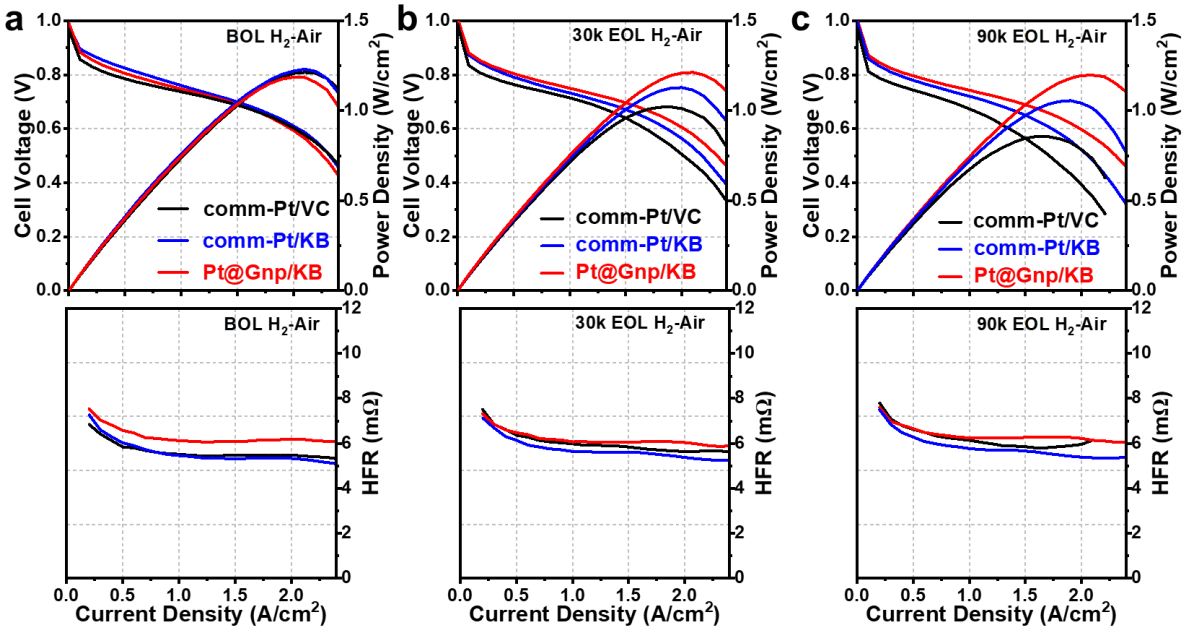

Figure 2. 9 Comparison of H_2/Air polarization plots and HFR of comm-Pt/KB, comm-Pt/VC, and Pt@Gnp/KB catalysts at (a) BOL, (b) EOL after 30k AST cycles, and (c) after EOL 90k AST cycles.

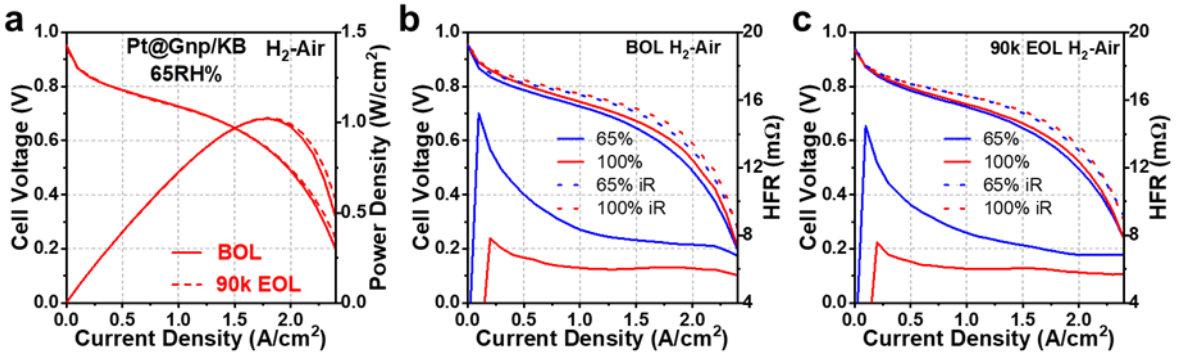

Figure 2. 10 H_2-air performance at lower relative humidity of 65 RH% relevant to heavy-duty application. (a) H_2-air polarization curves at BOL and EOL after 90,000 AST cycles under 65 RH%. Noted that the outstanding durability with negligible performance loss was still preserved and the performance difference after iR correction was relatively small.

As the fuel cells must meet performance requirements throughout their service lifetime, the EOL performance represents the critical metrics ultimately dictating the amount of Pt required in the cathode.[3] Therefore, the M2FCT has established a targeted EOL performance of 1.07 A/cm^2 at 0.7 V after an AST equivalent to 25,000 hours.[33] With the durable Pt@Gnp/KB catalyst, a high EOL performance of 1.375 ± 0.056 A/cm^2 at 0.7 V (Figure 2. 11) is achieved after 90,000 cycles, notably higher than that of the comm-Pt/KB (1.213 ± 0.060 A/cm^2) and comm-Pt/VC catalysts

(0.827 ± 0.016 A/cm^2). In general, the Pt@Gnp/KB catalyst demonstrates remarkably higher EOL performance throughout the entire LCD and HCD regions than comm-Pt/KB and comm-Pt/VC catalysts, which is essential for HDV applications.

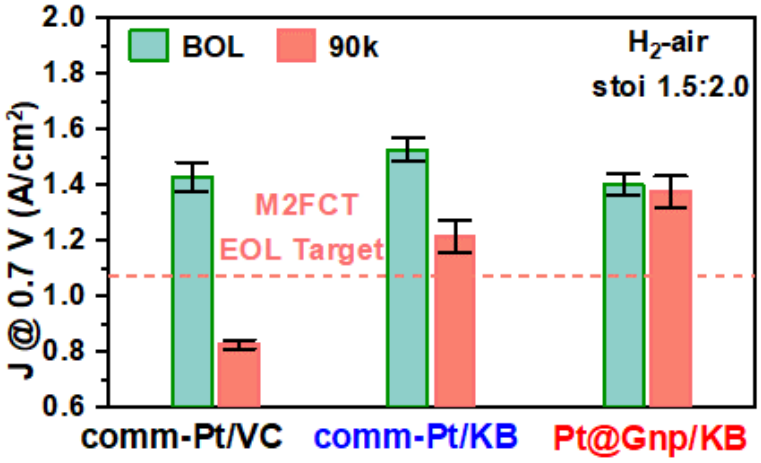

Figure 2. 11 Comparison of current density at 0.7 V of comm-Pt/KB, comm-Pt/VC, and Pt@Gnp/KB catalysts at BOL and 90k EOL. The red dash line indicates the M2FCT target of 1.07 A/cm^2 at 0.7V at EOL after 25000-hour-equivalent AST. All error bars represented standard deviation with the middle as the averaged value derived from at least two independent test.

The outstanding catalyst performance and unprecedented durability make the Pt@Gnp/KB catalyst well suited for addressing the efficiency and lifetime challenges of HDV applications. To reflect the enhancement in peak efficiency as well as its retention with the Pt@Gnp/KB catalyst, we adopt the concept of voltage efficiency, which is defined as the actual cell operating voltage divided by the thermodynamic voltage from the lower heating value (LHV) of hydrogen (1.25 V).[40,43] The operating voltage that gives the peak efficiency is achieved during low-power mode (e.g., during idling or cruising), and is calculated based on a representative Class 8 HDV with a 275 kW fuel cell system and a 20 kW idle power (Figure 2. 12a).[3,13,14] Our analysis shows that the fuel cell with Pt@Gnp/KB catalyst exhibits the highest initial peak efficiency of 71.9%, comparable with the comm-Pt/KB (71.9%) and higher than the comm-Pt/VC (69.0%) catalysts, and represents the only catalyst that exceeds the DOE 2050 ultimate efficiency target for HDV (Figure 2. 12b).[8] Impressively, the Pt@Gnp/KB catalyst suffers a much smaller loss in efficiency

of 2.0% after 90,000 AST cycles, in comparison with 4.1% for comm-Pt/KB and 5.2% for comm-Pt/VC catalysts, respectively. Such a high initial efficiency and outstanding retention is essential for a high fuel economy, which is particularly crucial for HDV with a long traveling distance and high operational cost.[10,11]

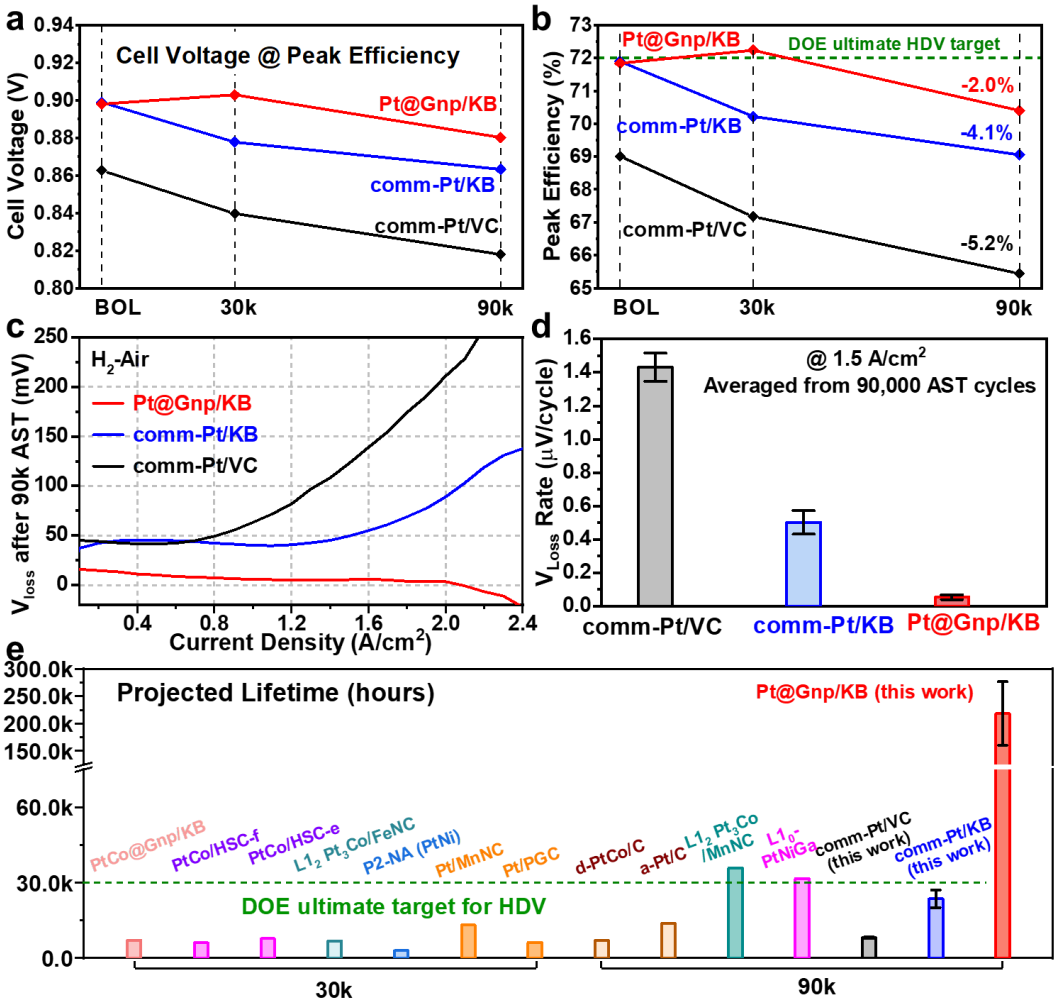

Figure 2. 12 Fuel cell efficiency and lifetime projection. (a) Cell voltage at low-power operation mode that gives the peak cell efficiency. Calculated based on a representative Class 8 HDV with a 275 kW fuel cell system and a 20 kW idle power. (b) The fuel cell peak voltage efficiency, calculated from the cell voltage at idle power and the LHV of hydrogen at 94 °C (1.25 V). (c) The voltage loss after 90k AST cycles versus current density. (d) The voltage degradation rate during square wave AST cycling, calculated from the voltage loss at 1.5 A/cm^2 where the rated power is delivered. (e) The comparison of the projected lifetime between Pt@Gnp/KB catalyst and the state-of-the-art catalysts reported in the literature: PtCo@Gnp;[28] PtCo/HSC-e, PtCo/HSC-f;[32] $L1_2$ Pt_3Co/Fe-N-C;[23] PtNi P2-NA;[22] Pt/PGC, Pt/MnNC;[31] $L1_0$ CoPt/Pt;[25] catalysts for HDV applications: d-PtCo/C, a-Pt/C;[34] $L1_2$ Pt_3Co/MnNC;[35] $L1_0$ PtNiGa.[36] The comparison clearly shows the excellent durability of the developed Pt@Gnp/KB catalyst. All error bars represented standard deviation with the middle as the averaged value derived from at least two independent tests.

Besides the efficiency challenge, the most substantial challenge for fuel-cell-driven HDVs is the long lifetime requirement.[8] To further demonstrate the stability advantage of the developed catalyst, the voltage losses after 90,000 AST cycles throughout the whole current density regions are plotted (Figure 2. 12c). Notably, the Pt@Gnp/KB catalyst exhibits a relatively small voltage loss of less than 20 mV throughout the whole current density region up to 2.4 A/cm^2. In contrast, the comm-Pt/KB and comm-Pt/VC exhibited a much larger voltage loss exceeding 100 mV and 200 mV in the HCD region, respectively.

To project the lifetime of the tested MEA, we compared the voltage degradation rate at 1.5 A/cm^2 where the rated power is typically delivered. Impressively, the Pt@Gnp/KB catalyst only loses 4.9 ± 1.2 mV at 1.5 A/cm^2 after 90,000 AST cycles, which translates into a degradation rate of only 0.054 ± 0.014 mV/cycle (Figure 2. 12d) that is over a order of magnitude lower than the comm-Pt/KB (0.502 ± 0.071 mV/cycle) and the comm-Pt/VC (1.430 ± 0.084 mV/cycle). As the square-wave AST testing protocol shows a hundred times acceleration over the drive-cycle,[37] this exceptional small degradation rate results in an ultralong projected lifetime of 218,000 ± 57,900 hours, far beyond those of the commercial catalysts (23,000 ± 3,500 hours for comm-Pt/KB and 8,000 ± 400 hours for comm-Pt/VC), and almost seven times of the DOE 2050 ultimate lifetime target of 30,000 hours for HDV.[8] To the best of our knowledge, our Pt@Gnp/KB catalyst outperforms all the state-of-the-art catalysts reported to date (Figure 2. 12e), and thus represents a highly promising candidate for heavy-duty fuel cell applications. We also explored the potential of Pt@Gnp/KB catalyst in mitigating the start-up/shut-down (SU/SD) degradation due to the mixed H_2 and air in anode. Interestingly, by applying Pt@Gnp/KB as either anode or cathode catalyst, we observed much improved durability against SU/SD degradation after 15 cycles of simulated SU/SD events (Figure 2. 13).

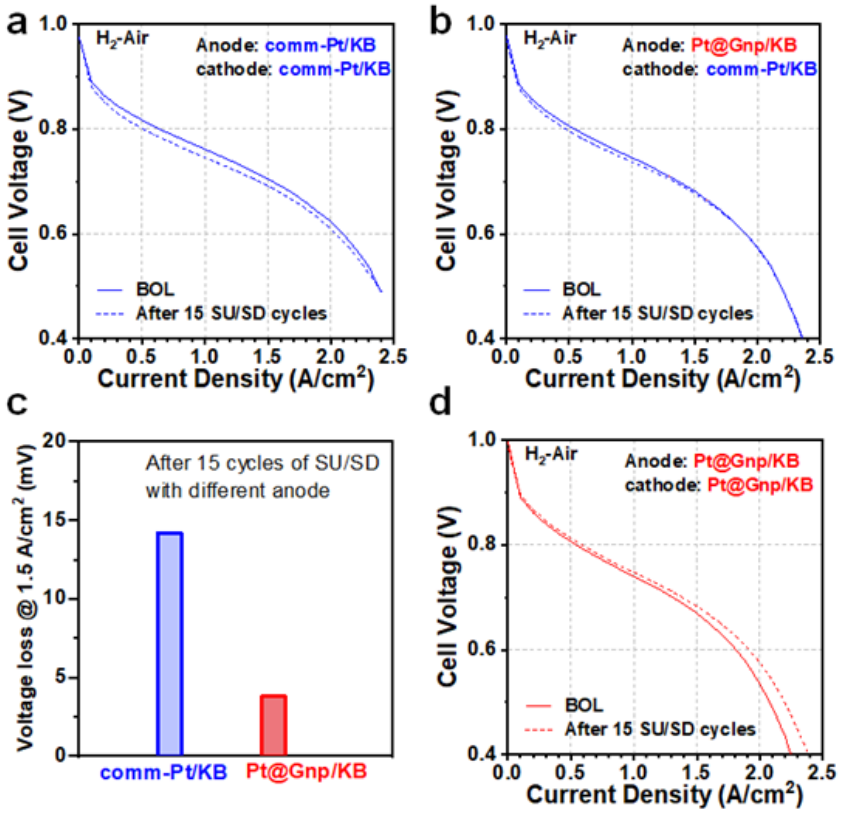

Figure 2. 13 SU/SD tests in MEA with different anode and cathode catalysts. (a) anode and cathode both using commercial Pt/KB, (b) anode using Pt@Gnp/KB and cathode using commercial Pt/KB, (c) comparison of their voltage loss at 1.5 A/cm^2 after 15 SU/SD cycles. (d) cathode and anode both using Pt@Gnp/KB.

The outstanding durability of the Pt@Gnp/KB catalyst is validated by post-AST characterizations and size analysis. HR-STEM imaging and the EELS mapping clearly revealed that the graphene protective layer in the Pt@Gnp/KB was still intact after 90,000 AST cycles (Figure 2. 14). The TEM studies of the catalysts after 90,000 AST cycles reveal that the Pt@Gnp/KB catalyst exhibits a much more uniform distribution (Figure 2. 15a) than both commercial catalysts (Figure 2. 15 b,c). The size analysis shows that the Pt@Gnp/KB catalyst retains a relatively narrow size distribution at EOL with an average size of 5.4 ± 1.1 nm (Figure 2. 15d), which is only a half of the comm-Pt/KB (8.9 ± 4.5 nm, Figure 2. 15e) and comm-Pt/VC catalysts (10.6 ± 6.8 nm, Figure 2. 15f). In addition, it is noted that the comm-Pt/KB and comm-

Pt/VC catalysts show a rather a broad distribution with a heavy tailing, indicating severe Ostwald ripening and particle coalescence.[44]

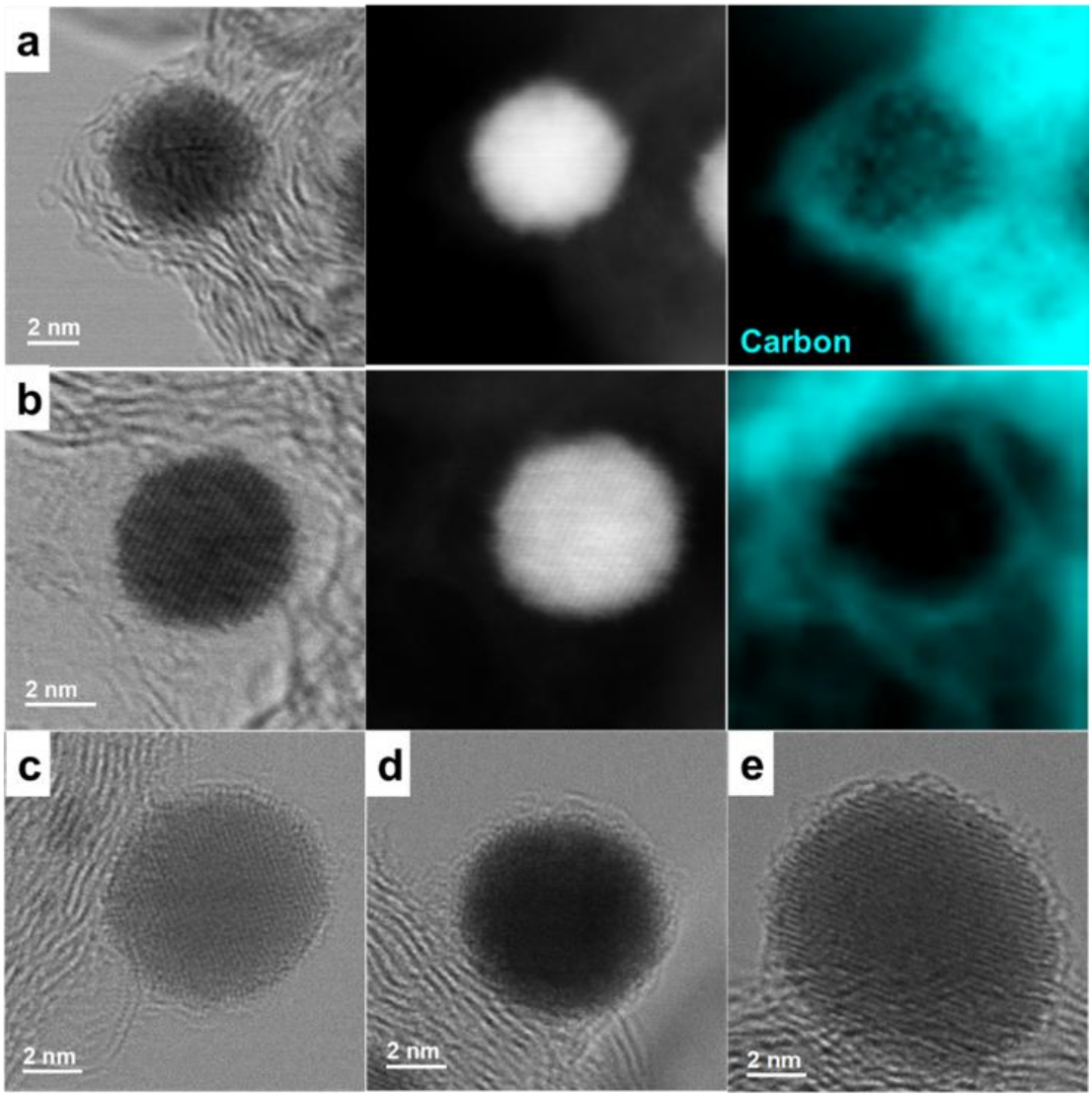

Figure 2. 14 Bright field, dark field STEM and carbon EELS mapping images at different surface locations after 90,000 AST cycles showing that the Pt@Gnp/KB structure is still preserved.

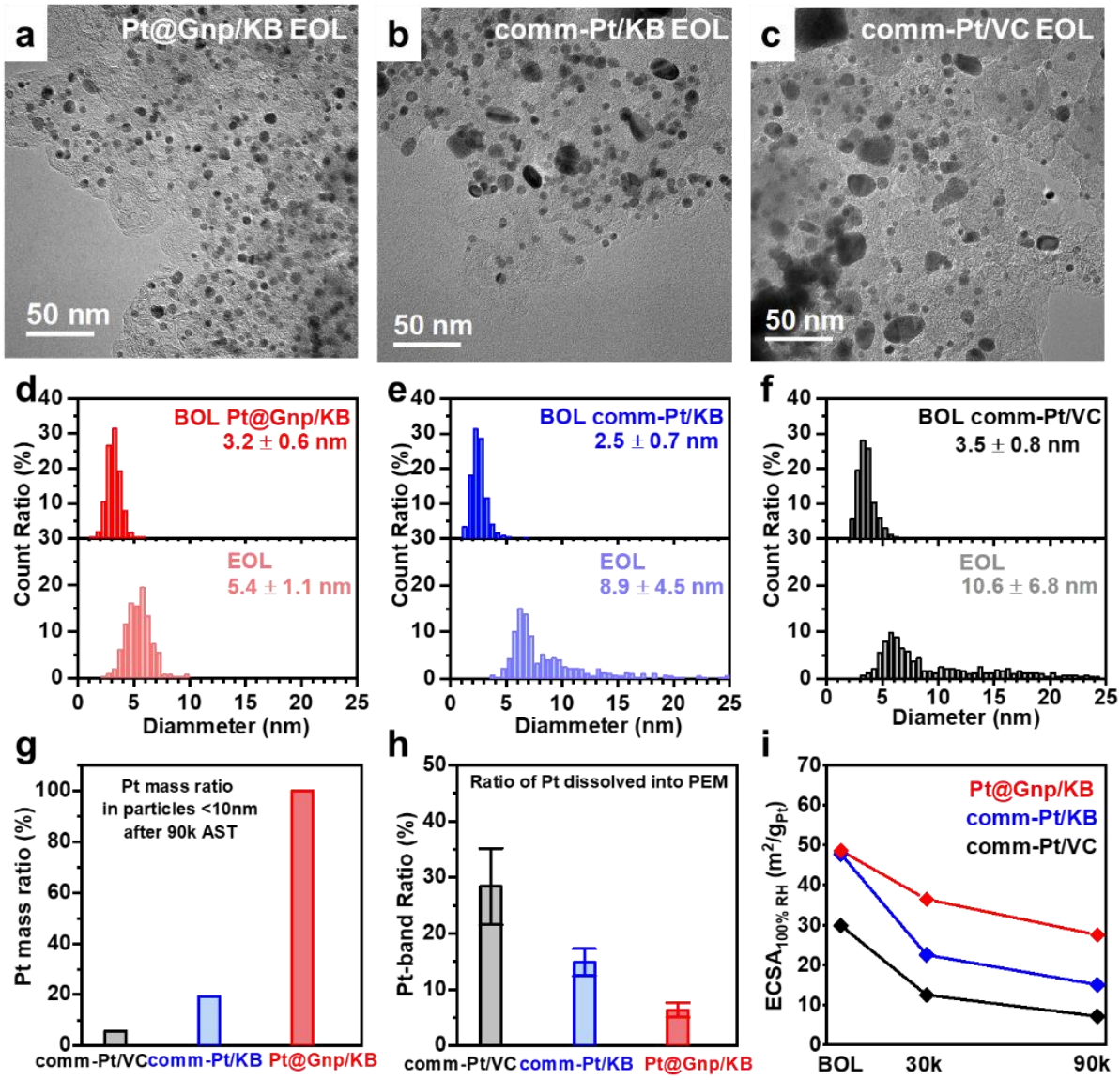

Figure 2. 15 Characterization of catalysts at EOL, analysis of size distribution, and corresponding MEA test results. TEM images of (a) Pt@Gnp/KB, (b) comm-Pt/KB, and (c) comm-Pt/VC at 90k EOL. Corresponding number-based particle size analysis of (d) Pt@Gnp/KB, (e) comm-Pt/KB, and (f) comm-Pt/VC at BOL and 90k EOL. (g) Ratio of Pt mass in particles with size smaller than 10 nm at 90k EOL. (h) Comparison of Pt-band ratio, which reflected the degree of Pt dissolution into the PEM. (i) ECSA from CO stripping experiments at 80 °C, ambient pressure under 100% RH.

Notably, we conducted size analysis after MEA activation and BOL test (Figure 2. 16), it was found that while the Pt@Gnp/KB still maintained the initial size and distribution, the size of the commercial catalysts had already grown considerably (from 2-4 nm to 5-6 nm), consistent with previous studies.[45] In addition to the particle number-based size distribution, a mass-weighted EOL size distribution is plotted to show the Pt mass distribution in different sizes of particle (Figure 2.

17, Figure 2. 18).[46] The result shows that the Pt@Gnp/KB catalyst still has the majority of Pt mass distributed in relatively small particle size (mass-weighted averaged diameter: 6.1 ± 1.2 nm), and almost all particles are still below 10 nm (Figure 2. 15g, Figure 2. 18). On the contrary, in the comm-Pt/KB and comm-Pt/VC catalysts, over 80% of Pt mass are originated from large particles with over 10 nm in size (Figure 2. 15g, Figure 2. 18). In addition to the size growth and particle agglomeration, we further characterized the Pt dissolution during AST by analyzing the Pt-band formed at the membrane interface (Figure 2. 15h, Figure 2. 19).[47] The results showed that Pt@Gnp/KB had much reduced Pt dissolution with a Pt-band ratio of only 6.4 ± 1.3%, significantly smaller than comm-Pt/KB of 14.9 ± 2.4% and comm-Pt/VC of 28.4 ± 6.8% (Figure 2. 15h).

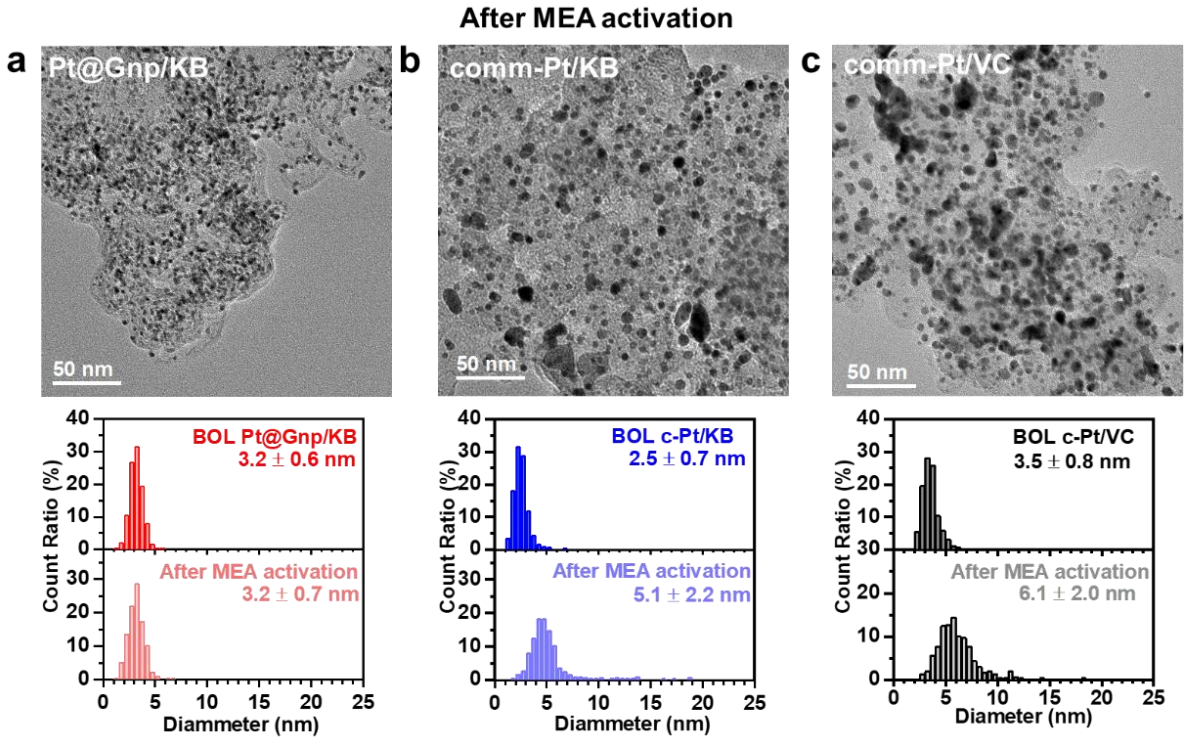

Figure 2. 16 Comparison of TEM images after MEA activation, and comparison of Pt size distribution and corresponding averaged size at BOL and after MEA activation of the (a) Pt@Gnp/KB, (b) comm-Pt/KB, and (c) comm-Pt/VC catalysts. Note that the particle size of commercial catalysts increased significantly even after MEA activation.

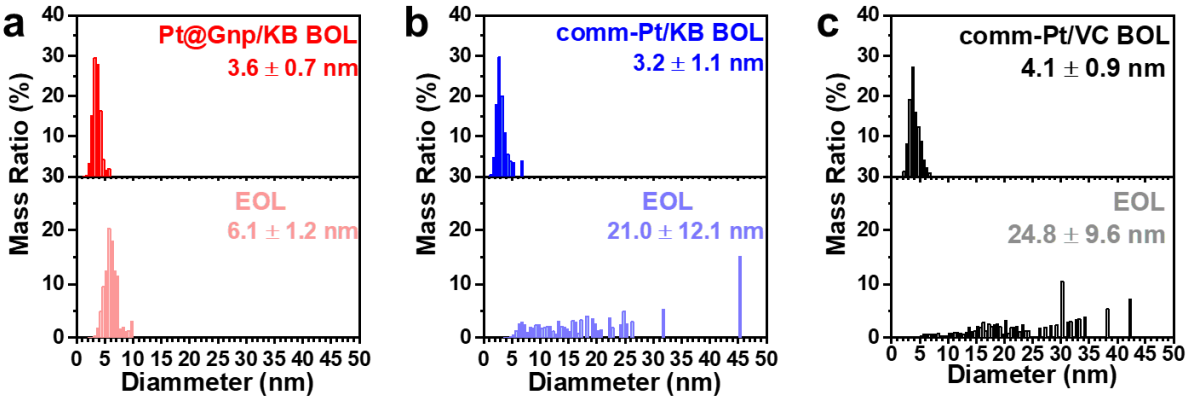

Figure 2. 17 Comparison of Pt mass-weighted size distribution and corresponding averaged size at BOL and at 90k EOL of the (a) Pt@Gnp/KB, (b) comm-Pt/KB, and (c) comm-Pt/VC catalysts.

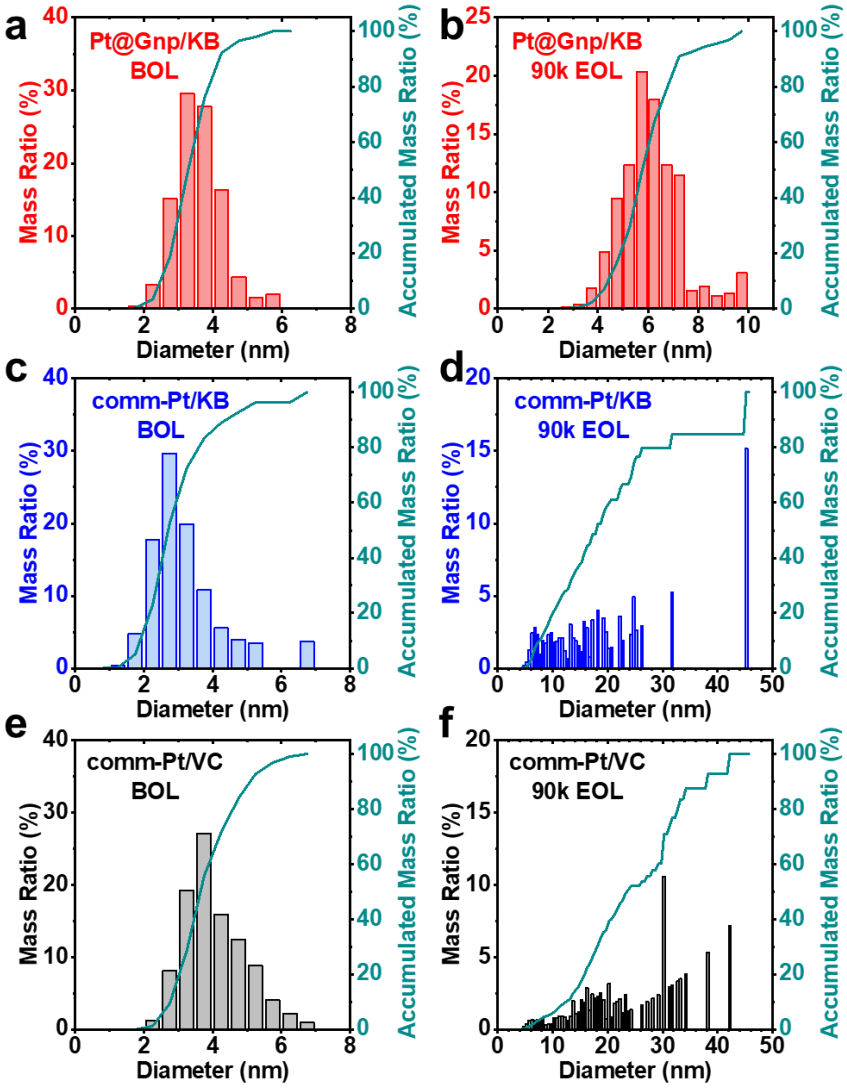

Figure 2. 18 Pt mass-weighted size distribution with accumulated mass ratio at BOL and 90k EOL of the (a-b) Pt@Gnp/KB, (c-d) comm-Pt/KB, and (e-f) comm-Pt/VC catalysts.

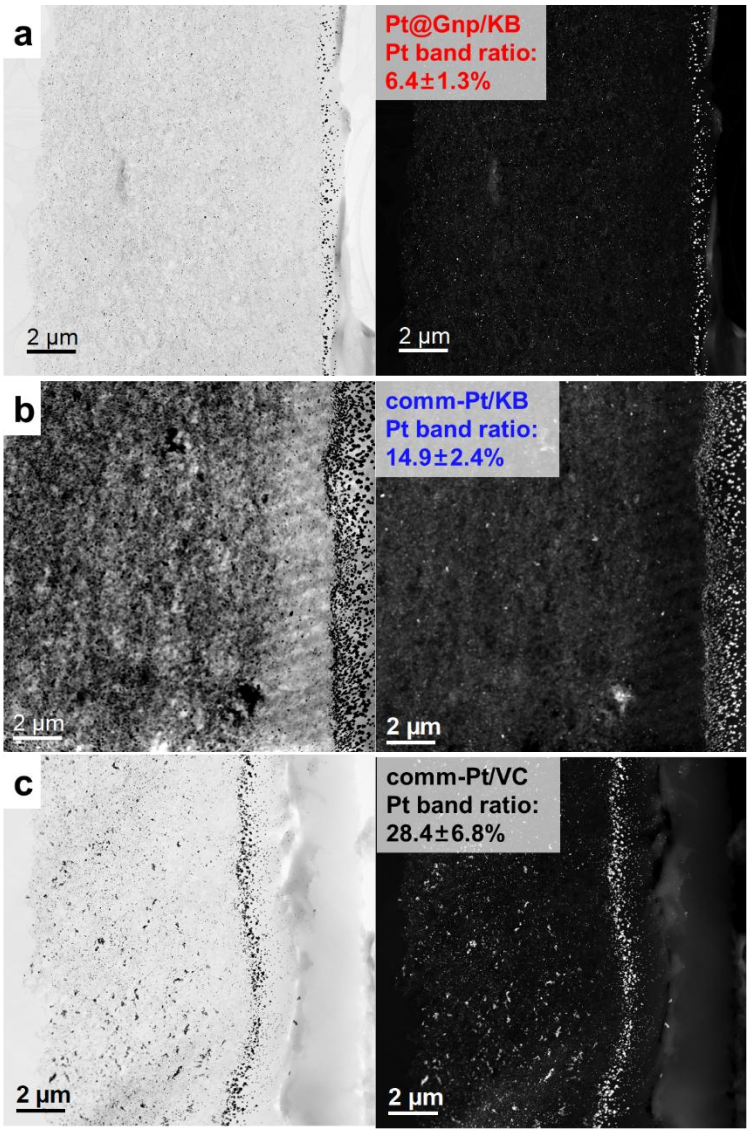

Figure 2. 19 Bright field and dark field STEM 90k EOL MEA cross-section images of (a) Pt@Gnp/KB, (b) comm-Pt/KB, and (c) comm-Pt/VC catalysts. The Pt band (selected by the teal box) ratio was averaged from at least five different MEA cross section regions, the error bar represented the standard deviation.

In addition, the cross-section images provided a broader view that showed much severer agglomeration and size growth in commercial samples compared to Pt@Gnp/KB across the catalyst layer (Figure 2. 19). As the result, the Pt@Gnp/KB catalyst exhibits highest EOL ECSA of 27.5 m^2/g_{Pt}, which is 83% and 287% higher than the comm-Pt/KB (15.0 m^2/g_{Pt}) and comm-Pt/VC (7.1 m^2/g_{Pt}) catalysts (Figure 2. 15i). Interestingly, it was also found that, in commercial catalysts without graphene protective layer, the ECSA loss ratio generally matched the MA loss

ratio (Figure 2. 20a), while much lower MA loss ratio was observed in Pt@Gnp/KB, leading to higher specific activity after AST (Figure 2. 20b). More importantly, by probing the fraction of Pt surface in direct or close contact with the ionomer, it was found that the Pt@Gnp/KB showed a much smaller ratio compared to commercial catalysts (Figure 2. 20c). This result is further validated with direct quantification of sulfonate group coverage on the Pt surface using CO-displacement experiment,[38,39] in which the Pt@Gnp/KB catalyst showed a low sulfonate group coverage of 3-6%, significantly lower than the typical coverage of 16% for unprotected Pt catalysts as well as ~12% for carbon coated Pt catalyst (Figure 2. 21).[39] These distinctive behaviors could be explained by the mitigation of ionomer poisoning effect on Pt specific activity by the graphene protective layer,[48] which stayed intact after 90,000 AST cycles (Figure 2. 14). These results support the remarkable fuel cell durability of our Pt@Gnp/KB catalyst, and suggest that the protection from the graphene nanopocket have effectively retarded the Ostwald ripening, particle coalescence, and poisoning effects in the Pt@Gnp/KB catalyst.

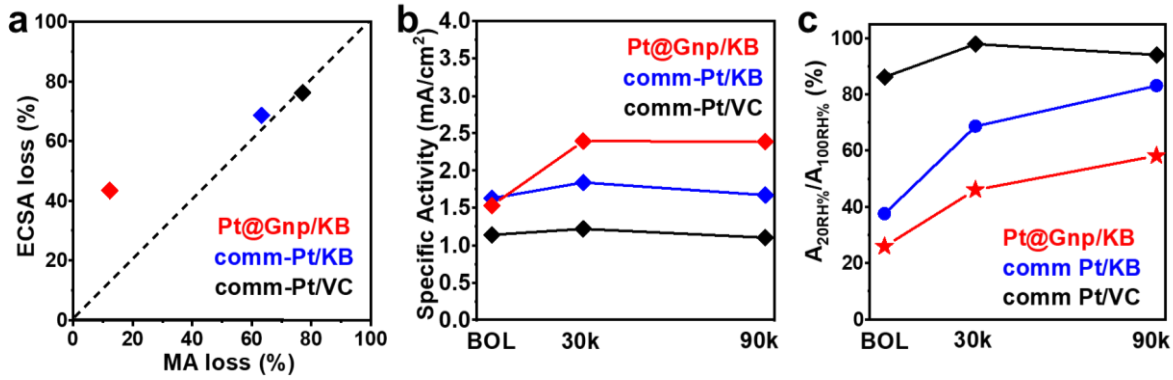

Figure 2. 20 (a) Relation of MA loss percentage and ECSA loss percentage. The less MA loss in Pt@Gnp/KB indicates that the specfic activity of Pt@Gnp/KB increased due to the mitigation of ionomer poisoning after AST. (b) MEA specific activities at BOL, 30k, and 90k EOL of Pt@Gnp/KB, comm-Pt/KB, and comm-Pt/VC catalysts. (c) Ratios of CO-stripping peak area of 20RH% and 100RH%, indicating the degree of close contact with ionomer and thus the degree of ionomer poisoning effect.

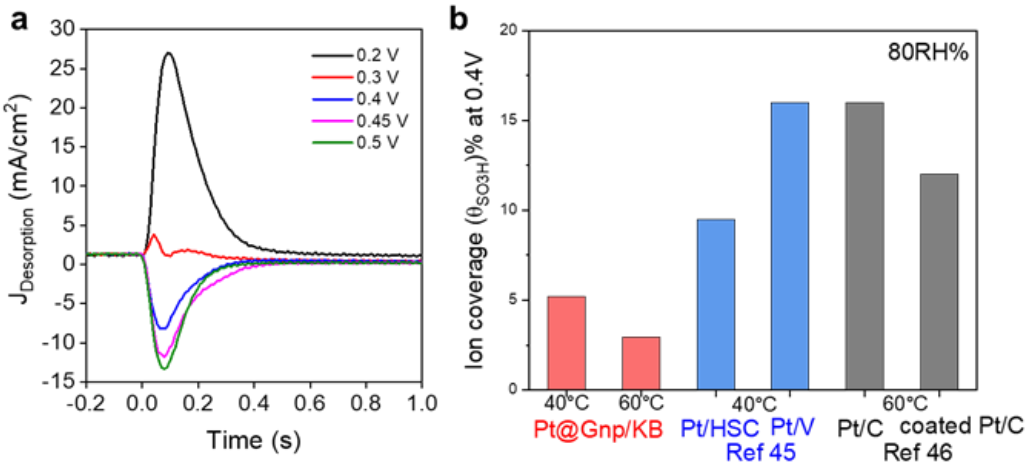

Figure 2. 21 (a) CO-displacement experiments tested at different voltage in MEA to directly reflect the sulfonate group coverage on Pt catalyst and the degree of ionomer poisoning. (b) Comparison of the sulfonate group coverage at 0.4 V on Pt@Gnp/KB with representative reported values. Ref[38]: conducted at 40 °C, 80 RH%; Ref[39]: Conducted at 60 °C, 80 RH%. Note that under all conditions, the Pt@Gnp/KB catalyst showed a much smaller sulfonate group coverage, suggesting the highly uniform protection against ionomer poisoning.

2.4 Conclusion

In this work, we have reported a highly pore-confined and surface-protected Pt nanocatalyst that shows an exceptional durability for HDV applications. Impressively, our designed catalyst simultaneously delivered a high power density of 1.08 W/cm^2 and an unprecedented power retention of 98.9% even after an aggressive 90,000 square wave cycles AST. With this high power stability, we project a record-breaking fuel cell lifetime of over 200,000 hours which is over seven times of the DOE 2050 ultimate target for HDV based on an average voltage loss rate of only 0.054 μV/cycle. The outstanding catalyst durability can be attributed to the high degree of pore confinement and the protective role of the accessible graphene layer. In addition to the much reduced Pt dissolution and particle size growth, the protective graphene layer also mitigates ionomer poisoning, which led to an outstanding MA of 0.74 A/mg$_{Pt}$ and high MA retention of 87.8% despite over 40% ECSA loss. As a result, a satisfying cell efficiency of 71.9% was enabled. While the expansion of fuel cell technology is facing two persisting roadblocks of

durability and efficiency, our catalyst holds the greatest potential to improve the commercial viability of PEMFCs, particularly for heavy-duty applications.

2.5 References

1. U.S. Department of Energy, F. C. T. O. *Fuel Cell Technologies Office Multi-Year Research, Development, and Demonstration Plan*. (2017).
2. Satyapal, S. *Hydrogen and Fuel Cell Program Overview*. https://www.hydrogen.energy.gov/docs/hydrogenprogramlibraries/pdfs/review19/plenary_overview_satyapal_2019.pdf?Status=Master (2019).
3. Cullen, D. A. *et al.* New roads and challenges for fuel cells in heavy-duty transportation. *Nat. Energy* **6**, 462–474 (2021).
4. North American Council for Freight Efficiency. *Making Sense of Heavy-Duty Hydrogen Fuel Cell Tractors*. (2020).
5. *Average Annual Vehicle Miles Traveled by Major Vehicle Category*. (2020).
6. U.S. Environmental Protection Agency. *Inventory of U.S. Greenhouse Gas Emissions and Sinks: 1990-2019 – Data Highlights*. (2021).
7. Davis, S. C. & Boundy, R. G. *Transportation Energy Data Book: Edition 40*. (Oak Ridge National Laboratory, 2020).
8. Marcinkoski, J. *et al. Hydrogen Class 8 Long Haul Truck Targets*. (2019).
9. Hunter, C. *et al. Spatial and Temporal Analysis of the Total Cost of Ownership for Class 8 Tractors and Class 4 Parcel Delivery Trucks*. www.nrel.gov/publications. (2021).
10. James, B. D., Huya-Kouadio, J. M., Houchins, C. & Desantis, D. A. *Mass Production Cost Estimation of Direct H2 PEM Fuel Cell Systems for Transportation Applications: 2018 Update*. (2018).

11. Hua, T. *et al.* Status of hydrogen fuel cell electric buses worldwide. *J. Power Sources* **269**, 975–993 (2014).

12. Kodama, K., Nagai, T., Kuwaki, A., Jinnouchi, R. & Morimoto, Y. Challenges in applying highly active Pt-based nanostructured catalysts for oxygen reduction reactions to fuel cell vehicles. *Nat. Nanotechnol.* **16**, 140–147 (2021).

13. Kurtz, J., Sprik, S., Saur, G. & Onorato, S. *Fuel Cell Electric Vehicle Driving and Fueling Behavior*. (2019).

14. Lohse-Busch, H. *et al.* Automotive fuel cell stack and system efficiency and fuel consumption based on vehicle testing on a chassis dynamometer at minus 18 °C to positive 35 °C temperatures. *Int. J. Hydrogen Energy* **45**, 861–872 (2020).

15. Mufan Li *et al.* Ultrafine jagged platinum nanowires enable ultrahigh mass activity for the oxygen reduction reaction. *Science* **354**, 1410–1414 (2016).

16. Escudero-Escribano, M. *et al.* Tuning the activity of Pt alloy electrocatalysts by means of the lanthanide contraction. *Science* **352**, 73–76 (2016).

17. Zhang, L. *et al.* Platinum-based nanocages with subnanometer-thick walls and well-defined, controllable facets. *Science* **349**, 412–416 (2015).

18. Li, W., Chen, Z., Xu, L. & Yan, Y. A solution-phase synthesis method to highly active Pt-Co/C electrocatalysts for proton exchange membrane fuel cell. *J. Power Sources* **195**, 2534–2540 (2010).

19. Wang, X. X. *et al.* Ordered Pt3Co Intermetallic Nanoparticles Derived from Metal-Organic Frameworks for Oxygen Reduction. *Nano Lett.* **18**, 4163–4171 (2018).

20. He, D. S. *et al.* Ultrathin Icosahedral Pt-Enriched Nanocage with Excellent Oxygen Reduction Reaction Activity. *J. Am. Chem. Soc.* **138**, 1494–1497 (2016).

21. Chung, D. Y. *et al.* Highly Durable and Active PtFe Nanocatalyst for Electrochemical Oxygen Reduction Reaction. *J. Am. Chem. Soc.* **137**, 15478–15485 (2015).

22. Han, B. *et al.* Record activity and stability of dealloyed bimetallic catalysts for proton exchange membrane fuel cells. *Energy Environ. Sci.* **8**, 258–266 (2015).

23. Qiao, Z. *et al.* Atomically dispersed single iron sites for promoting Pt and Pt3Co fuel cell catalysts: Performance and durability improvements. *Energy Environ. Sci.* **14**, 4948–4960 (2021).

24. Yang, C.-L. *et al.* Sulfur-anchoring synthesis of platinum intermetallic nanoparticle catalysts for fuel cells. *Science* **374**, 459–464 (2021).

25. Li, J. *et al.* Hard-Magnet L10-CoPt Nanoparticles Advance Fuel Cell Catalysis. *Joule* **3**, 124–135 (2019).

26. Song, T. W. *et al.* Small molecule-assisted synthesis of carbon supported platinum intermetallic fuel cell catalysts. *Nat. Commun.* **13**, (2022).

27. Gao, C., Lyu, F. & Yin, Y. Encapsulated Metal Nanoparticles for Catalysis. *Chem. Rev.* **121**, 834–881 (2021).

28. Zhao, Z. *et al.* Graphene-nanopocket-encaged PtCo nanocatalysts for highly durable fuel cell operation under demanding ultralow-Pt-loading conditions. *Nat. Nanotechnol.* **17**, 968–975 (2022).

29. Ji, S. G., Kwon, H. C., Kim, T. H., Sim, U. & Choi, C. H. Does the Encapsulation Strategy of Pt Nanoparticles with Carbon Layers Really Ensure Both Highly Active and Durable Electrocatalysis in Fuel Cells? *ACS Catal.* **12**, 7317–7325 (2022).

30. Tang, H. *et al.* Low Pt loading for high-performance fuel cell electrodes enabled by hydrogen-bonding microporous polymer binders. *Nat. Commun.* **13**, 7577 (2022).

31. Chen, M. *et al.* High-Platinum-Content Catalysts on Atomically Dispersed and Nitrogen Coordinated Single Manganese Site Carbons for Heavy-Duty Fuel Cells. *J. Electrochem. Soc.* **169**, 034510 (2022).

32. Ko, M., Padgett, E., Yarlagadda, V., Kongkanand, A. & Muller, D. A. Revealing the Nanostructure of Mesoporous Fuel Cell Catalyst Supports for Durable, High-Power Performance. *J. Electrochem. Soc.* **168**, 024512 (2021).

33. Borup, R. & Weber, A. *M2FCT: Million Mile Fuel Cell Truck Consortium*. (2021).

34. Wang, X., Hu, L., Neyerlin, K. C. & Ahluwalia, R. K. Baselining Activity and Stability of ORR Catalysts and Electrodes for Proton Exchange Membrane Fuel Cells for Heavy-Duty Applications. *J. Electrochem. Soc.* **170**, 024503 (2023).

35. Zeng, Y. *et al.* Regulating Catalytic Properties and Thermal Stability of Pt and PtCo Intermetallic Fuel-Cell Catalysts via Strong Coupling Effects between Single-Metal Site-Rich Carbon and Pt. *J. Am. Chem. Soc.* **145**, 17643–17655 (2023).

36. Liang, J. *et al.* Metal bond strength regulation enables large-scale synthesis of intermetallic nanocrystals for practical fuel cells. *Nat. Mater.* **23**, 1259–1267 (2024).

37. Garrick, T. R., Moylan, T. E., Carpenter, M. K. & Kongkanand, A. Editors' Choice—Electrochemically Active Surface Area Measurement of Aged Pt Alloy Catalysts in PEM Fuel Cells by CO Stripping. *J. Electrochem. Soc.* **164**, F55–F59 (2017).

38. Garrick, T. R., Moylan, T. E., Yarlagadda, V. & Kongkanand, A. Characterizing Electrolyte and Platinum Interface in PEM Fuel Cells Using CO Displacement. *J. Electrochem. Soc.* **164**, F60–F64 (2017).

39. Yamada, H., Kato, H. & Kodama, K. Cell Performance and Durability of Pt/C Cathode Catalyst Covered by Dopamine Derived Carbon Thin Layer for Polymer Electrolyte Fuel Cells. *J. Electrochem. Soc.* **167**, 084508 (2020).

40. Stariha, S. *et al.* Recent Advances in Catalyst Accelerated Stress Tests for Polymer Electrolyte Membrane Fuel Cells. *J. Electrochem. Soc.* **165**, F492–F501 (2018).

41. Kongkanand, A. & Mathias, M. F. The Priority and Challenge of High-Power Performance of Low-Platinum Proton-Exchange Membrane Fuel Cells. *J. Phys. Chem. Lett.* **7**, 1127–1137 (2016).

42. Barbir, F. *Fuel Cell Electrochemistry*. (Elsevier Academic Press, 2005).

43. Harrison, K. W., Remick, R., Martin, G. D. & Hoskin, A. *Hydrogen Production: Fundamentals and Case Study Summaries*. https://www.nlr.gov/docs/fy10osti/47302.pdf (2010).

44. Granqvist, C. G. & Buhrman, R. A. Size distributions for supported metal catalysts-Coalescence growth versus ostwald ripening. *J. Catal.* **42**, 477–479 (1976).

45. Borup, R. *et al. FC-PAD: Fuel Cell Performance and Durability Consortium*. https://energy.gov/eere/fuelcells/downloads/fuel-cell-technologies-office-multi-year-research-development-and-22 (2018).

46. Padgett, E. *et al.* Editors' Choice—Connecting Fuel Cell Catalyst Nanostructure and Accessibility Using Quantitative Cryo-STEM Tomography. *J. Electrochem. Soc.* **165**, F173–F180 (2018).

47. Peng, B. *et al.* Embedded oxide clusters stabilize sub-2 nm Pt nanoparticles for highly durable fuel cells. *Nat. Catal.* **7**, 818–828 (2024).

48. Lin, L.-C., Cheng, Y.-S., Liao, W.-C., Huang, Y.-H. & Pan, Y.-T. Transient Loss and Recovery of Platinum Fuel Cell Cathode Catalyst at High Voltage Efficiency Regimes. *J. Electrochem. Soc.* **168**, 054503 (2021).

Chapter 3. Sparsely Dispersed CeO_x-stablized Pt Nanoparticles Overcome Pt Loading-durability Trade-off for Highly Durable Heavy-duty Fuel Cells

3.1 Introduction

Proton-exchange-membrane fuel cell (PEMFCs) is an attractive zero-emission power generation technology.[1-3] Key priorities for the implementation of PEMFCs include reducing system cost and extending the lifetime, particularly for the emerging application in heavy-duty transportation.[2,4] Given that the catalyst accounts for ~ 40-60% of fuel cell stack cost, the central task to meet the priorities is to develop highly active and durable catalysts to reduce the usage of platinum group metal (PGM) catalysts throughout the lifetime.[5-7] However, achieving this target is fundamentally constrained by the intrinsic trade-off in PEMFCs, wherein catalysts with higher activity often exhibit reduced durability.[3]

We therefore start by analyzing the fuel cell performance requirement, their relation to the current-voltage polarization curve, and the implications on catalyst design principles (Figure 3. 1). In transportation applications, the driving pattern requires the fuel cell to be continuously switching between low-power cruising/idling mode and high-power acceleration mode.[8] Fuel cell performance in these modes is reflected by the current-voltage response in low-current-density (LCD) and high-current-density (HCD) regions, which are mainly limited by catalyst intrinsic activity (Figure 3. 1a, blue shaded area) and mass transport properties (Figure 3. 1a, orange shaded area), respectively. In particular, significant local oxygen transport resistance emerges near Pt surface and carbon/ionomer interface, which is closely correlated with the accessible electrochemical surface area (ECSA). However, under the repeated potential switching, the

catalyst layer undergoes multiple degradation pathways,[9] undermining the performance retention in both the LCD and HCD regions.

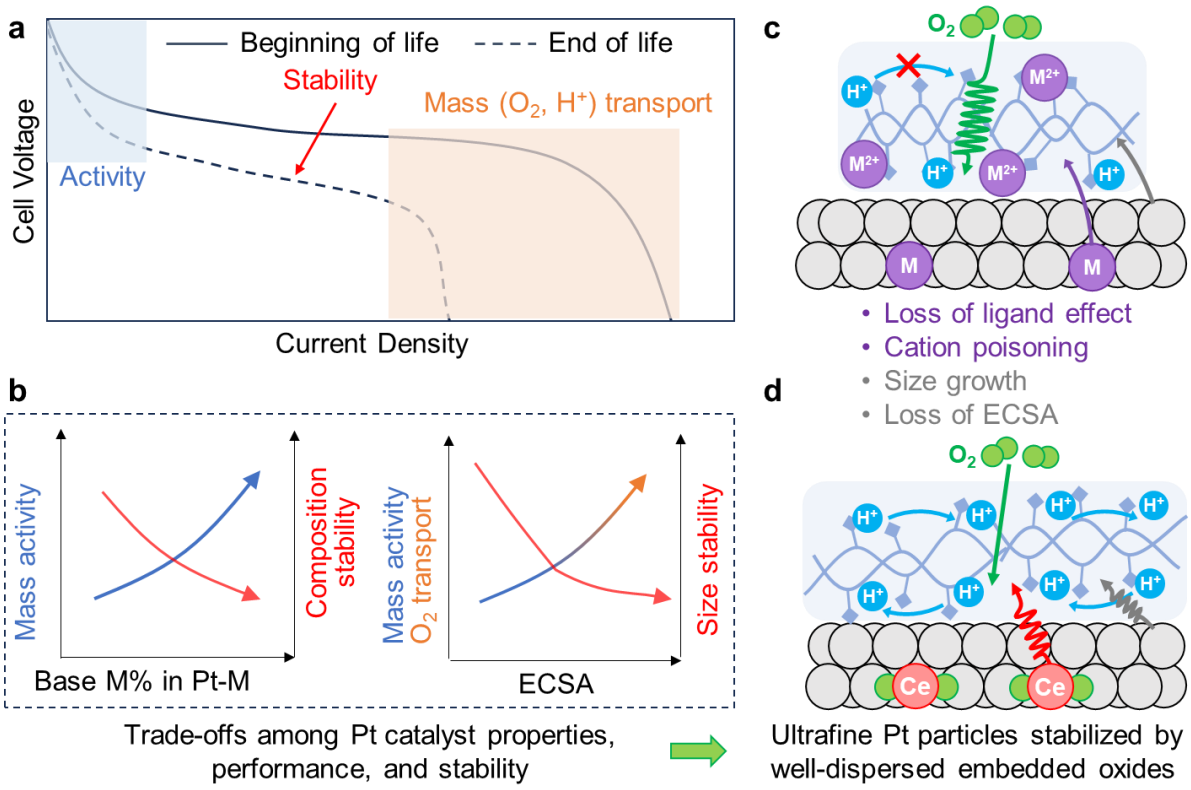

Figure 3. 1 Trade-off relation among Pt loading, catalyst activity and stability. (a) Typical polarization curve for evaluating fuel cell performance, in which the low and high current density regions are mainly impacted by the catalytic activity and mass transport properties, respectively. (b) The trade-off relations between catalyst properties (M%, ECSA), fuel cell performance (activity, mass transport), and the stability (composition, size). (c) Limitations in conventional Pt-alloy catalysts, and (d) the advantages of CeO_x@Pt catalyst design.

We further examined the key factors affecting the activity and stability of ORR properties in typical platinum-metal alloy (Pt-M) catalyst (M% composition, ECSA, etc.) (Figure 3. 1b). It is well-accepted that increasing the amount of alloying content and ECSA can benefit ORR mass activity and oxygen transport, but also bring more challenges in catalyst stability (morphology, composition and size, etc.). Although structurally ordered intermetallic Pt-M alloys have shown improved mass activity (MA) retention (> 60%) in LCD region,[10-12] the inevitable transition metal leaching rapidly degrades mass activity in LCD region and the associated cation poisoning effects

compromise the mass transport property in the HCD region,[2,13] resulting in an undesirable rated power loss (>10%) (Figure 3. 1c). Moreover, since the oxygen transport resistance is inversely proportional to the available Pt surface area (ECSA × Pt loading),[14] the stability challenge, especially power performance in HCD, exacerbates when the membrane electrode assembly (MEA) has an low PGM loading.[15] Thus, the ideal catalyst design strategy involves maximizing the ligand effect to boost specific activity, stabilize Pt atoms in an ultrafine particle to maximize the ECSA while minimizing the negative impact associated with metal leaching.

To this end, substantial effort has been devoted to developing stable Pt catalysts for HDVs.[16-22] Our previous study reported that embedded dispersed metal oxide (CoO_x, NiO_x, FeO_x) clusters can stabilize ultrafine Pt nanoparticles and enable high activity and stability in both LCD and HCD regions under light-duty-relevant testing conditions.[21] Nevertheless, we note that meeting the heavy-duty stability target (1.07 A/cm^2 at 0.7 V after a heavy-duty-relevant 90,000 square-wave cycles) with low-total-PGM-loading MEA (~0.1 mg_{PGM}/cm^2) remains a highly desirable but extremely challenging task in the community.

Aiming to further advance the catalyst design to address the stability challenge in heavy-duty application, we postulated that a stronger metal-oxide interaction could help further prevent Pt dissolution to further mitigate the potential leaching (Figure 3. 1d). We examined the trend in Pt-metal oxide interactions,[23] then identified CeO_x as a promising candidate owing to the stronger electron transfer and interaction between Pt and the oxygen vacancies due to the mixed $Ce^{3+/4+}$ state,[24,25] compared to the previously studied early transition metal oxides (CoO_x, NiO_x, FeO_x).

3.2 Methods

Materials and Chemicals

Platinum(II) acetylacetonate [$Pt(acac)_2$], aquivion D83-06A ionomer dispersion were purchased from Sigma Aldrich. Cerium(III) acetylacetonate [$Ce(acac)_3$], 10 wt% and 40 wt% commercial Pt/C (comm-Pt/C) were purchased from Alfa Aesar. 40 wt% commercial Pt/C with a size around 2 nm (comm-Pt/C-2nm) was purchased from Fuel Cell Store. Acetone and isopropanol (IPA) were purchased from Fisher Scientific. Proton-exchange membranes, Freudenberg H14C7 gas diffusion layer (GDL) and polytetrafluoroethylene (PTFE) gasket were purchased from Fuel Cell Store. Carbon support (Ketjenblack EC-300J) was purchased from Fitz Chem LLC. The water was Ultrapure Millipore (18.2 MΩ·cm).

Catalyst Preparation

Synthesis of CeO_x@Pt/C: The carbon support (Ketjenblack EC-300J) was activated in hydrogen (H_2)/argon (Ar) mixture before use as noted in the literature. A typical synthesis includes 150-180 mg carbon support, 150-170 mg $Pt(acac)_2$, 230-250 mg $Ce(acac)_3$, and 15 mL acetone were mixed under ultrasonication for 20 minutes. After acetone evaporation, the powder was collected, and then annealed in a quartz tube in Ar/H_2 mixed gas atmosphere, whereby the temperature is heated from room temperature (20 °C) to 200 °C and maintained at 200 °C for 8 hours. After annealing, the obtained catalyst powder was acid washed in N_2-saturated 0.05 M H_2SO_4 solution at 80 ºC for 12 h and washed with ultrapure water till the pH was neutral. The powder was thoroughly dried under vacuum and activated in H_2/Ar mixture at 180 °C for 1-2 h to obtain the final CeO_x@Pt/C catalyst.

Synthesis of CeO_x/C: CeO_x/C was synthesized following a similar procedure without the addition of $Pt(acac)_2$, the precursor-loaded powder was fast annealed at 800 ºC and the obtained powder was washed with acetone and water to remove unreacted precursor. The final Ce loading was found to be 4.7 wt% on carbon determined by ICP-AES.

Structure and Composition Characterization

Transmission electron microscopy (TEM) images were taken with Titan 80-300 TEM at 300 kV and also with JEOL JEM 2800 transmission electron microscope operated at 200 kV. Atomic resolution high angle annular dark-field (HAADF) images were taken using a JEOL Grand ARM300CF scanning/transmission electron microscopy (S/TEM) operated at 300 kV. Electron energy loss spectroscopy (EELS) and corresponding HAADF imaging were acquired using the quantum emitter electron nanomaterial microscope (QuEEN-M), a Spectra 300 STEM Thermo Fisher Scientific, located in the Center for Nanoscale Materials (CNM) at Argonne National Laboratory. The MEA cross-section samples were prepared with an ultramicrotome at thickness around 150 nm and were analyzed with a JEOL JEM 2800 transmission electron microscope operated at 200 kV. The fraction of Pt mass loss in the Pt band is calculated by integrating the Pt EDS peak from the Pt band region divided by the total Pt signal from the entire catalyst layer region (membrane plus cathode catalyst layer). The cross-section analyses were averaged from over 5 different regions in each sample. The composition of catalysts was determined by inductively coupled plasma atomic emission spectroscopy (ICP-AES, Shimadzu ICPE-9000).

X-ray Absorption Spectroscopy (XAS) Data Collection and Analysis

The electrode inks for the XAS electrodes were composed of 60% ethanol, 40% water, 5 wt % Nafion solution, and the catalyst powder. The XAS experiments were conducted at room temperature beamline 10-BM (MRCAT) at the Advanced Photon Source (APS). Data were collected on the same electrode in Fluorescence mode at the Pt L_3-edge and at the Ce L_3-edge. The data were processed and fitted using the Ifeffit−based Athena and Artemis programs. Scans were calibrated, aligned, and normalized with background removed using the IFEFFIT suite. The $\chi(R)$ were modeled using single scattering paths calculated by FEFF6.

Membrane Electrode Assemblies (MEA) Fabrication

The catalyst ink was made by mixing the catalysts with the ionomer solution (Aquivion D83-06A) and water-IPA solvent through ultrasonication. The catalyst ink was then spray-coated onto a reinforced perfluorosulfonic acid (PFSA) membrane (12 μm thickness) using a Sono-Tek ultrasonic spray system to form a catalyst-coated membrane (CCM).

For a fair comparison, cell components and fabrication conditions were the same in all MEAs except for the cathode catalysts. Accordingly, the MEAs were labeled by the cathode catalysts. The anode catalyst was the commercial 10% Pt/C with platinum group metal (PGM) loading fixed to be 0.01 mg_{PGM}/cm^2. The anode ionomer to carbon mass ratio was 0.6. The commercial 40% Pt/C (comm-Pt/C), commercial 40% Pt/C with a size around 2nm (comm-Pt/C-2nm) and physically mixed CeO_x/C and comm-Pt/C-2nm (CeO_x/C-Pt/C) were used as benchmark of cathode catalysts. The ionomer to carbon ratio was optimized to be 0.6 for comm-Pt/C and 0.7 for comm-Pt/C-2nm, CeO_x/C-Pt/C, and CeO_x@Pt/C. The cathode catalyst loading was controlled to be about 0.09 mg_{PGM}/cm^2. The PGM loading on anode/cathode were confirmed by the ICP-AES measurements. The fabricated CCM was dried under vacuum for an hour to evaporate the solvents. For the MEA fabrication, two gas diffusion layers (GDLs), two PTFE gaskets, and the prepared CCM were pressed together. The thickness of the PTFE gasket is 127 μm (5 mil). The thickness of GDL, which includes a microporous layer, is 175 μm (Freudenberg H14C7).

MEA Activity Tests

The MEA was loaded in 5 cm^2 single-cell fixture with serpentine flow field and tested in the Scribner 850e fuel cell test stand with automatic back pressure system. The MEAs were tested following a protocol similar to the one recommended by DOE Fuel Cell Performance and Durability Consortium (FC-PAD). Prior to the testing cycles, MEAs were stabilized and activated

by holding the voltage at 0.5 V under H_2/Air flow of 100/100 standard cubic centimeters per minute (sccm) at 80 °C, 100% relative humidity (RH), 150 kPa_{abs} (all pressure noted in this work refer to the absolute pressure). Then, the MEA was further activated at oversaturated conditions, where the fuel temperature was set at 80 °C for both cathode and anode before entering the cell (held at 60 °C). The mass activity (MA) tests were at 80 °C, 100% RH, 150 kPa_{abs} with a flow rate of 835 (H_2)/2000 (O_2) sccm.

The rated power at BOL and EOL was tested in Scribner 850e fuel cell fixture under 94 °C, 250 $kPa_{abs,}$ and 100% RH. The H_2/Air gas flow rate was 126/400 sccm, which is equivalent to the stoichiometry of 1.5/2.0 at 2.4 A/cm^2 (endpoint of current density plot).

All of the MEA's BOL and EOL performance metrics, such as MA, ECSA, and H_2 crossover, were recorded by the Scribner 850e fuel cell test station and the Scribner 885 potentiostat. The ECSA was determined by integrating the CO stripping peak, assuming 420 $\mu C/cm^2_{Pt}$. The CO stripping test in MEA followed the protocol in the literature.

MEA AST

For the accelerated stress test (AST), we adopted the more aggressive 90,000-cycle square wave protocol with each cycle holding the MEA at the voltage of 0.6 V for 3 seconds and then 0.95 V for 3 seconds. The full AST is carried at 80 °C, ambient pressure, 100% RH with H_2/N_2 flow 100/100 sccm for anode and cathode, respectively. We noted that our AST protocol followed the current M2FCT AST protocol for PGM-based catalysts, while new AST protocols are under development and validation.

Projection of Fuel Cell Pt Cost

The Pt cost ($/kW) was estimated following a reported model based on the EOL Pt power utilization performance (kW/g_{Pt}). We assume a Pt price of 50$/g and an active-to-total area ratio of 0.65.

Projection of Fuel Cell Lifetime

The fuel cell lifetime is defined as the total operation time until a 10% voltage loss is reached at maximum power. In our study, we use the current density of 1.5 A/cm^2 to be the study point. The lifetime of the tested MEA is then projected by Eq. 1 based on the voltage loss (V_{Loss}) rate at 1.5 A/cm^2. An acceleration factor of 100 (with respect to time) over the drive-cycle is used according to previous literature. Noted that a full square wave cycle takes 6 sec (0.6 V for 3 seconds and 0.95 V for 3 seconds).

$$Lifetime\ (hours) = \frac{10\% \times V_{inital}\ (mV)}{V\ Loss\ Rate\ \left(\frac{mV}{cycle}\right)} \times 6\left(\frac{sec}{cycle}\right) \times 100 \div 3600\left(\frac{sec}{hour}\right) \qquad \textbf{Eq. 1}$$

3.3 Results and Discussion

The designed CeO_x@Pt/C structure was prepared through a wet impregnation process involving the mixing of porous carbon with platinum acetylacetonate ($Pt(acac)_2$) and cerium acetylacetonate ($Ce(acac)_3$), followed by an annealing and acid wash step to achieve the designed CeO_x@Pt consisting dispersed CeO_x encapsulated within ultrafine Pt nanoparticles (See Methods for detail). STEM and high-resolution TEM (HRTEM) show that the CeO_x@Pt/C was well-dispersed on the carbon support (Figure 3. 2a, Figure 3. 3) with an average diameter of 1.5 ± 0.3 nm (Figure 3. 2b). XRD studies show a face-centered cubic (fcc) structure with broad peak profile (Figure 3. 2c), which corresponds to an average crystalline size of 1.2 nm from Scherrer equation, consistent with TEM studies.

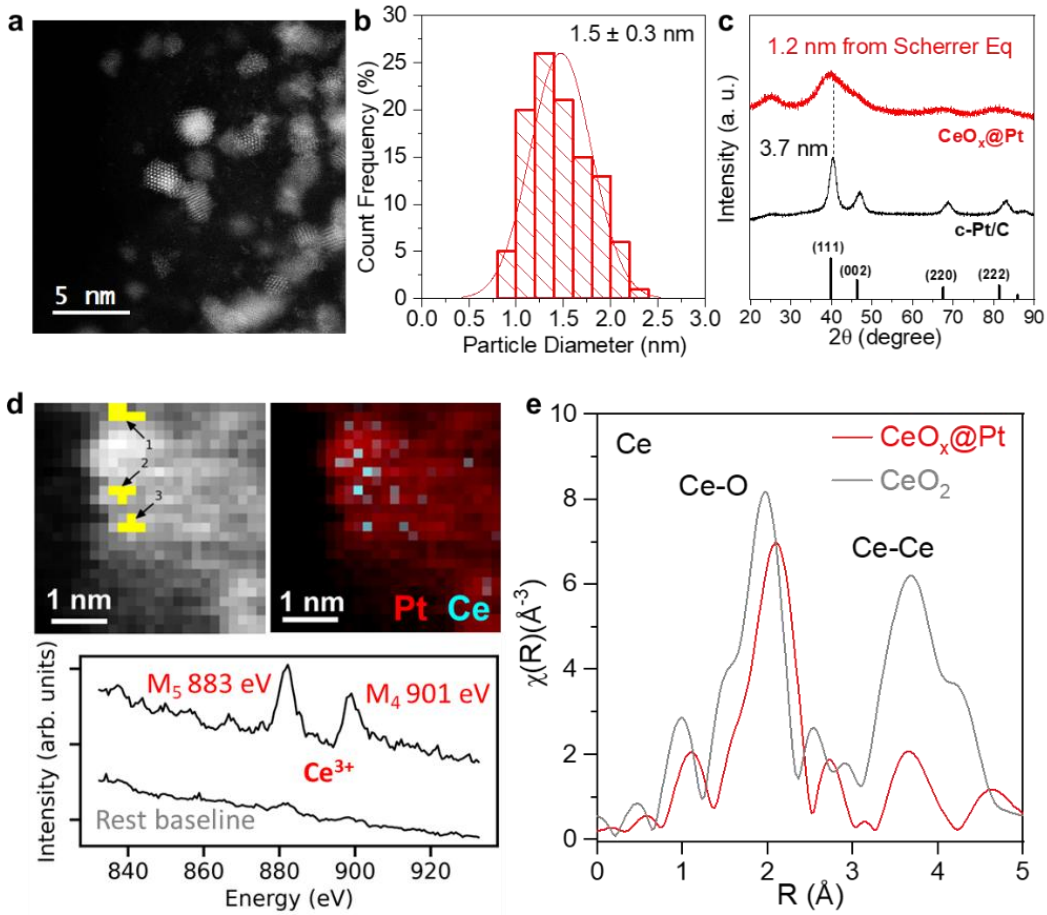

Figure 3. 2 Synthesis and structural characterization of CeO_x@Pt supported on carbon. (a) HAADF STEM images of the CeO_x@Pt/C nanocatalyst, (b) Corresponding size distributions and the averaged size measured in particle diameter. (c) XRD pattern of CeO_x@Pt/C and comm-Pt/C catalysts with averaged crystalline size calculated from Scherrer equation. (d) STEM-EELS elemental maps showing the sparsely dispersed Ce within the Pt nanoparticle, and the corresponding EELS spectrum from the Ce signal. (e) Fourier transform EXAFS of CeO_x@Pt/C collected at Ce edge.

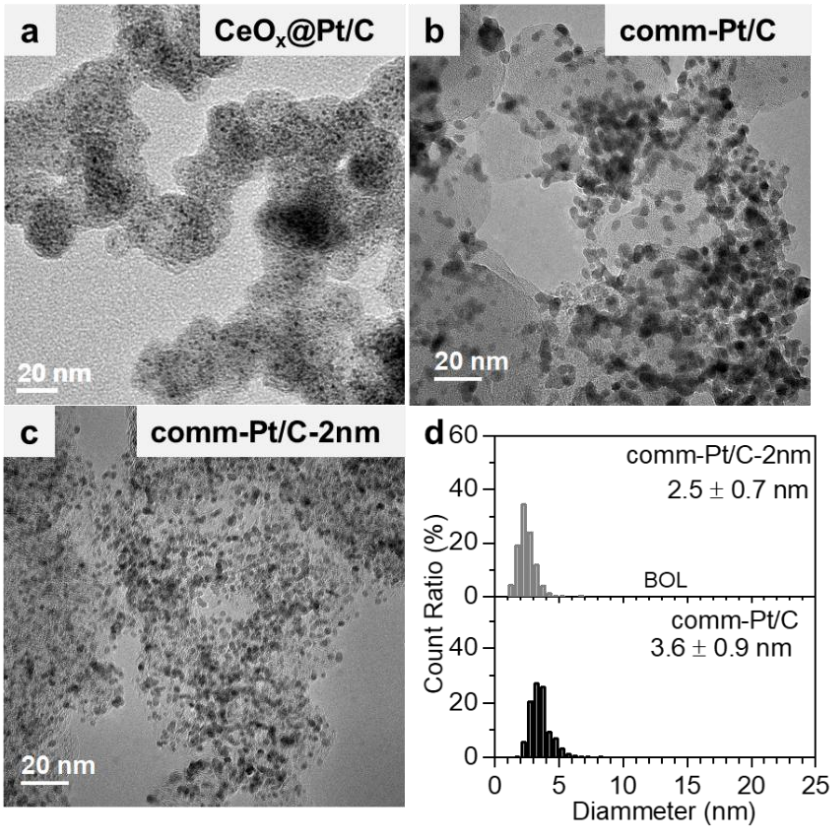

Figure 3. 3 TEM characterization of catalyst at beginning-of-life. (a) CeO_x@Pt/C, (b) comm-Pt/C, and (c) comm-Pt/C-2nm. (d) The size distribution of the catalysts at beginning-of-life and the corresponding average diameter. The values represent the mean size and the error bars represent the standard deviation.

The composition analysis via ICP-AES shows that the CeO_x@Pt/C has a Ce:Pt atomic ratio of 1.5:98.5 (Table 3. 1). The EELS mapping (Figure 3. 2d) and the corresponding spectra reveal that the Ce atoms are sparsely dispersed inside the nanoparticle and in the mixed form of $Ce^{3+/4+}$. We further conducted XAS studies to understand the local atomistic and electronic structures (Figure 3. 2e). The Ce L_3-edge X-ray absorption near-edge spectroscopy (XANES) result confirms the Ce is mainly in oxidized state and the shift to lower energy suggests the mixed oxidation state of $Ce^{3+/4+}$ (Figure 3. 4). The extended X-ray absorption fine structure (EXAFS) fitting results (Table 3. 2) reveal a much longer Ce-O bond length of 2.51 Å compared to 2.32 Å in CeO_2, further suggesting the presence of a lower oxidation state of Ce^{3+}, consistent with the XANES and EELS

result. The Ce-Ce interaction at 3.7 Å is also substantially suppressed, indicating that the CeO_x clusters are sparsely or possibly mostly atomically dispersed.

Sample	atomic % (Pt, Ce) Based on ICP-AES	
	Pt	Ce
CeO_x@Pt/C	98.5	1.5

Table 3. 1 Atomic ratios of Pt and Co in catalysts measured by ICP-AES.

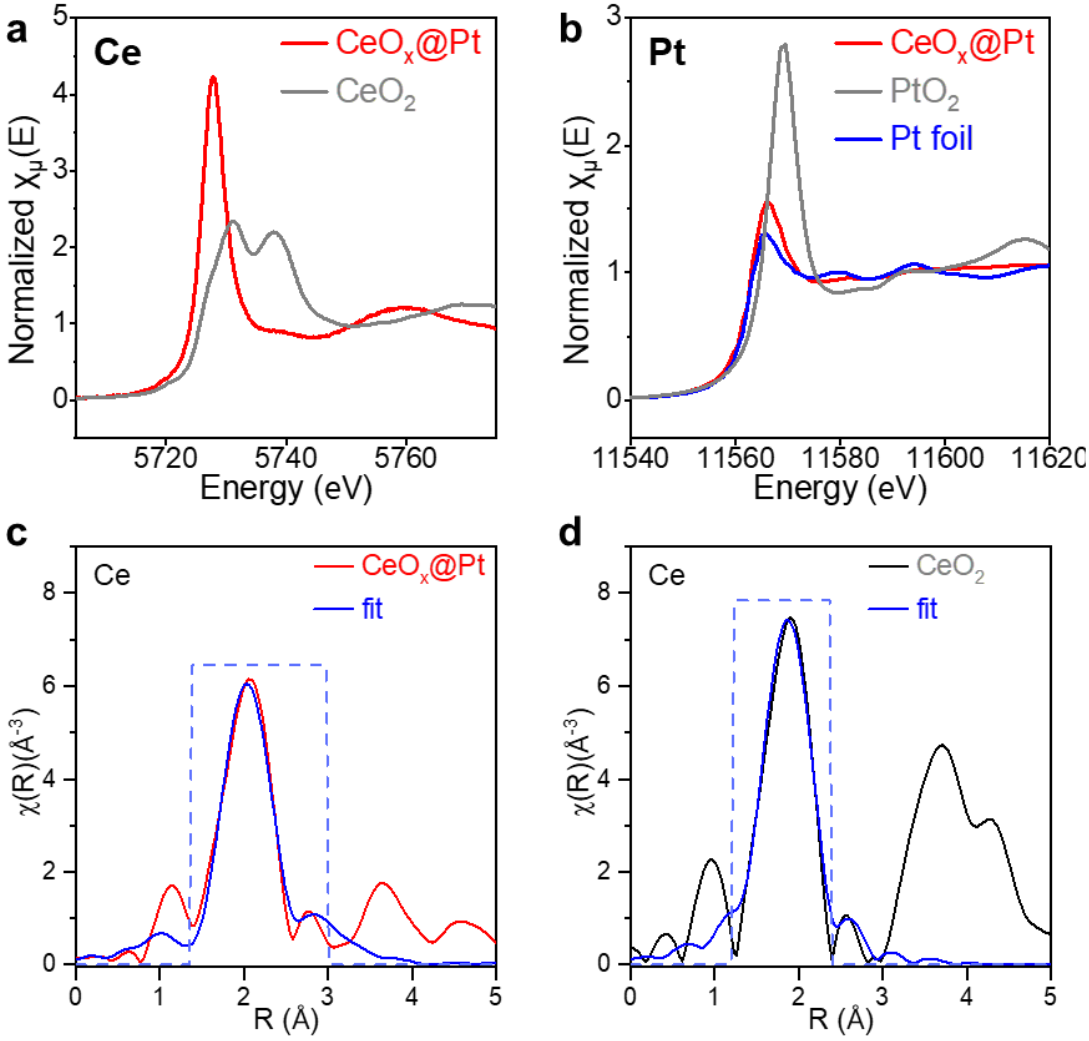

Figure 3. 4 XANES and EXAFS of the CeO_x@Pt samples. XANES at (a) Ce L_3-edge and (b) Pt L_3-edge. The lower Ce edge compared to CeO_2 indicates a lower oxidation state than +4, and the lack of the second peak indicates less Ce-Ce interaction. Ce-O fitting of the Fourier transform EXAFS spectrum at Ce L_3-edge of (a) CeO_x@Pt, and (b) CeO_2 reference.

Ce L-edge EXAFS fitting						
Sample	Scattering path	CN	R (Å)	σ^2 (10^{-3} Å^2)	E_0 (eV)	R factor
CeO_2	Ce-O	8±2	2.32±0.02	11±6	8±2	0.015
CeO_x@Pt/C		7±2	2.51±0.02	13±3	2±2	0.017

Table 3. 2 Summaries of structural parameters extracted from EXAFS fitting. Results from CeO_x@Pt at the Ce L_3-edge are compared to CeO_2 reference. CN is the coordination number; R is the interatomic distance (the bond length between Pt or Ce central atoms and surrounding coordination atoms); σ^2 is the Debye-Waller factor (a measure of thermal and static disorder in absorber-scatterer distances); E_0 is edge-energy shift (the difference between the zero kinetic energy value of the sample and that of the theoretical model). R factor is used to value the goodness of the fitting.

The practical MEA device performance of the CeO_x@Pt/C as cathode catalyst was evaluated in a 5 cm^2 single-cell fuel cell fixture with a total PGM loading of 0.1 mg_{PGM}/cm^2 (cathode loading was controlled at 0.09 mg_{PGM}/cm^2 and anode loading was at 0.01 mg_{PGM}/cm^2, see Methods for detail). The performance is benchmarked against commercial Pt/C (comm-Pt/C) under identical fabrication and testing conditions. The testing protocols and performance metrics were selected with an emphasis on heavy-duty applications as recommended by the Million Mile Fuel Cell Truck consortium (M2FCT, see Methods for detail),[26] in which the power performance is evaluated at 0.7 V (for efficiency consideration), while the AST is extended to 90,000 cycles.

We first evaluated the catalyst MA, an indicator of catalyst activity and fuel cell performance at LCD, and its stability after the AST (Figure 3. 5, Figure 3. 6). These tests, conducted under H_2-O_2 at differential flow conditions (see Methods for detail), reflect the catalyst performance and stability without strong interference from mass transport limitations. Owing to the ultrafine size, the CeO_x@Pt/C demonstrated an excellent beginning-of-life (BOL) MA of 1.13 A/mg_{PGM}, considerably higher than the comm-Pt/C (0.34 A/mg_{PGM}) and surpassing DOE target (0.44 A/mg_{PGM}). Notably, after applying 90,000 aggressive square-wave AST cycles on these low-PGM-loading MEAs, the CeO_x@Pt/C retained 85% of its initial MA (EOL MA of 0.96 A/mg_{PGM}),

while the comm-Pt/C only retained 17% of its initial MA (0.06 A/mg$_{PGM}$), offering an impressive 16 times higher EOL MA compared to comm-Pt/C.

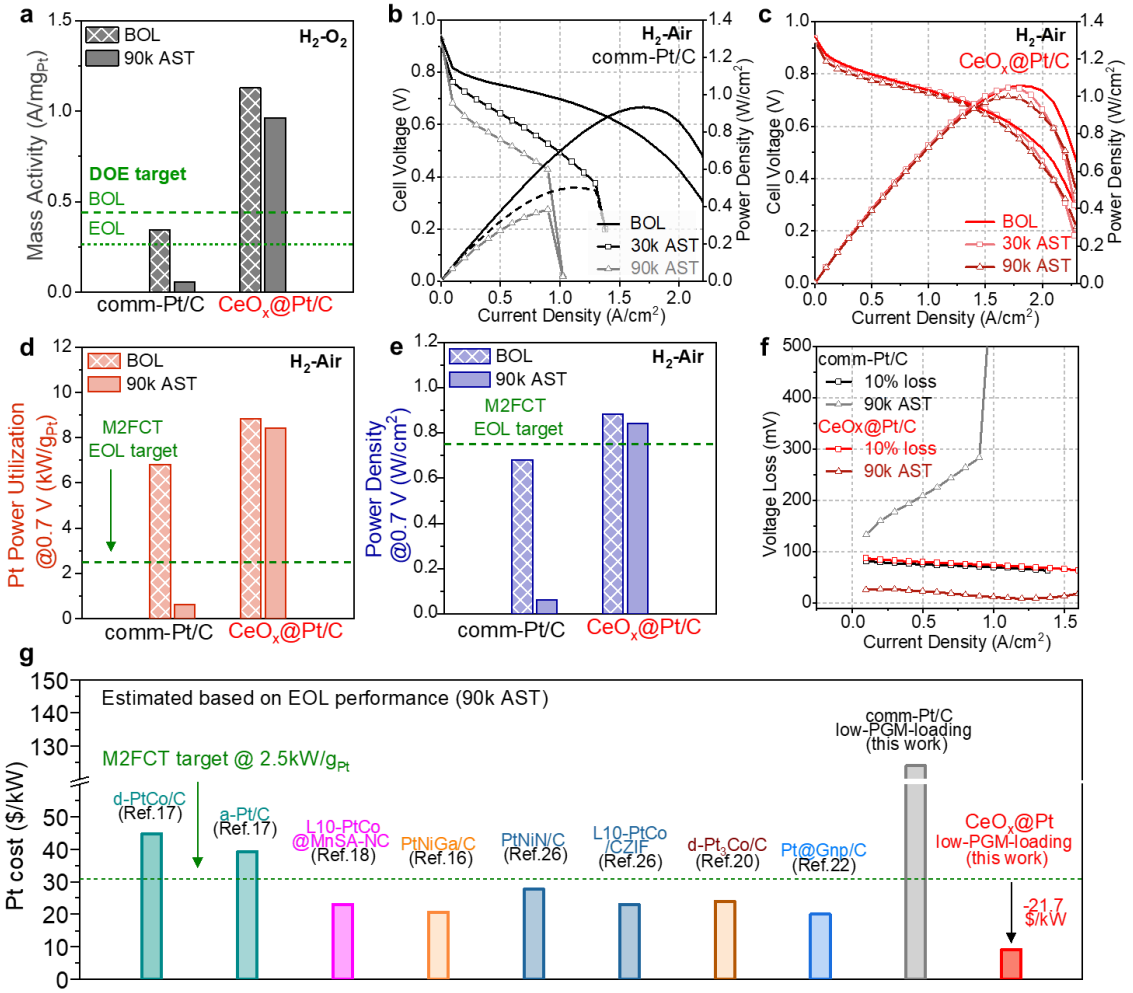

Figure 3. 5 MEA performance and stability of CeO_x@Pt/C and commercial Pt/C (comm-Pt/C). (a) Comparison of mass activity (MA) obtained in H_2/O_2 tests (80 °C, 100% RH, 150 kPa_{abs} with a differential flow condition of 835 (H_2)/2000 (O_2) sccm) at the beginning of life (BOL; before AST) and end of life (EOL; after 90,000 AST). Polarization plots (left y-axis) and power density plots (right y-axis) of (b) comm-Pt/C and (c) CeO_x@Pt/C obtained in H_2/air tests at BOL, after 30,000 and 90,000 cycles, highlighting extraordinary power performance and stability of the MEA with CeO_x@Pt/C. The H_2/Air tests were run at 94 °C, 250 kPa_{abs}, and 100% RH with a gas flow rate of 126 (H_2)/400 (air) sccm, which is equivalent to the stoichiometry of 1.5/2.0 at 2.4 A/cm^2 (endpoint of current density plot). Comparison of (d) Pt power utilization at 0.7 V and (e) power density obtained in H_2/air tests at BOL and EOL after 90,000 AST. DOE M2FCT targets are represented by green dash line. (f) Voltage loss after 90,000 AST at various current densities and the comparison to 10% voltage loss from BOL voltage. (g) The comparison of Pt cost estimated from the EOL Pt power utilization performance (kW/g_{Pt}) between the CeO_x@Pt/C catalyst and state-of-the art reference catalysts, assuming a Pt price of 50$/$g_{Pt}$ and an active-to-total area ratio of 0.65 as reported by M2FCT[7]: d-PtCo/C, a-Pt/C;[17] L10-PtCo@MnSA-NC;[18] PtNiGa/C;[16] PtNiN/C, L10-PtCo/CZIF;[26] d-Pt_3Co/C;[20] Pt@Gnp/C[22]. DOE M2FCT targets are represented by green dash line, and CeO_x@Pt/C offers a 70% (-21.7 $/kW) cost reduction.

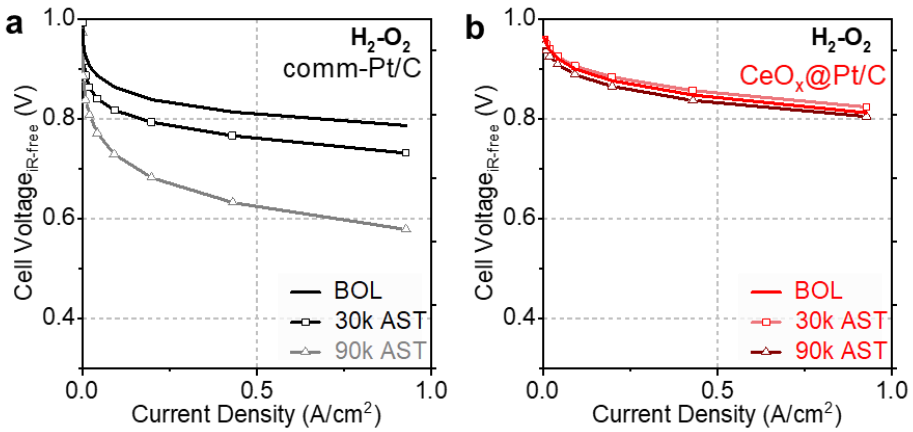

Figure 3. 6 H_2-O_2 polarization curve comparison of. (a) comm-Pt/C, and (b) CeO_x@Pt/C. Polarization plots were tested under H_2/O_2 at 80°C, 100 RH% and 150 kPa_{abs} in BOL after activation, after 30,000 AST cycles, and after 90,000 AST cycles. The cathode loading of all MEAs were 0.09 mg_{PGM}/cm^2 (total loading 0.10 mg_{PGM}/cm^2).

To evaluate the practical fuel cell performances in transportation applications, the MEAs were then tested under H_2-air at a low stoichiometry (1.5:2.0, see Methods for detail). This testing condition, in which mass transport plays an important role, evaluates not only the catalyst stability (in terms of composition and size), but also their indirect impacts on ionomer/membrane, e.g., the cation poisoning effect. From the obtained polarization curves (Figure 3. 5b,c), it is clear that CeO_x@Pt/C offers much better power performance compared to comm-Pt/C throughout the LCD and HCD regions. More importantly, it was found that comm-Pt/C suffered high mass transport loss as indicated by the drastically decreased HCD performance only after 30,000 AST cycles, e.g., peak power density decreased from 0.94 W/cm^2 to 0.51 W/cm^2 (Figure 3. 5b). In sharp contrast, the power performance of the MEA with CeO_x@Pt/C largely maintained throughout 90,000 AST cycles (peak power density slightly decreased from 1.06 W/cm^2 to 1.04 W/cm^2 and 1.00 W/cm^2 after 30,000 and 90,000 AST cycles, respectively (Figure 3. 5c).

For HDV-related MEAs, the DOE M2FCT has set a single performance target of 2.5 kW/g_{PGM} (0.75 W/cm^2) at 0.7 V after AST, which combines durability, power density, and cost. To this end, we showed that the CeO_x@Pt/C has far exceeded the M2FCT target with an EOL Pt

power utilization of 8.4 kW/g_{PGM} and a performance retention over 90% (Figure 3. 5d), while the comm-Pt/C only retained less than 10% of its initial performance (from 6.8 to 0.6 kW/g_{PGM}). In addition to the loading-normalized power, we further evaluate the absolute power density as it would directly impact the cell area and the stack cost. Notably, the CeO_x@Pt/C delivers a high EOL power density of 0.84 W/cm^2 (Figure 3. 5e), satisfying the M2FCT target (0.75 W/cm^2) and is over 13 times of the performance in comm-Pt/C (0.06 W/cm^2).

To further demonstrate the stability advantage of the developed catalyst, the voltage losses across a broad current density regions after 90,000 AST cycles are calculated (Figure 3. 5f). The voltage loss is an important indicator as it is closely related to fuel efficiency, which is the largest share in the total cost of ownership, and thus determines the lifetime of the fuel cell stack (<10% voltage loss at maximum power).[4] Impressively, the CeO_x@Pt/C MEA exhibits a relatively small voltage loss of less than 20 mV (~3%) throughout the current density region up to 1.6 A/cm^2, far below the 10% voltage loss. In contrast, the comm-Pt/C exhibited a much larger voltage loss exceeding 100 mV in all current density regions. Additionally, by defining the duration to reach 10% BOL voltage loss as the lifetime, we estimated a projected lifetime of over 45,000 hours for the CeO_x@Pt/C MEA (see Methods for detail, Figure 3. 7), satisfying the HDV lifetime target of 30,000 hours. In comparison, the lifetime for comm-Pt/C is only <1000 hours under identical test conditions.

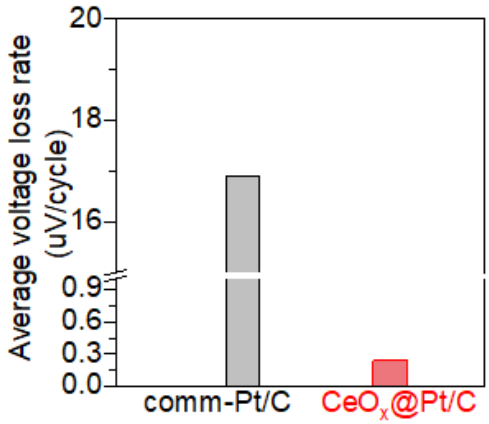

Figure 3. 7 Average voltage loss rate of the catalysts after AST cycles. The voltage loss rate is calculated at the current density of 1.5 A/cm^2. For comm-Pt/C, the voltage loss rate is estimated from the first 30,000 cycles as the maximum current density could not reach 1.5 A/cm^2 after 90,000 AST cycles.

To provide a quantitative picture on the impact of reducing PGM loading while still satisfying the stability requirements, we projected the Pt cost ($/kW) for the HDV fuel cells based on EOL performance and compared the result with the state-of-the-art catalysts (Figure 3. 5g, see Methods for detail).[7] It was found that the CeO_x@Pt/C catalyst lead to a Pt cost of only 9 $/kW, significantly lower than all state-of-the-art catalysts (20-45$/kW) and presented a 70% cost reduction from the M2FCT target of 30$/kW (estimated based on the 2.5 kW/g_{PGM} and the 0.3 mg_{PGM}/cm^2 targets). On the contrary, the low-PGM-loading MEA with comm-Pt/C was estimated to result in a high Pt cost of over 120 $/kW, owing to its poor stability and low EOL power performance.

These striking performance, stability, and Pt cost differences between comm-Pt/C and the developed CeO_x@Pt/C re-emphasize the grand challenge in meeting the heavy-duty-relevant stability requirements with low-PGM-loading MEA, and also clearly highlight that the CeO_x@Pt design effectively suppressed the degradation even under the most demanding low-PGM loading conditions.

Multi-scale microscopic characterizations and electrochemical tests were conducted to further understand the challenge in low-PGM-loading MEA under HDV conditions as well as the origin of the stability difference between CeO_x@Pt and comm-Pt/C (Figure 3. 8). First, we analyzed and compared the nanoparticle size distribution in these low-PGM-loading MEA after the AST (Figure 3. 8a-c). The size of comm-Pt/C increased dramatically from 3.6 ± 0.9 nm at BOL to 13.8 ± 8.4 nm after 90,000 AST cycles (Figure 3. 8a,c). Such a substantial increase and broadening of particle size is a clear indicator of Ostwald ripening and particle coalescence due to severe oxidative dissolution and redeposition during the harsh AST with low-PGM-loading MEA.[27] In contrast, the average size of the CeO_x@Pt/C only increased moderately from 1.5 ± 0.3 nm at BOL to 5.1 ± 1.1 nm at EOL (Figure 3. 8b,c), while still keeping a relatively narrow size distribution after 90,000 AST cycles. To evaluate the potential impacts of initial Pt particle size and the mere presence of CeO_x, we tested additional reference catalysts: a commercial Pt/C with an initial particle size around 2 nm (comm-Pt/C-2nm), and a physical mixture of comm-Pt/C-2nm with home-made CeO_x/C at the same Ce loading (Figure 3. 9, see Methods for detail). MEAs were fabricated following the identical recipe. While smaller size commercial Pt/C (comm-Pt/C-2nm) showed improved BOL performance, both commercial Pt/C catalysts exhibited comparably poor stability and EOL performance: around 90% power loss after 90k AST (Figure 3. 10, Table 3. 3). Meanwhile, the physical mixture of comm-Pt/C-2nm and CeO_x/C did not show a noticeable difference in stability (Figure 3. 10, Table 3. 3). These results further support the stabilizing role of embedded CeO_x with intimate CeO_x-Pt interaction.

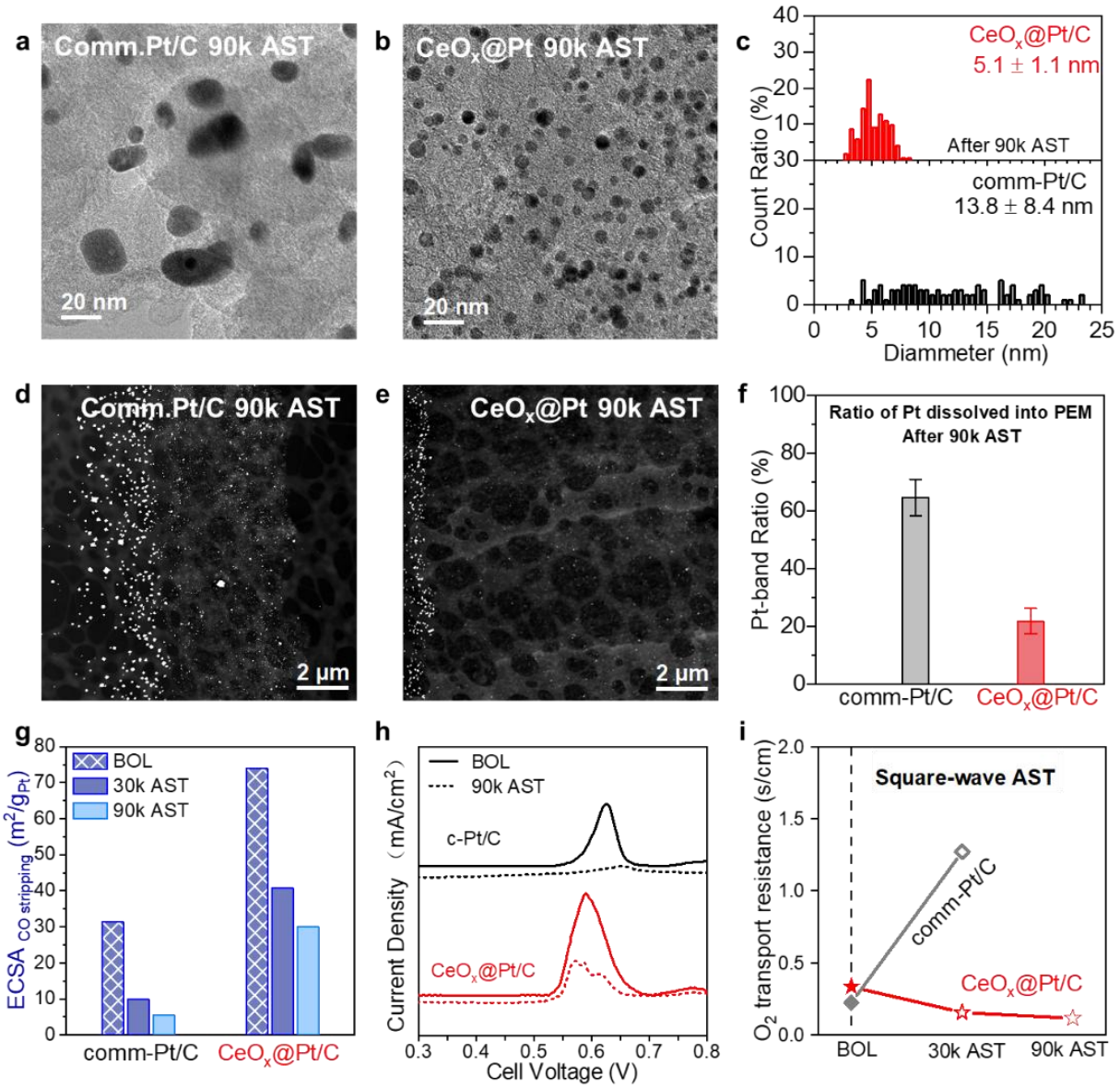

Figure 3. 8 Post-stability characterizations to understand the enhanced stability under HDV conditions. TEM images of (a) comm-Pt/C and (b) CeO_x@Pt/C after 90,000 AST cycles. (c) The corresponding size distribution and the count-based average diameter of CeO_x@Pt/C (red) and comm-Pt/C (grey). Dark field STEM images of the MEA cross section after 90,000 AST cycles of (d) comm-Pt/C and (e) CeO_x@Pt/C. (f) The ratio of Pt-band over the total Pt signal from the whole catalyst layer, reflecting the degree of Pt dissolution. Note that the CeO_x@Pt MEA has much less Pt dissolution as reflected by a much smaller fraction of Pt-band compared to comm-Pt/C. (g) The comparison of ECSA, obtained from CO stripping experiments at 80 °C in MEAs, and its degradation during AST between comm-Pt/C and CeO_x@Pt/C. (h) Comparison of CO oxidation peaks obtained at 80 °C in MEAs, showing the change of oxidation peak potential at BOL (solid lines) and EOL (dotted lines) of the comm-Pt/C and CeO_x@Pt/C catalysts. (i) The change of pressure-independent oxygen transport resistance of the comm-Pt/C and CeO_x@Pt/C catalysts at BOL and after AST.

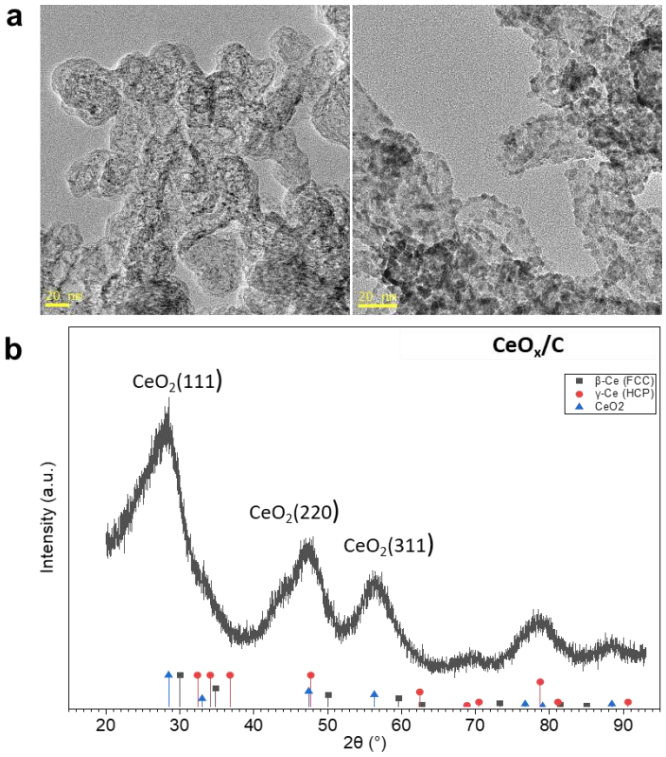

Figure 3. 9 (a) TEM images and (b) XRD pattern of home-made CeO_x/C.

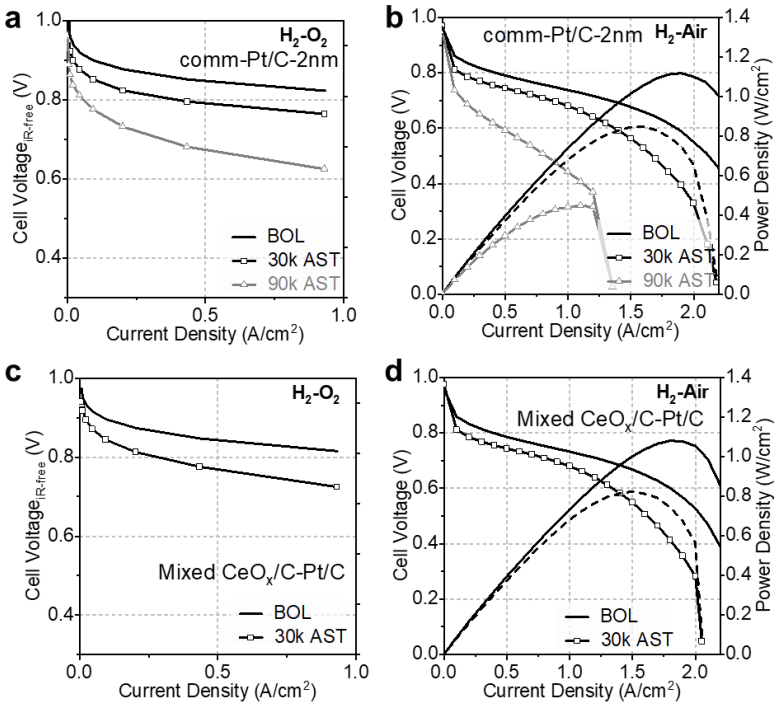

Figure 3. 10 (a) H_2-O_2 and (b) H_2-air polarization plots of comm-Pt/C-2nm at BOL, after 30,000 and 90,000 cycles. (c) H_2-O_2 and (d) H_2-air polarization plots of physically mixed CeO_x/C-Pt/C at BOL and after 30,000 cycles. Note that the physically mixed CeO_x does not show noticeable impact on the fuel cell stability.

Catalyst	Total Loading (mg_{Pt} cm^{-2})	Mass Activity (A/mg_{Pt})			Power density @ 0.7 V W/cm^2			90k Power loss%	Pt cost $/kW	AST condition
		BOL	30k EOL	90k EOL	BOL	30k EOL	90k EOL			
DOE M2FCT target	0.30	NA	NA	NA	NA	NA	0.75	10%	30.8	Squarewave
CeO_x@Pt/C (this work)	0.1	1.13	1.30	0.962	0.883	0.921	0.843	3.3%	9.1	Squarewave
comm-Pt/C (this work)	0.1	0.344	0.09	0.057	0.682	0.200	0.062	90.9%	124.1	Squarewave
comm-Pt/C-2nm (this work)	0.1	1.00	0.234	0.061	0.934	0.609	0.118	87.4%	68.7	Squarewave
Mixed CeO_x/C-Pt/C (this work)	0.1	0.948	0.226	NA	0.896	0.608	NA	NA	NA	Squarewave
CoO_x@Pt/C Ref.[21]	0.1	1.1	0.97	NA	0.965	0.91	NA	NA	NA	Squarewave
NiO_x@Pt/C Ref.[21]	0.1	0.89	0.71	NA	0.915	0.837	NA	NA	NA	Squarewave
FeO_x@Pt/C Ref.[21]	0.1	1.01	0.75	NA	0.928	0.842	NA	NA	NA	Squarewave
Pt@Gnp Ref.[22]	0.25	0.745	0.872	0.646	0.987	1.01	0.963	2.4%	20.0	Squarewave
a-Pt/C Ref.[17]	0.3	0.4	0.28	0.2	0.875	NA	0.588	32.8	39.2	Squarewave
d-PtCo Ref.[17]	0.3	0.8	0.36	0.16	0.875	NA	0.516	41.0	44.7	Squarewave
PtNiGa/C Ref.[16]	0.25	0.6	NA	0.4	1.17	NA	0.931	20.4	20.7	Squarewave
L12-Pt_3Co@MnSA-NC Ref.[18]	0.3	0.49	NA	0.31	1.22	NA	1.001	18.0	23.1	Squarewave
d-PtCo/HSC Ref.[20]	0.25	0.6	NA	NA	NA	NA	0.800	NA	24.0	Squarewave
PtNiN/KB Ref.[26]	0.3	NA	NA	NA	NA	NA	0.833	NA	27.7	Squarewave

Table 3. 3 Summary of fuel cell performances and Pt cost of the representative state-of-the-art catalysts and CeO_x@Pt/C catalyst in this work.

As Pt dissolution is one of the key catalyst degradation pathways under fuel cell operation, we studied and quantified the Pt dissolution properties by characterizing the Pt-band (Figure 3. 8d-f), which is formed via Pt dissolution, diffusion-into-membrane, and redeposition at the membrane-catalyst interface.[28] The STEM imaging and EDS analysis on the MEA cross-section

after 90,000 AST cycles revealed that the comm-Pt/C MEA lost 64.6 ± 6.4% of Pt mass into the Pt-band (Figure 3. 8d,f), whereas the CeO_x@Pt/C MEA showed only 21.7 ± 4.4% Pt mass loss (Figure 3. 8e,f). We conducted EELS on the post-AST CeO_x@Pt particles and found the the CeO_x clusters remained inside the Pt particles at similar density (Figure 3. 11). These results explain the dramatic EOL performance difference and clearly support that the CeO_x@Pt design effectively suppressed Pt dissolution under the harsh HDV condition with low-PGM-loading MEA.

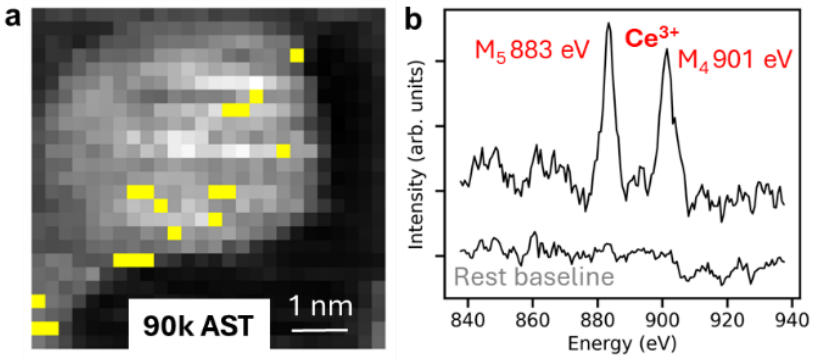

c

	Ce atoms	radius (nm)	volume (nm^3)	Density ($atom/nm^3$)
CeOx@Pt/C BOL	3	1.5	14.1	0.21
After 90,000 AST cycles	10	2.5	65.4	0.15

Figure 3. 11 (a) STEM-EELS elemental maps showing the sparsely dispersed Ce within the Pt nanoparticle. (b) The corresponding EELS spectrum from the Ce signal. (c) Analysis of Ce density in the nanoparticle.

The available Pt surface area was further evaluated by electrochemical CO stripping (Figure 3. 8g,h), it was found that, after 90,000 AST cycles, the CeO_x@Pt/C catalyst exhibited a considerably higher EOL ECSA (30.0 m^2/g_{PGM}) in MEAs than that of comm-Pt/C (5.5 m^2/g_{PGM}) catalyst (Figure 3. 8g). These electrochemical test results are consistent with the microscopic studies and the observed EOL performance trend. In addition, we also probe the change in the chemisorption behavior of catalyst through the CO stripping experiments, as the lower CO

oxidation peak indicates a weaker CO binding strength, which also found to be correlated to weaker oxygen adsorption energy,[29] favoring ORR kinetics. Interestingly, the CO oxidation peak in comm-Pt/C showed a notable shift to higher binding energy, while it was not observed in the CeO_x@Pt/C (Figure 3. 8h, Figure 3. 12). This result indicates that the favorable weak oxygen adsorption characteristics in CeO_x@Pt/C is maintained after AST test.

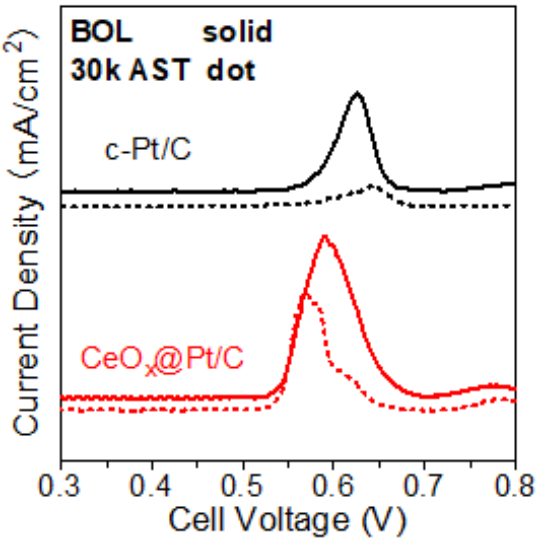

Figure 3. 12 CO stripping tests of catalysts at BOL and after 30k AST cycles. Tested at 80℃, 100 RH%.

The direct impact of the stability in available Pt surface area is further evidenced by the studies on pressure-independent oxygen transport resistance (Figure 3. 8i), which has been found to be inversely proportional to the available Pt surface area. Notably, CeO_x@Pt/C maintained a low oxygen transport resistance throughout the AST test (Figure 3. 8i, red), ensuring good mass transport and HCD performance. On the contrary, comm-Pt/C experienced nearly 5 times increase in the oxygen transport resistance after just 30,000 AST cycles (Figure 3. 8i, grey), consistent with the observations of high Pt mass loss into the Pt-band and considerable size growth within the catalyst layer.

3.4 Conclusion

Together, by embedding CeO_x clusters and utilizing the strong CeO_x-Pt interaction in the ultrafine Pt nanoparticles, we demonstrate an effective catalyst design strategy against size growth and Pt dissolution under a challenging HDV condition (90,000 AST cycles) with low-PGM loading (0.1 mg_{PGM}/cm^2). The low-PGM-loading and high EOL performance of the CeO_x@Pt/C MEA reduce the Pt-cost by 70% from the M2FCT target, representing a promising catalyst candidate for HDV applications.

3.5 References

1. Debe, M. K. Electrocatalyst approaches and challenges for automotive fuel cells. *Nature* **486**, 43–51 (2012).

2. Cullen, D. A. *et al.* New roads and challenges for fuel cells in heavy-duty transportation. *Nat. Energy* **6**, 462–474 (2021).

3. Kodama, K., Nagai, T., Kuwaki, A., Jinnouchi, R. & Morimoto, Y. Challenges in applying highly active Pt-based nanostructured catalysts for oxygen reduction reactions to fuel cell vehicles. *Nat. Nanotechnol.* **16**, 140–147 (2021).

4. Ramaswamy, N., Kongkanand, A., Wortman, J. & Gu, W. Review—Meeting Fuel Cell Catalyst Requirements for Heavy-Duty Vehicle Applications. *J. Electrochem. Soc.* **172**, 024501 (2025).

5. James, B. D., Huya-Kouadio, J. M., Houchins, C. & Desantis, D. A. *Mass Production Cost Estimation of Direct H2 PEM Fuel Cell Systems for Transportation Applications: 2018 Update*. (2018).

6. Zhang, F. *et al.* Developing long-durability proton-exchange membrane fuel cells. *Joule* **9**, (2025).

7. James, B. D. & Huya-Kouadio, J. *Fuel Cell Cost and Performance Analysis*. (2024).

8. Lohse-Busch, H. *et al.* Automotive fuel cell stack and system efficiency and fuel consumption based on vehicle testing on a chassis dynamometer at minus 18 °C to positive 35 °C temperatures. *Int. J. Hydrogen Energy* **45**, 861–872 (2020).

9. Lopes, P. P. *et al.* Eliminating dissolution of platinum-based electrocatalysts at the atomic scale. *Nat. Mater.* **19**, 1207–1214 (2020).

10. Li, J. *et al.* Hard-Magnet L10-CoPt Nanoparticles Advance Fuel Cell Catalysis. *Joule* **3**, 124–135 (2019).

11. Wang, X. X. *et al.* Ordered Pt3Co Intermetallic Nanoparticles Derived from Metal-Organic Frameworks for Oxygen Reduction. *Nano Lett.* **18**, 4163–4171 (2018).

12. Yang, C.-L. *et al.* Sulfur-anchoring synthesis of platinum intermetallic nanoparticle catalysts for fuel cells. *Science.* **374**, 459–464 (2021).

13. Cai, Y., Kongkanand, A., Gu, W. & Moylan, T. E. Effects of Cobalt Cation on Low Pt-loaded PEM Fuel Cell Performance. *ECS Trans.* **69**, 1047–1061 (2015).

14. Kongkanand, A., Yarlagadda, V., Garrick, T. R., Moylan, T. E. & Gu, W. (Plenary) Electrochemical Diagnostics and Modeling in Developing the PEMFC Cathode. *ECS Trans.* **75**, 25–34 (2016).

15. Zhao, Z. *et al.* Graphene-nanopocket-encaged PtCo nanocatalysts for highly durable fuel cell operation under demanding ultralow-Pt-loading conditions. *Nat. Nanotechnol.* **17**, 968–975 (2022).

16. Liang, J. *et al.* Metal bond strength regulation enables large-scale synthesis of intermetallic nanocrystals for practical fuel cells. *Nat. Mater.* **23**, 1259–1267 (2024).

17. Wang, X., Hu, L., Neyerlin, K. C. & Ahluwalia, R. K. Baselining Activity and Stability of ORR Catalysts and Electrodes for Proton Exchange Membrane Fuel Cells for Heavy-Duty Applications. *J. Electrochem. Soc.* **170**, 024503 (2023).

18. Zeng, Y. *et al.* Regulating Catalytic Properties and Thermal Stability of Pt and PtCo Intermetallic Fuel-Cell Catalysts via Strong Coupling Effects between Single-Metal Site-Rich Carbon and Pt. *J. Am. Chem. Soc.* **145**, 17643–17655 (2023).

19. Borup, R. & Weber, A. *M2FCT: Million Mile Fuel Cell Truck Consortium*. https://www.hydrogen.energy.gov/docs/hydrogenprogramlibraries/pdfs/review21/fc339_weber_2021_o-pdf.pdf (2021).

20. Ramaswamy, N. *Surface Protected High Activity Pt Alloy Catalysts for Durable Heavy Duty Fuel Cells*. (2024).

21. Peng, B. *et al.* Embedded oxide clusters stabilize sub-2 nm Pt nanoparticles for highly durable fuel cells. *Nat. Catal.* **7**, 818–828 (2024).

22. Liu, Z. *et al.* Pt catalyst protected by graphene nanopockets enables lifetimes of over 200,000 h for heavy-duty fuel cell applications. *Nat. Nanotechnol.* **20**, 807–814 (2025).

23. Leybo, D. *et al.* Metal-support interactions in metal oxide-supported atomic, cluster, and nanoparticle catalysis. *Chem. Soc. Rev.* **53**, 10450–10490 (2024).

24. Zhang, J. *et al.* Structural characteristics of cerium oxide nanocrystals prepared by the microemulsion method. *Chem. Mater.* **13**, 4192–4197 (2001).

25. Masuda, T. *et al.* Role of cerium oxide in the enhancement of activity for the oxygen reduction reaction at Pt-CeO x nanocomposite electrocatalyst - An in situ electrochemical X-ray absorption fine structure study. *J. Phys. Chem. C* **116**, 10098–10102 (2012).

26. Borup, R. & Weber, A. *M2FCT: Million Mile Fuel Cell Truck Consortium*. (2024).

27. Borup, R. L. *et al.* Recent developments in catalyst-related PEM fuel cell durability. *Curr. Opin. Electrochem.* **21**, 192–200 (2020).

28. Padgett, E. *et al.* Mitigation of PEM Fuel Cell Catalyst Degradation with Porous Carbon Supports. *J. Electrochem. Soc.* **166**, F198–F207 (2019).

29. Nilsson, A. *et al.* The electronic structure effect in heterogeneous catalysis. *Catal. Letters* **100**, 111–114 (2005).

Chapter 4. Synthesis of PtCo Nanotwinned Catalysts via Laser Ablation

4.1 Introduction

The nanostructure of materials plays a significant role in determining mechanical,[1,2] electronic,[3] biological,[4] and catalytic properties across various technological applications.[5-10] Among these, metastable materials, which exist in kinetically trapped, non-equilibrium states, exhibit unique phases, defect structures, and enhanced functionalities that are inaccessible in thermodynamically stable counterparts.[11,12] A particularly promising class of metastable materials is nanotwinned structures.[13,14] These structures exhibit superior mechanical strength,[15,16] exceptional thermal stability,[17,18] and enhanced catalytic properties,[19-21] making them attractive for a wide range of applications.[13] However, despite their promising properties, the controlled synthesis of nanotwinned structures is notoriously difficult due to the intricate balance between thermodynamic stability and kinetic trapping during twin formation.[13,22] Conventional synthesis techniques, such as crystallization control,[23,24] mechanical deformation,[25,26] surface diffusion,[27-29] and thermal treatments[30,31] can successfully introduce nanotwinning in low-stacking-fault energy-metals like gold (Au)[27,29,32] and copper (Cu).[15,19,28,33] However, extending these approaches to high-stacking-fault-energy metals including platinum (Pt), iridium (Ir), and nickel (Ni), aluminum (Al) alloys, remains particularly challenging and is unlikely to succeed.[34-36] The inability to effectively engineer stable twin boundaries in these metals has largely limited their potential in practical applications. Given the importance of Pt-group metals as catalysts in hydrogen oxidation reactions (HOR) and oxygen reduction reactions (ORR) for proton-exchange membrane fuel cells (PEMFCs),[37-39] as well as hydrogen evolution reactions (HER) and oxygen evolution reactions

(OER) for proton-exchange membrane water electrolyzers,[40-42] there is a pressing need for a facile synthetic method that can introduce nanotwinned structures into these materials.

Determined by the laser intensity profile,[43] the laser ablation (LA) technique can achieve extremely high cooling rates reaching up to 10^8 K s^{-1},[44,45] which enables precise microstructural and nanostructural engineering through rapid melting, solidification, and phase transformation. This makes laser ablation an ideal tool for creating diverse metastable nanostructures with high defect densities,[46] columnar grains,[47,48] and nanotwinned domains,[49,50] which are typically inaccessible through conventional manufacturing methods. Under these extreme thermal gradients, materials experience rapid quenching, enabling the stabilization of non-equilibrium phases and unique defect structures. Beyond structural control, the rapid heating and cooling enabled by laser ablation allow for fast synthesis, presenting potential for high-throughput material production.

In this study, we report the controlled synthesis of nanotwinned platinum-cobalt (PtCo) catalysts ($Pt_{78}Co_{22}$, 24.0 wt% of Pt) with a nanotwinning yield of 61% using a laser ablation-based approach (Figure 4. 1). By systematically exploring key laser parameters, such as exposure time and laser power, we successfully introduced twin boundaries within the nanoparticles. The resulting nanostructures were characterized using X-ray diffraction (XRD) and transmission electron microscopy (TEM). The elemental composition and element distribution within the nanoparticle were analyzed using energy dispersive X-ray spectroscopy (EDS). Optimal conditions for forming nanotwinned PtCo alloys were identified. Our results show that both particle agglomeration under high-energy beam and elemental effect play key roles in nanotwin formation. Importantly, the nanotwinned PtCo catalysts demonstrated exceptional activity and

durability in membrane electrode assembly (MEA) tests for their practical potential in PEMFC applications.

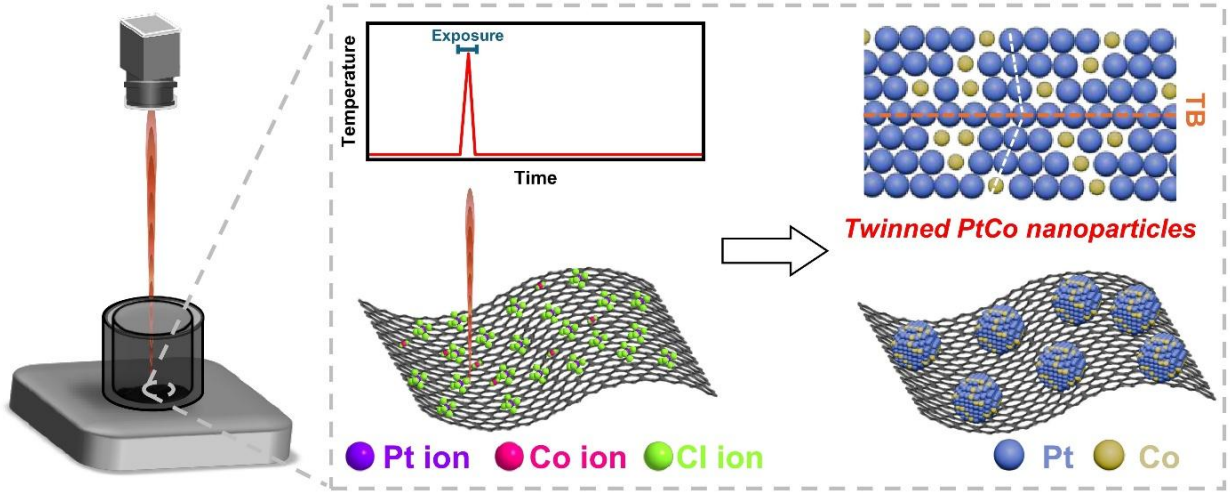

Figure 4. 1 Schematic illustration of the synthesis process for nanotwinned PtCo electrocatalysts via laser ablation. A pulsed laser irradiates metal precursors contained in a graphite crucible, generating rapid localized heating followed by quenching. This process facilitates the formation of PtCo nanoparticles with a high density of twin boundaries. The resulting nanotwinned structures are designed to enhance both catalytic activity and structural durability.

4.2 Methods

Materials and Chemicals

All chemicals were purchased from Sigma-Aldrich unless otherwise specified. Cobalt(II) chloride hexahydrate ($CoCl_2 \cdot 6H_2O$) was purchased from Thermo Fisher Scientific. Commercial Pt/C catalysts (10 and 40 wt% Pt) were obtained from Alfa Aesar. Commercial 20 wt% Pt/C was purchased from Fuel Cell Store. Commercial 20 wt% and 40 wt% PtCo/C were purchased from Premetek. All reagents were used as received without further purification. High purity graphite crucibles (5 mL, 25 mm OD, 19 mm ID) were purchased from MSE Supplies. Optical fused quartz discs (25.4 mm OD, 1.59 mm thick) were purchased from AdValue Tech. Ketjen-EC300J carbon black (KB) was sourced from Lion Specialty Chemicals Co., Ltd. Deionized water (18 MΩ·cm) was supplied by a Milli-Q Advantage A10 ultrapure purification system.

Catalyst Preparation

Synthesis of Nanotwinned PtCo Nanoparticles: To prepare the catalyst, 500 mg of Ketjen-EC300J carbon black was weighed in a 500 mL beaker. Then, 376 mL of deionized water was added, followed by 1 hour of ultrasonication to disperse the carbon black. Subsequently, 3.75 mL of chloroplatinic acid solution (8 wt% in H_2O) and 1.53 mL of 0.205 mmol/mL $CoCl_2 \cdot 6H_2O$ were added to the dispersion, followed by an additional hour of sonication. After sonication, the precursor dispersion was stirred overnight at room temperature. The resulting dispersion was evenly divided into 30 mL vials, frozen in liquid nitrogen (N_2) until solidified, and then freeze-dried for 72 hours to remove ice crystals. The dried powder was collected immediately prior to laser ablation processing to prevent hydrolysis of precursors.

In a typical synthesis of nanotwinned PtCo nanoparticles via laser ablation, 40 mg of dried powder was transferred to a high-purity graphite crucible. The powder was then manually pressed into a thin film by a steel bar with a flat graphite head that fit the size of the opening of the graphite crucible. A fused quartz disc was placed on top to cover the opening and secured with tape. The crucibles containing catalyst precursors were then placed to the Renishaw AM400 stage. Laser ablation was carried out in a N_2 atmosphere using pre-programmed parameters, including laser power, exposure time, defocus, hatch spacing, and point distance, to control the synthesis process. To prepare the catalyst for further investigation and MEA testing, the as-synthesized material (as-synthesized PtCo-LA) was washed in N_2-saturated 0.05 M H_2SO_4 at 80 °C for 12 hours in a sealed vial. The catalyst was then washed with deionized water until the pH was approximately neutral (~7) and collected via centrifugation. The washed catalyst was dried under vacuum in a desiccator for 24 hours before being transferred to a quartz crucible for annealing. Annealing was conducted

in an H_2/Ar atmosphere at 180 °C for 1.5 hours inside a quartz tube. The final product (PtCo-LA) was collected after cooling and used directly for subsequent characterization and testing.

Structure and Composition Characterization

Low-magnification TEM images were acquired using an FEI T12 TEM operated at 120 kV. High-resolution TEM (HRTEM), EDS, and high-angle annular dark-field scanning transmission electron microscopy (HAADF-STEM) images were obtained using a JEM-ARM300F STEM operated at 300 kV. TEM samples were prepared by depositing an ethanol dispersion of catalysts onto carbon-coated aluminum TEM grids. The elemental composition of the catalysts was determined by inductively coupled plasma atomic emission spectroscopy (ICP-AES). X-ray photoelectron spectroscopy (XPS) was performed using a Kratos AXIS Ultra DLD spectrometer. Pt loading in the catalysts was determined prior to electrochemical ink preparation and Pt loading on the MEA was assessed using ICP-AES after mass activity (MA) and power density measurements. Specifically for the assessment of MEA loading, two sprayed catalyst samples (1 cm^2 each) were cut from the PTFE gaskets, soaked in aqua regia for 24 hours, and used to prepare ICP solutions for metal content analysis.

MEA Preparation and Fuel Cell Testing

The single-cell performance of the catalysts as cathodes was evaluated at an 850e Fuel Cell Test System (Scribner, USA). The MEAs with an active area of 5.0 cm^2 were fabricated using a catalyst-spray membrane method. Catalysts were incorporated into MEAs by direct ultrasonic spraying of a water/2-propanol based ink onto a reinforced perfluorosulfonic acid membrane (12 μm thick) at the desired loading. The anode Pt loading was set to be 0.01 mg_{Pt}/cm^2. The cathode Pt loading ranged from 0.085 to 0.09 mg_{Pt}/cm^2. The MA was measured via recording the current at 0.9 V (iR-free) under H_2/O_2 at 150 kPa absolute pressure (abs) (80 °C, 100% relative humidity

(RH), 835/2000 cm^3/min) with correction for measured H_2 crossover. The H_2-air performance tests were conducted under 250 kPa_{abs} H_2/Air (94 °C, 100% RH, 126/400 cm^3/min). The accelerated stress test (AST) was conducted for 30,000 cycles using a square-wave potential protocol, with each cycle consisting of a 3 s hold at 0.6 V followed by a 3 s hold at 0.95 V (150 kPa_{abs}, 80 °C, 100% RH, H_2/N_2 = 100/100 cm^3/min). Rated power voltage = (77.6/ (22.1 + T (°C))) V, based on the target of $Q/\Delta Ti$ = 1.45 kW/°C (rated voltage = 0.67 V for 94 °C).

4.3 Results and Discussion

Compared with conventional wet chemical methods used in laboratories for synthesizing Pt-based electrocatalysts, laser ablation offers rapid processing for high-throughput studies and demonstrates high energy efficiency for scalable production (Table 4. 1). In the laser ablation synthesis, since the energy input into the system is primarily determined by exposure time and laser power, we fixed other tunable parameters, such as hatch spacing and point distance. To achieve a more uniform laser beam, the laser defocus was maximized to 4 mm, thereby increasing the laser scan area on the precursor films.

	Wet Chemical Methods [51,52]	Laser Ablation
Precursor Weight per Batch	13 g	3.6 g
Total Synthesis Time	580 mins [52]	18 mins
Total Energy Consumption	69.6 kWh	0.082 kWh
Material Yield	90% [53]	90%
Normalized Energy Consumption (per Unit Mass of Pt)	34.6 kWh/g_{Pt}	0.12 kWh/g_{Pt}
Normalized Synthesis Time (per Unit Mass of Pt)	4.8 hrs/g_{Pt}	0.5 hrs/g_{Pt}

Table 4. 1 Comparative analysis of Pt-based electrocatalyst synthesis: Wet Chemical Methods vs. Laser Ablation.

Twelve precursor samples were used to investigate the effects of varying exposure time and laser power on synthesis conditions (Figure 4. 2). For PtCo samples (PtCo-LA1 to PtCo-LA5) synthesized at either low laser power or short exposure times, we observed nanoparticles formation on carbon black (Figure 4. 3a-e); however, their XRD patterns showed residual precursor peaks and asymmetric diffraction peaks of metallic nanoparticles (Fig. 4. 2b, Table 4. 2), indicating incomplete reduction of Pt and Co precursors and insufficient alloying. This resulted in pronounced phase segregation and compositional nonuniformity in the nanoparticles (Figure 4. 2b). The average diameter of PtCo-LA3 nanoparticle was only 2.7 ± 0.6 nm based on TEM (Figure 4. 3c). The small particle size and low particle density on carbon black indicated a limited reduction driving force. To quantify the energy input into the system, we calculated the areal energy density based on the beam size, laser power, and exposure time (Fig. 4. 2a, Table 4. 3). When the areal energy density exceeded 3.5 J mm^{-2} (e.g., PtCo-LA6), the nanoparticle density on carbon black

was notably higher compared to those synthesized at low areal energy densities (Figure 4. 2b, Figure 4. 3f-h), indicating a higher reaction yield. Notably, the XRD patterns of PtCo-LA6, PtCo-LA7, and PtCo-LA8 showed no obvious peak asymmetry, suggesting reduced phase segregation (Figure 4. 2b). The (111) diffraction peak shifted from 39.52° to 40.27°, consistent with the (111) facet of $Pt_{85}Co_{15}$, based on the Vegard's law (Table 4. 2). TEM image showed that the average diameter of the nanoparticles is 6.4 ± 2.1 nm (e.g., PtCo-LA8) (Figure 4. 3h), in good agreement with the Scherrer equation results (6.1 nm, Table 4. 2). Further increasing the areal energy density beyond 4.9 J mm^{-2} (e.g., PtCo-LA9 to PtCo-LA12) led to the particle aggregation and the formation of large particles (Figure 4. 2b, Figure 4. 3i-l). The average particle size significantly increased to over 10 nm with larger variation in size distribution (Figure 4. 3i-l). Correspondingly, the XRD peaks shifted to lower angles, closely matching the pattern of pure Pt (Figure 4. 2b, Table 4. 2). This peak shift can be attributed to the dealloying of Co under the high-energy laser exposure, which likely caused localized overheating. These combined XRD and TEM results emphasized the importance of tuning laser power and exposure time for an optimal areal energy density for the uniform synthesis of PtCo alloy particles.

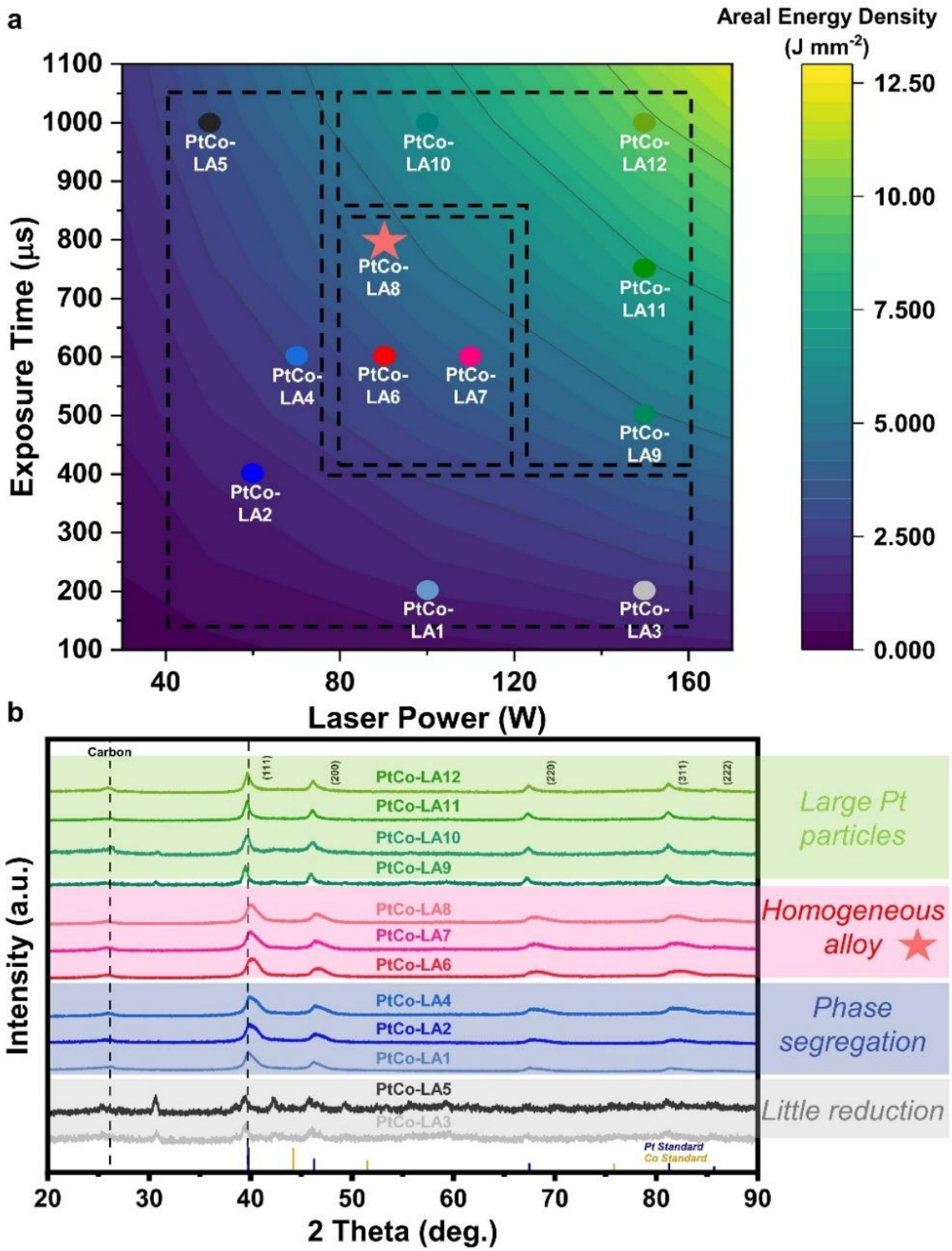

Figure 4. 2 Laser parameters and corresponding XRD characterization results for the as-synthesized PtCo-LA1 to PtCo-LA12 samples. (a) Map of areal energy density as a function of laser power and exposure time, which shows the tunable laser conditions used to generate different PtCo nanoparticles as catalysts. (b) XRD patterns of the resulting samples, revealing phase evolution and crystallinity changes induced by varying laser processing conditions.

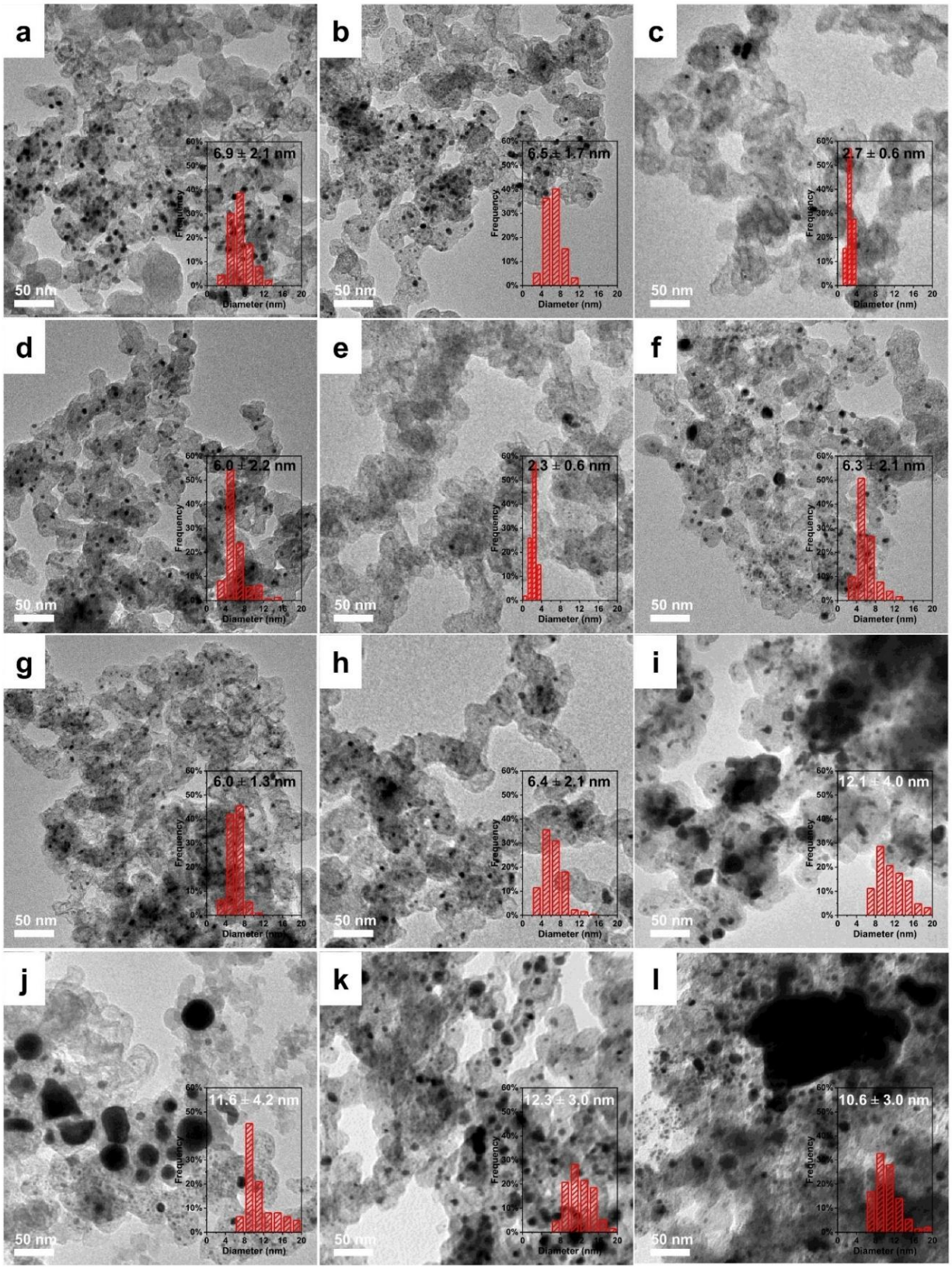

Figure 4. 3 TEM images and their corresponding particle size distribution charts of the as-synthesized (a-l) PtCo-LA1 to PtCo-LA12.

Sample Name	FWHM	Size (nm)	Pt (111)	Composition
PtCo-LA1	1.3656	6.19	39.97°	$Pt_{92}Co_8$
PtCo-LA2	1.4612	5.788	40.14°	$Pt_{88}Co_{12}$
PtCo-LA3	0.5993	14.086	39.52°	$Pt_{100}Co_0$
PtCo-LA4	1.4979	5.648	40.19°	$Pt_{87}Co_{13}$
PtCo-LA5	0.7968	10.590	39.40°	$Pt_{100}Co_0$
PtCo-LA6	1.4034	6.030	40.33°	$Pt_{84}Co_{16}$
PtCo-LA7	1.4679	5.764	40.27°	$Pt_{85}Co_{15}$
PtCo-LA8	1.3922	6.078	40.27°	$Pt_{85}Co_{15}$
PtCo-LA9	0.5183	16.283	39.45°	$Pt_{100}Co_0$
PtCo-LA10	0.7343	11.498	39.61°	$Pt_{100}Co_0$
PtCo-LA11	0.6612	12.770	39.63°	$Pt_{100}Co_0$
PtCo-LA12	0.8334	10.133	39.74°	$Pt_{98}Co_2$

Table 4. 2 Full width at half maximum (FWHM) and the corresponding nanoparticle sizes calculated by Scherrer's equation, and compositional analysis from Vegard's equation according to the position of the Pt (111) peak for as-synthesized PtCo-LA samples. (The standard Pt (111) peak appears at 39.76°; therefore, any peak at a lower angle corresponds to a Pt_{100} composition.)

Sample Name	Areal Energy Density (J mm^{-2})	Sample Name	Areal Energy Density (J mm^{-2})
PtCo-LA1	1.30	PtCo-LA7	4.29
PtCo-LA2	1.56	PtCo-LA8	4.68
PtCo-LA3	2.44	PtCo-LA9	4.87
PtCo-LA4	2.73	PtCo-LA10	6.50
PtCo-LA5	3.25	PtCo-LA11	7.31
PtCo-LA6	3.51	PtCo-LA12	9.74

Table 4. 3 Areal energy densities of as-synthesized PtCo-LA samples produced via laser ablation.

We further used HAADF-STEM to investigate the atomic structure of the PtCo alloys. Among all samples, PtCo-LA8 showed the highest twinning yield of 61% and was selected for detailed analysis. HAADF-STEM images revealed characteristic nanotwinning structures with well-defined twinning boundaries within the nanoparticles (Figure 4. 4b-d). Fast Fourier Transform (FFT) analysis indicated an averaged (111) lattice spacing of 0.221 to 0.223 nm, consistent with the expected (111) spacing for $Pt_{81\pm5}Co_{19\pm5}$. EDS elemental mapping results showed a uniform distribution of Pt and Co throughout the nanotwinning structures of PtCo-LA8, suggesting a well-mixed alloy phase without phase segregation (Figure 4. 4e-g). The composition of PtCo-LA8 was determined to be $Pt_{78\pm1}Co_{22\pm1}$ by EDS spectroscopy (Figure 4. 5a), which was consistent with ICP-AES measurements ($Pt_{78\pm0.3}Co_{22\pm0.3}$, Table 4. 4). The compositions obtained from EDS and ICP-AES fall within the range derived from lattice spacing. The HAADF-STEM/FFT method provides an indirect estimate based on structural parameters, which can be affected by local strain from twinning and imaging conditions. To evaluate the chemical stability under acid conditions, we compared the composition before and after acid washing. Notably for PtCo-LA8, only 13% Co leaching was observed after acid washing, indicating the exceptional chemical stability of the nanotwinned PtCo structure. In contrast, commercial PtCo/C showed a 34% Co loss (Table 4. 4). Even after acid washing, the size and composition of PtCo-LA8 remained unchanged according to the TEM and XRD results (Figure 4. 6).

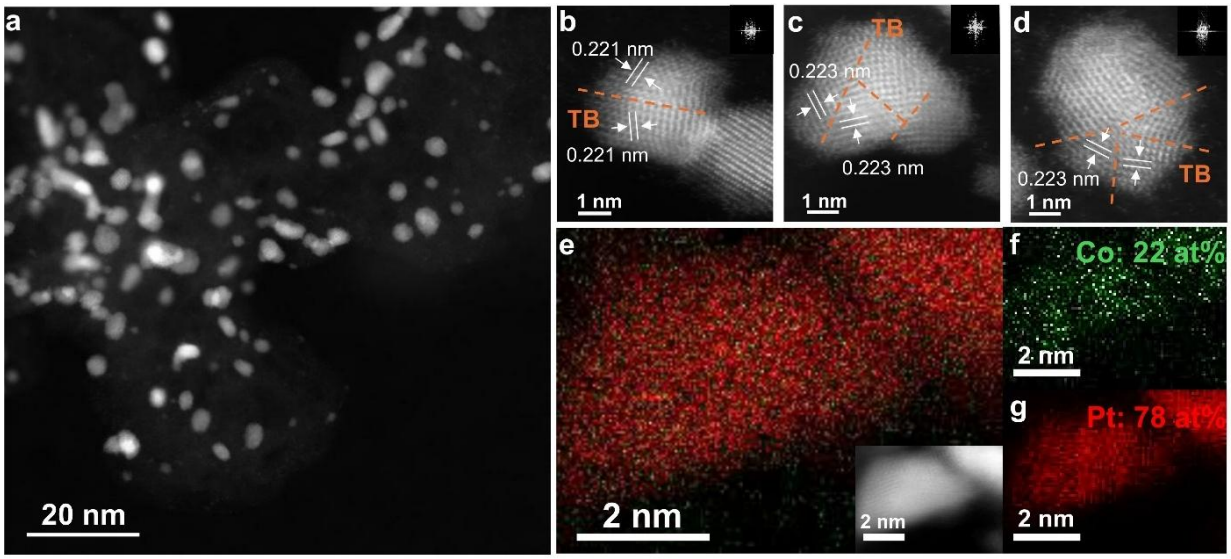

Figure 4. 4 Structural and compositional characterization of the PtCo-LA8 electrocatalyst. (a) HAADF-STEM image revealing the overall morphology and dispersion of PtCo-LA8 nanoparticles. (b-d) Representative high-resolution STEM images showing well-defined twin boundaries within individual nanoparticles. (e-g) EDS elemental maps of Pt, Co, and their overlay, confirming a uniform elemental distribution throughout the nanoparticles. The corresponding atomic percentages represent the alloy composition.

Sample	Weight % (Pt, Co, C)		Relative Atomic Ratio (%)	
	Pt	Co	Pt	Co
As-synthesized PtCo-LA8	24.6±0.2	2.4±0.1	75.3±0.02	24.7±0.02
Acid-washed PtCo-LA8	24.0±0.4	2.0±0.3	78.5±0.3	21.5±0.3
c-PtCo/C	36.1±0.2	3.5±0.1	75.9±0.02	24.1±0.02
Acid-washed c-PtCo/C	35.1±0.4	2.0±0.3	84.2±0.3	15.8±0.3

Table 4. 4 Comparisons of compositions measured by ICP-AES for PtCo-LA8 and 40% c-PtCo/C before and after acid washing.

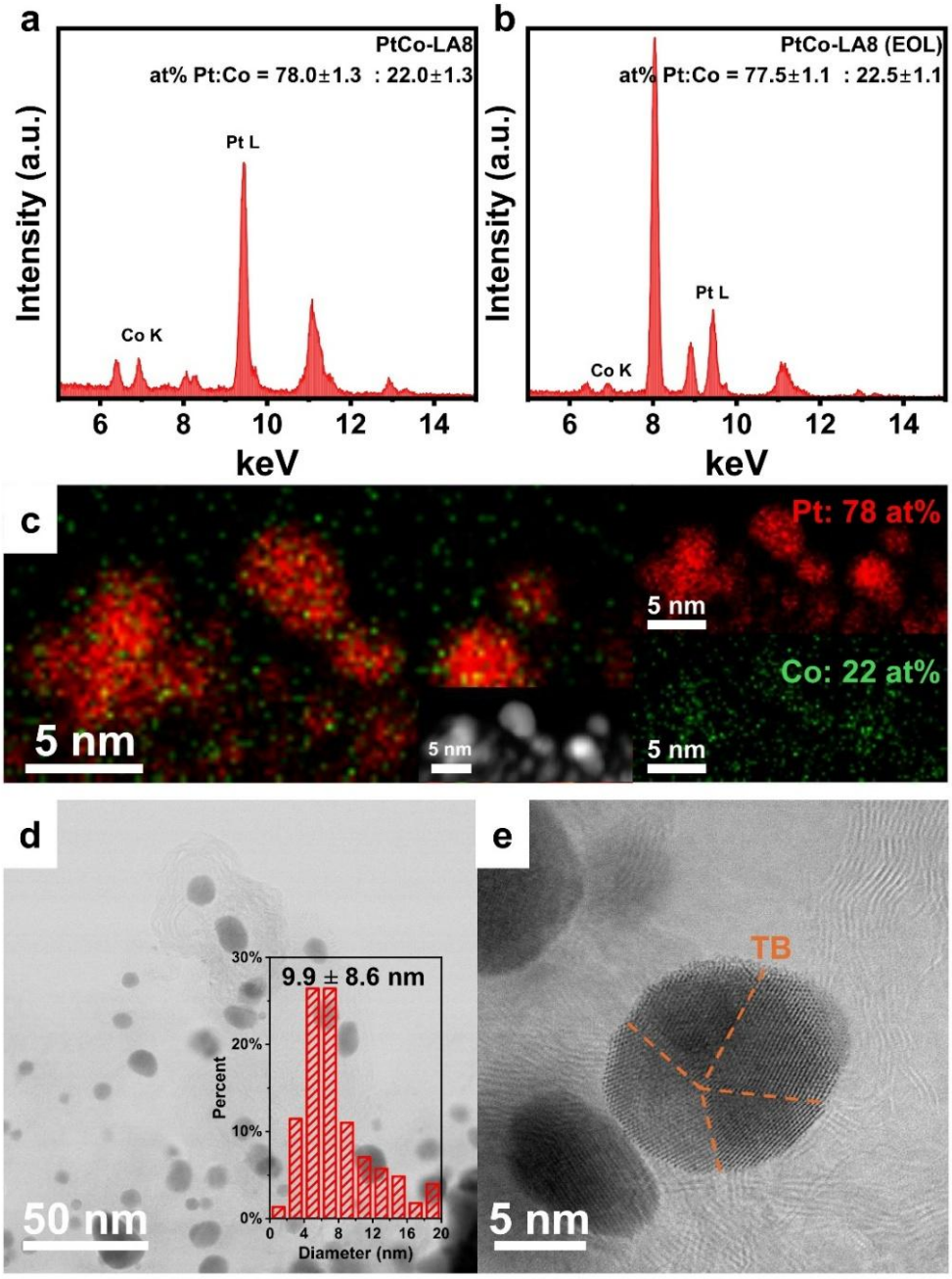

Figure 4. 5 EDS spectrum of (a) PtCo-LA8, (b,c) EDS spectrum and mapping results of PtCo-LA8 (EOL), (d) TEM image of PtCo-LA8 (EOL) and its corresponding size distribution chart, and (e) HRTEM image of PtCo-LA8 (EOL).

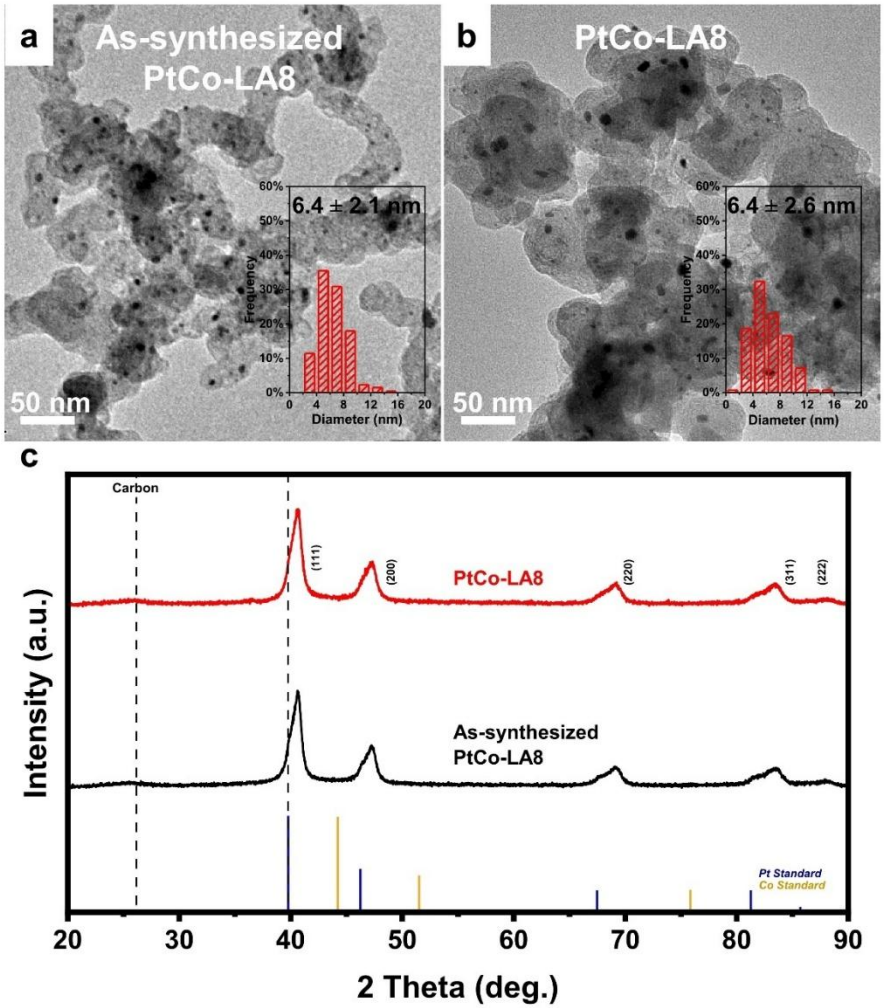

Figure 4. 6 TEM images and the size distribution charts of (a) as-synthesized PtCo-LA8 and (b) PtCo-LA8, and their corresponding (c) XRD patterns.

To further investigate the elemental valence states, we conducted the XPS analysis for PtCo-LA8 and commercial PtCo/C (Figure 4. 7). The Pt peaks at 71.4 eV, 72.8 eV, and 74.6 eV were assigned to Pt^0 $4f_{7/2}$, Pt^{2+} $4f_{7/2}$ and Pt^{4+} $4f_{7/2}$, respectively.[54] The Co 2p peaks were deconvoluted into 2 sets of peaks: 780.0 eV and 795.0 eV, 778.1 eV and 793.1 eV, corresponding to Co^{2+} and Co^0 peaks, respectively.[55] Quantitative analysis showed that PtCo-LA8 exhibited a comparable Pt^0 content (51.8%, Table 4. 5) with commercial PtCo (57.8%, Table 4. 5). The Co^0 content in PtCo-LA8 was 20.9% (Table 4. 5), lower than that of the commercial PtCo/C (33.3%,

Table 4. 5). This result is consistent with the reaction yield analysis, as Pt is more readily reduced than Co under the synthetic conditions.

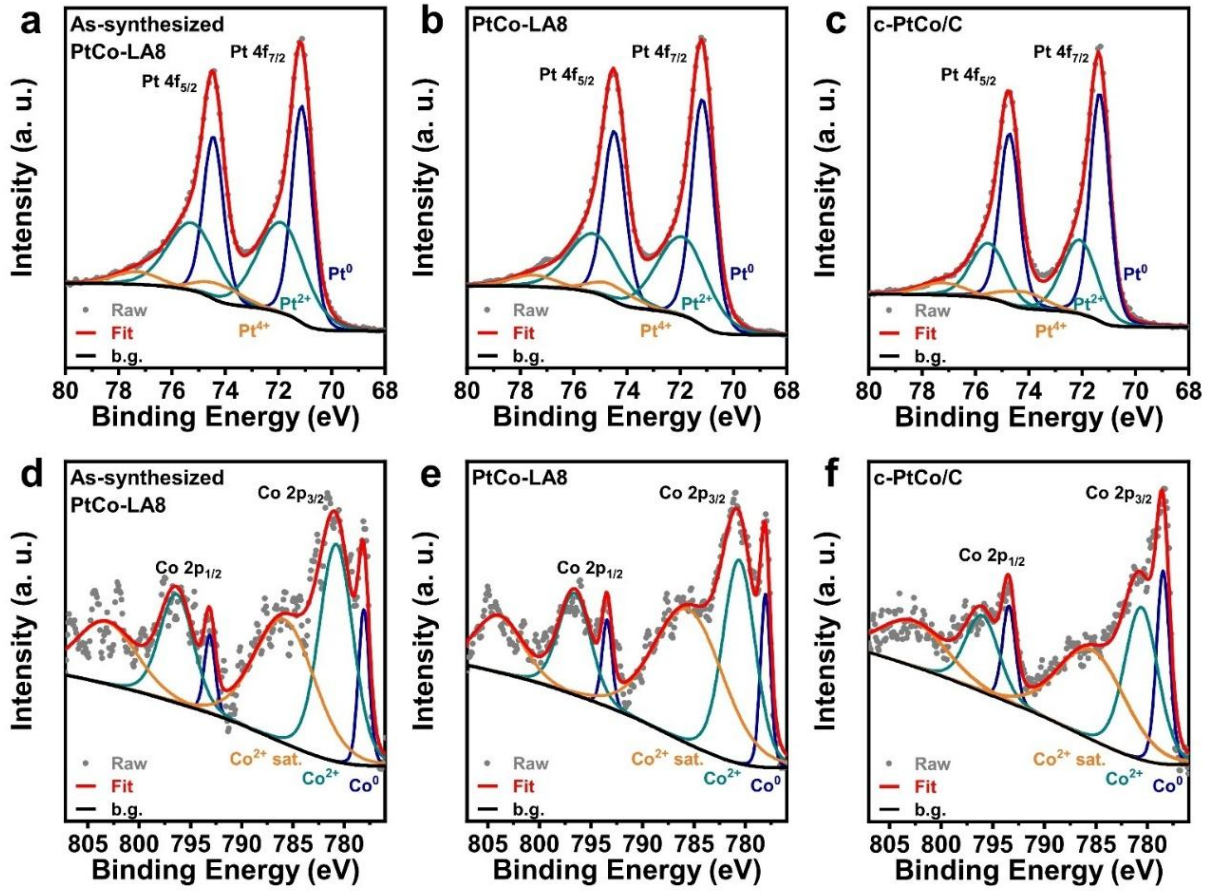

Figure 4. 7 XPS spectra of as-synthesized PtCo-LA8, PtCo-LA8, and 20% c-PtCo/C on (a-c) Pt 4f, and (d-f) Co 2p.

Sample	XPS High-resolution Scans				
	Relative Pt Ratio (%)			Relative Co Ratio (%)	
	Pt^0	Pt^{2+}	Pt^{4+}	Co^0	Co^{2+}
As-synthesized PtCo-LA8	46.5	45.6	7.9	18.7	81.3
PtCo-LA8	51.8	41.0	7.2	20.9	79.1
c-PtCo/C	57.8	32.8	9.3	33.3	66.7

Table 4. 5 Comparison of Pt and Co oxidation states obtained from XPS high-resolution scans for as-synthesized PtCo-LA8, PtCo-LA8, and 20% c-PtCo/C.

The unique twinning structure of PtCo-LA8 inspired us to explore its catalytic properties and potential practical applications. Since PtCo nanoparticles have been widely used as the ORR catalysts for high-performance PEMFCs, we incorporated PtCo-LA8 into an MEA and benchmarked its performance against commercial PtCo/C and Pt/C catalysts. Although PtCo-LA8 had a larger particle size (6.4 nm, Figure 4. 6b) than commercial PtCo/C (4.9 nm, Figure 4. 8a), it exhibited a MA of 0.56 A/mg_{Pt} at 0.9 V at the beginning-of-life (BOL), comparable to that of commercial PtCo/C (0.56 A/mg_{Pt}). Both catalysts outperformed the Department of Energy (DOE) target (0.44 A/mg_{PGM}) and commercial Pt/C (0.30 A/mg_{Pt}) (Figure 4. 9a,b).[56]

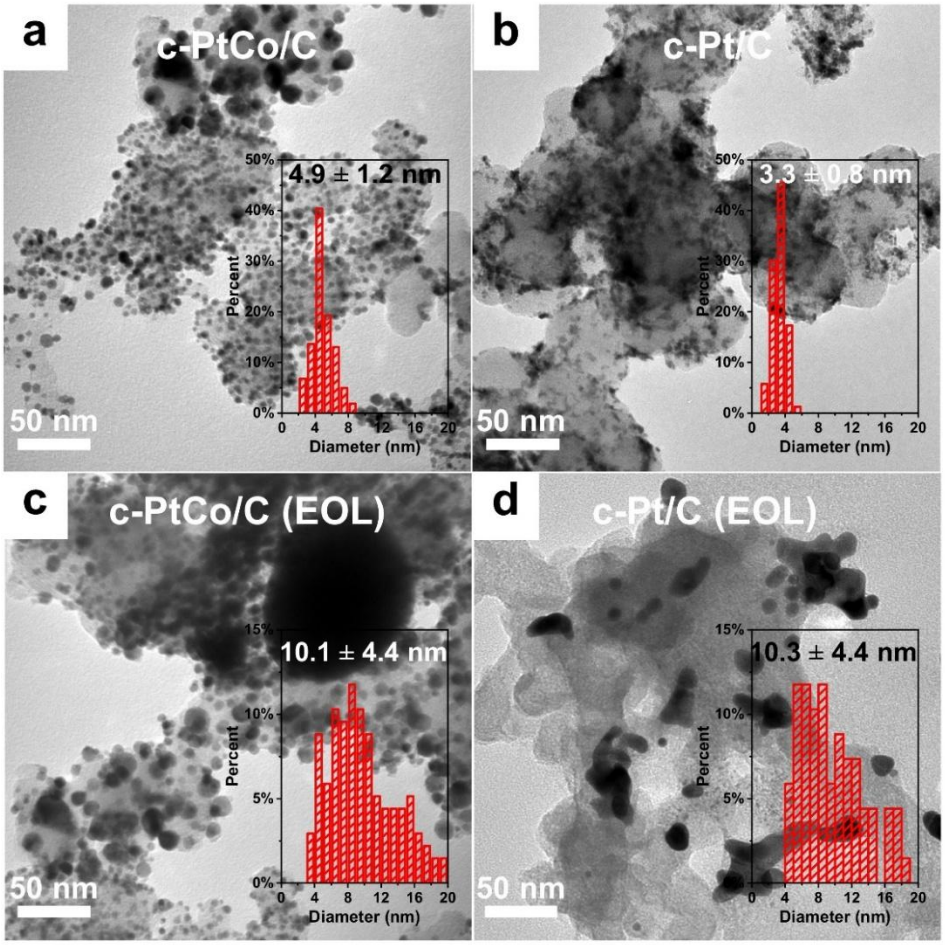

Figure 4. 8 TEM images and the size distribution charts of (a) 40% c-PtCo/C, (b) 40% c-Pt/C, and after 30k cycles AST (c) 40% c-PtCo/C (EOL), and (d) 40% c-Pt/C (EOL).

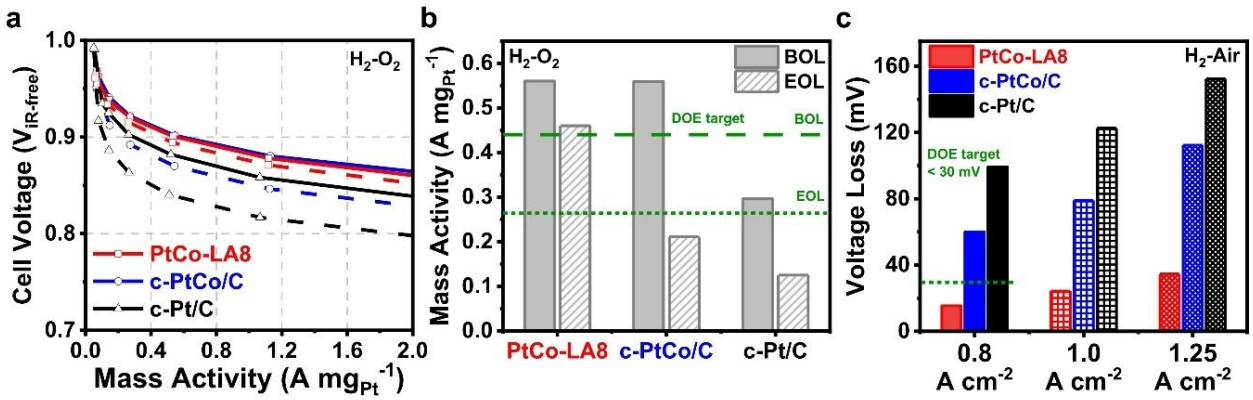

Figure 4. 9 Comparison of MEA performance of PtCo-LA8 with 40 wt% commercial PtCo/C (c-PtCo/C), and 40 wt% commercial Pt/C (c-Pt/C). (a) MA polarization curves at beginning-of-life (BOL, solid lines) and end-of-life (EOL, dashed lines) for PtCo-LA8, c-PtCo/C, and c-Pt/C tested under H_2-O_2 conditions. (b) Bar chart comparing MAs at 0.9 $V_{iR\text{-}free}$ for the three catalysts, benchmarked against the DOE 2025 targets: 0.44 A/mg_{PGM} at BOL and ≥60% retention (≥0.264 A/mg_{PGM}) at EOL. (c) Comparison of voltage loss after AST at current densities of 0.8, 1.0, and 1.25 A/cm^2 under H_2-air conditions. The DOE 2025 target for voltage loss at 0.8 A/cm^2 is <30 mV. PtCo-LA8 shows significantly improved activity retention and lower voltage degradation relative to commercial catalysts.

Despite their similar initial activity, PtCo-LA8 showed markedly superior stability. We followed the DOE-recommended protocol to evaluate the stability of the catalysts by applying square-wave potential cycling between 0.60 and 0.95 V for 30,000 cycles. Remarkably, PtCo-LA8 retained an outstanding end-of-life (EOL) MA of 0.46 A/mg_{Pt}, more than doubled that of commercial PtCo/C (0.21 A/mg_{Pt}) and Pt/C (0.13 A/mg_{Pt}) (Figure 4. 9a,b). Notably, even after AST, the EOL activity of PtCo-LA8 surpassed the DOE's BOL activity target. PtCo-LA8 retained 82.1% of its initial MA, significantly higher than the DOE's required 60% and much higher than commercial PtCo/C (38%) and Pt/C (42%). In addition to its high EOL MA and MA retention, PtCo-LA8 exhibited remarkably low voltage loss under H_2-air test conditions. At a current density of 0.8 A/cm^2, it showed a voltage loss of only 15.3 mV—half of the DOE-specified requirement of <30 mV (Figure 4. 9c). In contrast, commercial PtCo/C and Pt/C showed much higher voltage losses of 60.0 mV and 99.3 mV, respectively (Figure 4. 9c, Figure 4. 10 a-c). This voltage loss gap became even more pronounced at higher current densities (1 A/cm^2 and 1.25 A/cm^2), where commercial PtCo/C consistently exhibited 3 to 4 times the voltage loss compared to PtCo-LA8.

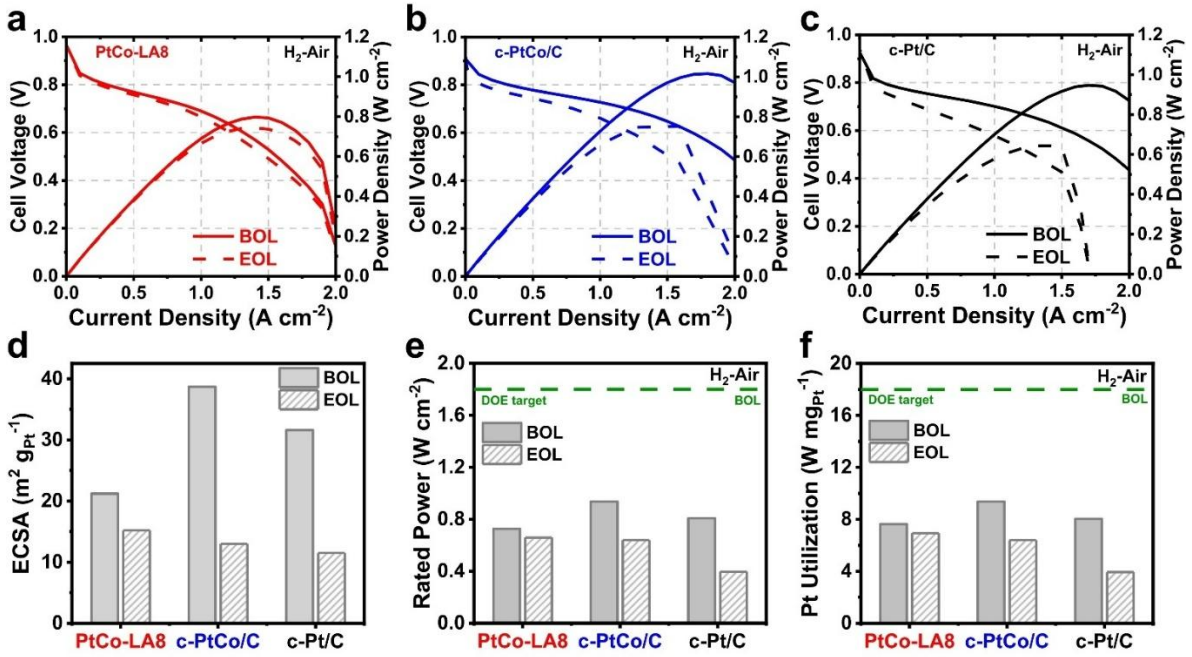

Figure 4. 10 MEA performance comparison of PtCo-LA8 with commercial samples. BOL (solid lines) and EOL (dotted lines) polarization curves of (a) PtCo-LA8, (b) 40% c-PtCo/C, and (c) 40% c-Pt/C under H_2-Air conditions. Comparisons of (d) electrochemical surface area (ECSA), (e) rated power, and (f) Pt utilization.

Compositional analysis of PtCo-LA8 at the EOL stage revealed stability in its alloy structure, with EDS showing a composition of $Pt_{78\pm1}Co_{22\pm1}$ (Figure 4. 5b). The average particle size of PtCo-LA8 increased moderately from 6.4 nm to 9.9 nm (55%, Figure 4. 5d), while commercial PtCo/C exhibited 106% increase in size (from 4.9 nm to 10.1 nm) and the size of Pt/C increased by 212% (from 3.3 nm to 10.3 nm) at the EOL stage (Figure 4. 8c,d), suggesting better stability of PtCo-LA8. Overall, these results demonstrate that PtCo-LA8, with its unique nanotwinned structure, delivers both high catalytic activity and exceptional durability, making it a promising candidate for next-generation PEMFC cathode catalysts.

To investigate the formation of nanotwinning, we performed laser ablation on commercial PtCo/C and Pt/C catalysts. Prior to laser ablation, commercial PtCo/C exhibited a nanotwinning fraction of only 12% (Figure 4. 11a), with an average twinned particle size of 4.3 ± 0.7 nm, similar to the overall average particle size (3.5 ± 0.9 nm) (Figure 4. 12a). Interestingly, after applying the

same synthetic laser ablation conditions used for PtCo-LA8 to commercial PtCo/C (c-PtCo/C-LA8), the overall nanotwinning percentage increased to 44%, and for nanoparticle diameter below 7.5 nm, the nanotwinning percentage reached 59%, approaching that of PtCo-LA8 (61%) (Figure 4. 11a). In comparison, laser ablation of commercial Pt/C (c-Pt/C-LA8) led primarily to particle growth from 2.6 nm to 6.2 nm (Figure 4. 12d), while the nanotwinning percentage only increased slightly from 10% to 15% (Figure 4. 11a). These observations suggest that agglomeration during laser ablation facilitates nanotwinning in PtCo alloys, both in bottom-up synthesized PtCo-LA8 and in laser ablation of commercial PtCo/C. However, agglomeration alone cannot fully account for the formation of nanotwins. Instead, our findings indicate that the incorporation of Co plays a key role in promoting nanotwinning in Pt-based alloys.

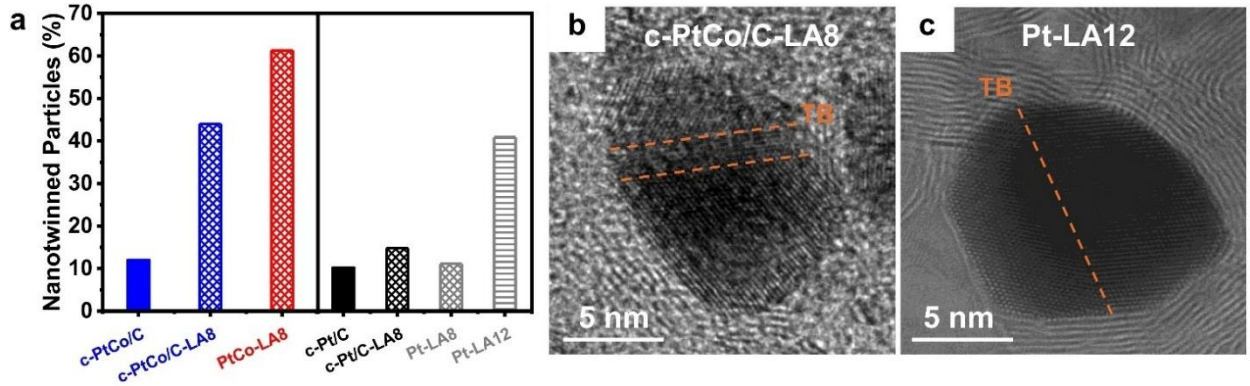

Figure 4. 11 Nanotwin formation in Pt-based electrocatalysts induced by laser ablation. (a) Quantitative comparison of the percentage of nanotwinned nanoparticles in commercial PtCo/C and Pt/C before and after laser treatment, highlighting the effect of laser ablation on twin formation in PtCo-LA8, Pt-LA8, and Pt-LA12. (b, c) Representative TEM images of (b) c-PtCo/C after laser ablation (c-PtCo-LA8) and (c) Pt-LA12, both showing well-defined twin boundaries.

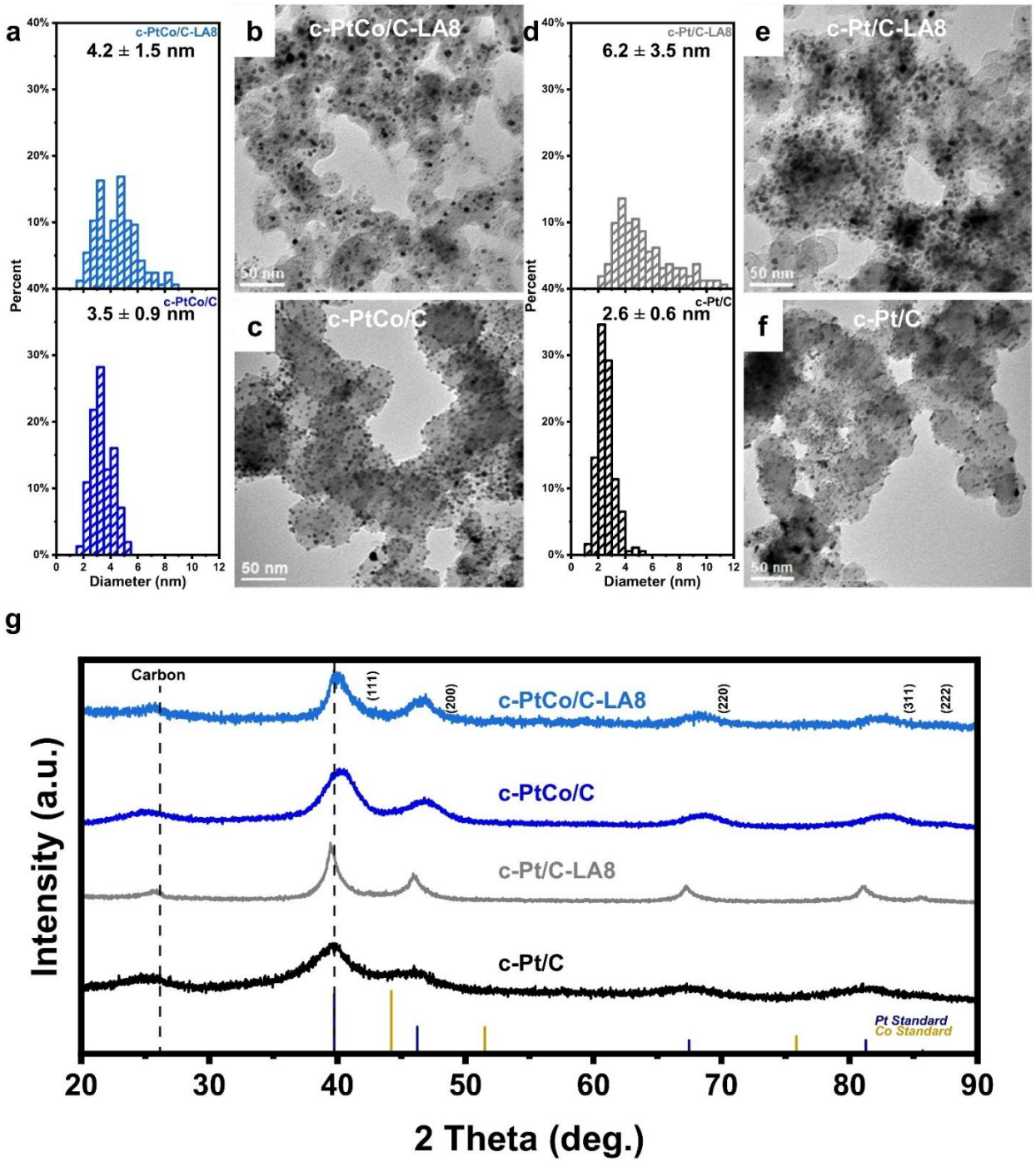

Figure 4. 12 TEM images and the size distribution charts of (a-c) 20% c-PtCo/C and (d-f) 20% c-Pt/C before and after laser ablation, along with their corresponding (g) XRD patterns.

To validate this hypothesis, we synthesized Pt nanoparticles via laser ablation under the same conditions as PtCo-LA8. The resulting nanotwin fraction in Pt-LA8 was only 11%, with an averaged particle diameter of 5.0 nm (Figure 4. 11a, Figure 4. 13a). We further increased the laser

power and exposure time, and although we observed much larger particles with an average diameter of 10.1 ± 4.9 nm in Pt-LA12 (Figure 4. 13b), the nanotwin percentage increased to 41%, which is still lower than the 61% observed in PtCo-LA8 (Figure 4. 11a). Based on these findings, we propose the following mechanism for twinning formation: 1) Under high-energy laser ablation and driven by the thermal effect, small PtCo particles migrate and attach to nearby neighbors. Rapid cooling then freezes intermediate metastable structures, leading to high yield nanotwin formation. Laser-ablation driven nanotwin formation can be achieved even in metals with high stacking fault energy such as Pt, though at a low percentage; 2) The addition of Co significantly reduces the stacking fault energy of Pt, enhancing atomic diffusion even under lower energy disturbances and at smaller particle sizes. The incorporation of multiple transition metals into Pt-based binary alloys has been confirmed by DFT calculations to reduce the intrinsic stacking fault energy and enhance the propensity for twinning formation.[57] Furthermore, both computational and experimental studies have demonstrated that the addition of Co effectively lowers the stacking fault energy in Ni-based and other alloys.[58-60] Together, these pathways either enhance the likelihood of particle coalescence or lower the energetic barrier for twin boundary formation, resulting in the high nanotwinning yields observed in PtCo-LA8.

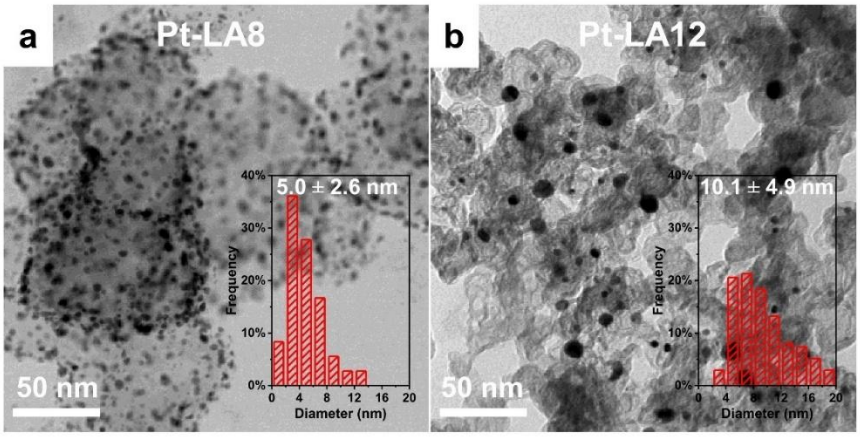

Figure 4. 13 TEM images and the size distribution charts of (a) Pt-LA8 and (b) Pt-LA12.

4.4 Conclusion

In summary, this work shows how laser ablation technique can be leveraged to create nanotwinned structures that are hard to obtain otherwise. In this case, nanotwinned PtCo nanoparticles were synthesized as catalysts for the ORR in PEMFCs. The nanotwinned PtCo nanoparticles exhibited excellent activity and significantly enhanced stability compared to commercial PtCo/C and Pt/C in the MEAs. The formation of nanotwinning can be attributed to either particle agglomeration or lowering of stacking fault energy. Notably, the laser ablation-based synthesis is exceptionally rapid and offers a powerful platform for both the high-throughput exploration of metastable material libraries and the scalable production of advanced catalysts with reduced processing time.

4.5 References

1. Li, X., Lu, L., Li, J., Zhang, X. & Gao, H. Mechanical properties and deformation mechanisms of gradient nanostructured metals and alloys. *Nat. Rev. Mater.* **5**, 706–723 (2020).
2. Sun, L. G., Wu, G., Wang, Q. & Lu, J. Nanostructural metallic materials: Structures and mechanical properties. *Mater. Today* **38**, 114–135 (2020).
3. Fernández-García, M., Martínez-Arias, A., Hanson, J. C. & Rodriguez, J. A. Nanostructured oxides in chemistry: Characterization and properties. *Chem. Rev.* **104**, 4063–4104 (2004).
4. Rosi, N. L. & Mirkin, C. A. Nanostructures in biodiagnostics. *Chem. Rev.* **105**, 1547–1562 (2005).
5. Zaera, F. Nanostructured materials for applications in heterogeneous catalysis. *Chem. Soc. Rev.* **42**, 2746–2762 (2013).

6. Choi, S. *et al.* Kink-Controlled Gold Nanoparticles for Electrochemical Glucose Oxidation. *Nano Lett.* **24**, 4528–4536 (2024).

7. Park, S. *et al.* Iridium-Cooperated, Symmetry-Broken Manganese Oxide Nanocatalyst for Water Oxidation. *J. Am. Chem. Soc.* **145**, 26632–26644 (2023).

8. Xia, Y. *et al.* One-dimensional nanostructures: Synthesis, characterization, and applications. *Adv. Mater.* **15**, 353–389 (2003).

9. Yao, Y. *et al.* High-entropy nanoparticles: Synthesis-structure-property relationships and data-driven discovery. *Science* **376**, (2022).

10. Wang, X. *et al.* Continuous Synthesis of Hollow High-Entropy Nanoparticles for Energy and Catalysis Applications. *Adv. Mater.* **32**, 2002853 (2020).

11. Therrien, F., Jones, E. B. & Stevanović, V. Metastable materials discovery in the age of large-scale computation. *Appl. Phys. Rev.* **8**, (2021).

12. Sun, W. *et al.* The thermodynamic scale of inorganic crystalline metastability. *Sci. Adv.* **2**, e1600225 (2016).

13. Uttam, P., Kumar, V., Kim, K. H. & Deep, A. Nanotwinning: Generation, properties, and application. *Mater. Des.* **192**, (2020).

14. Lu, K. Stabilizing nanostructures in metals using grain and twin boundary architectures. *Nat. Rev. Mater.* **1**, (2016).

15. Ko, M., Padgett, E., Yarlagadda, V., Kongkanand, A. & Muller, D. A. Revealing the Nanostructure of Mesoporous Fuel Cell Catalyst Supports for Durable, High-Power Performance. *J. Electrochem. Soc.* **168**, 024512 (2021).

16. Cheng, Z., Zhou, H., Lu, Q., Gao, H. & Lu, L. Extra strengthening and work hardening in gradient nanotwinned metals. *Science* **362**, (2018).

17. Huang, Q. *et al.* Nanotwinned diamond with unprecedented hardness and stability. *Nature* **510**, 250–253 (2014).

18. Zhang, X. & Misra, A. Superior thermal stability of coherent twin boundaries in nanotwinned metals. *Scr. Mater.* **66**, 860–865 (2012).

19. Cai, J. *et al.* Highly Selective Electrochemical Reduction of CO2 into Methane on Nanotwinned Cu. *J. Am. Chem. Soc.* **145**, 9136–9143 (2023).

20. Twinning Enhances Efficiencies of Metallic Catalysts toward Electrolytic Water Splitting.

21. Gu, J. *et al.* Twinning Engineering of Platinum/Iridium Nanonets as Turing-Type Catalysts for Efficient Water Splitting. *J. Am. Chem. Soc.* **146**, 5355–5365 (2024).

22. Sun, L., He, X. & Lu, J. Nanotwinned and hierarchical nanotwinned metals: A review of experimental, computational and theoretical efforts. *NPJ Comput. Mater.* **4**, (2018).

23. Jiang, G. *et al.* Recrystallization and twinning enhancing mechanical property of laser directed energy deposited CoCrFeNi high entropy alloys induced by synchronous ultrasonic impact. *Addit. Manuf.* **93**, (2024).

24. Lin, F., Zhang, Y., Godfrey, A. & Juul Jensen, D. Twinning during recrystallization and its correlation with the deformation microstructure. *Scr. Mater.* **219**, (2022).

25. Zhu, Y. T., Liao, X. Z. & Wu, X. L. Deformation twinning in nanocrystalline materials. *Prog. Mater. Sci.* **57**, 1–62 (2012).

26. Yu, Q. *et al.* The nanostructured origin of deformation twinning. *Nano Lett.* **12**, 887–892 (2012).

27. Song, M. *et al.* In situ atomic observations of aggregation growth and evolution of penta-twinned gold nanocrystals. *Nat. Commun.* **15**, (2024).

28. Chen, K.-C., Wu, W.-W., Liao, C.-N., Chen, L.-J. & Tu, K. N. Observation of Atomic Diffusion at Twin-Modified Grain Boundaries in Copper. *Science* **22**, 1066–1069 (2008).

29. Song, M. *et al.* Oriented attachment induces fivefold twins by forming and decomposing high-energy grain boundaries. *Science* **367**, 40–45 (2020).

30. Cao, S. *et al.* On the role of cooling rate and temperature in forming twinned α' martensite in Ti–6Al–4V. *J. Alloys Compd.* **813**, (2020).

31. Haase, C., Barrales-Mora, L. A., Molodov, D. A. & Gottstein, G. Tailoring the mechanical properties of a twinning-induced plasticity steel by retention of deformation twins during heat treatment. *Metall. Mater. Trans. A* **44**, 4445–4449 (2013).

32. Lee, S. *et al.* Reversible cyclic deformation mechanism of gold nanowires by twinning-detwinning transition evidenced from in situ TEM. *Nat. Commun.* **5**, (2014).

33. Choi, C. *et al.* A Highly Active Star Decahedron Cu Nanocatalyst for Hydrocarbon Production at Low Overpotentials. *Adv. Mater.* **31**, (2019).

34. Wang, Z. *et al.* High stress twinning in a compositionally complex steel of very high stacking fault energy. *Nat. Commun.* **13**, (2022).

35. Velasco, L. & Hodge, A. M. Growth twins in high stacking fault energy metals: Microstructure, texture and twinning. *Mater. Sci. Eng. A* **687**, 93–98 (2017).

36. Yu, K. Y. *et al.* Basic criteria for formation of growth twins in high stacking fault energy metals. *Appl. Phys. Lett.* **103**, (2013).

37. Huang, L. *et al.* Advanced Platinum-Based Oxygen Reduction Electrocatalysts for Fuel Cells. *Acc. Chem. Res.* **54**, 311–322 (2021).

38. Mistry, H., Varela, A. S., Kühl, S., Strasser, P. & Cuenya, B. R. Nanostructured electrocatalysts with tunable activity and selectivity. *Nat. Rev. Mater.* **1**, (2016).

39. Jiao, K. *et al.* Designing the next generation of proton-exchange membrane fuel cells. *Nature* **595**, 361–369 (2021).

40. Liu, R. T. *et al.* Recent advances in proton exchange membrane water electrolysis. *Chem. Soc. Rev.* **52**, 5652–5683 (2023).

41. Chen, F. Y., Wu, Z. Y., Adler, Z. & Wang, H. Stability challenges of electrocatalytic oxygen evolution reaction: From mechanistic understanding to reactor design. *Joule* **5**, 1704–1731 (2021).

42. Qiu, C., Xu, Z., Chen, F. Y. & Wang, H. Anode Engineering for Proton Exchange Membrane Water Electrolyzers. *ACS Catal.* **14**, 921–954 (2024).

43. Brown, B., Newkirk, J. & Liou, F. Absorption of Nitrogen during Pulsed Wave L-PBF of 17-4 PH Steel. *Materials* **14**, (2021).

44. Dev Singh, D., Mahender, T. & Raji Reddy, A. Powder bed fusion process: A brief review. *Mater. Today Proc.* **46**, 350–355 (2021).

45. Chowdhury, S. *et al.* Laser powder bed fusion: a state-of-the-art review of the technology, materials, properties & defects, and numerical modelling. *J. Mater. Res. Technol.* **20**, 2109–2172 (2022).

46. Narasimharaju, S. R. *et al.* A comprehensive review on laser powder bed fusion of steels: Processing, microstructure, defects and control methods, mechanical properties, current challenges and future trends. *J. Manuf. Process.* **75**, 375–414 (2022).

47. Narayana Samy, V. P., Schäfle, M., Brasche, F., Krupp, U. & Haase, C. Understanding the mechanism of columnar–to-equiaxed transition and grain refinement in additively manufactured steel during laser powder bed fusion. *Addit. Manuf.* **73**, (2023).

48. Karimi, P. *et al.* Columnar-to-equiaxed grain transition in powder bed fusion via mimicking casting solidification and promoting in situ recrystallization. *Addit. Manuf.* **46**, (2021).

49. Sabzi, H. E. *et al.* Deformation twinning-induced dynamic recrystallization during laser powder bed fusion. *Scr. Mater.* **207**, (2022).

50. Yavari, R. *et al.* Digitally twinned additive manufacturing: Detecting flaws in laser powder bed fusion by combining thermal simulations with in-situ meltpool sensor data. *Mater. Des.* **211**, (2021).

51. Chen, A. & Holt-Hindle, P. Platinum-based nanostructured materials: Synthesis, properties, and applications. *Chem. Rev.* **110**, 3767–3804 (2010).

52. Bass, R. J., Dunn, T. M., Lin, Y. C. & Hohn, K. L. Syngas production from catalytic partial oxidation of n-butane: Comparison between incipient wetness and sol-gel prepared Pt/Al2O3. *Ind. Eng. Chem. Res.* **47**, 7184–7189 (2008).

53. Holade, Y., Sahin, N. E., Servat, K., Napporn, T. W. & Kokoh, K. B. Recent advances in carbon supported metal nanoparticles preparation for oxygen reduction reaction in low temperature fuel cells. *Catalysts* **5**, 310–348 (2015).

54. Vovk, E. I., Kalinkin, A. V., Smirnov, M. Y., Klembovskii, I. O. & Bukhtiyarov, V. I. XPS Study of Stability and Reactivity of Oxidized Pt Nanoparticles Supported on TiO2. *J. Phys. Chem. C* **121**, 17297–17304 (2017).

55. Biesinger, M. C. *et al.* Resolving surface chemical states in XPS analysis of first row transition metals, oxides and hydroxides: Cr, Mn, Fe, Co and Ni. *Appl. Surf. Sci.* **257**, 2717–2730 (2011).

56. U.S. DRIVE Fuel Cell Technical Team. *Fuel Cell Technical Team Roadmap*. www.uscar.org. (2017).

57. Yang, S., Yu, X., Jiang, X., Wu, H. & Zhao, J. Effect of composition on mechanical properties of Pt-based binary and ternary alloys: A first-principles study. *Comput. Mater. Sci.* **240**, (2024).

58. J Gallagher, P. C. The Influence Effects on the of Alloying, Temperature, and Related Stacking Fault Energy. *Metallurgical Transactions* **1**, 2429–2461 (1970).

59. Xu, L., Casillas-Trujillo, L., Gao, Y. & Xu, H. Compositional effects on stacking fault energies in Ni-based alloys using first-principles and atomistic simulations. *Comput. Mater. Sci.* **197**, (2021).

60. Shih, M., Miao, J., Mills, M. & Ghazisaeidi, M. Stacking fault energy in concentrated alloys. *Nat. Commun.* **12**, (2021).

Chapter 5. Conclusion and Perspective

This dissertation focused on the development of advanced Pt-based electrocatalysts for PEMFCs in heavy-duty transportation applications. Despite significant advances in PEMFC technology, widespread deployment in heavy-duty vehicles remains limited by challenges in catalyst durability, platinum utilization, and scalable catalyst manufacturing.

In the first study, a graphene nanopocket-protected Pt catalyst was developed to address the stringent durability requirements of heavy-duty fuel cells. By suppressing Pt dissolution, particle coalescence, and ionomer poisoning, the catalyst achieved a projected fuel cell lifetime exceeding 200,000 h under heavy-duty operating conditions. In the second study, a CeO_x-stabilized Pt nanocatalyst was designed to overcome the conventional trade-off between Pt loading and durability. The strong CeO_x-Pt interaction mitigated Pt dissolution and particle growth, enabling highly durable fuel cell operation while reducing Pt usage by approximately 70% and satisfying DOE heavy-duty targets. In the third study, a laser ablation-based synthesis strategy enabled a ten-fold increase in catalyst production rate while introducing stable nanotwinned structures that enhanced catalyst durability.

Collectively, these studies demonstrate three complementary strategies for advancing PEMFC technology through improved durability, reduced Pt utilization, and scalable catalyst manufacturing. Looking forward, future efforts will aim to integrate these design principles to enable the scalable production of highly active and durable Pt-based catalysts. Future research will further explore catalyst design strategies for mitigating humidity inhomogeneity in large-area MEAs and operating under reduced-humidity, elevated-temperature conditions. Overall, the work presented in this dissertation advances the development of practical PEMFC technologies for heavy-duty transportation and contributes to the realization of a sustainable, zero-emission future.